博士論文

Electrochemical Nitrogen Reduction at Intermediate Temperature Using Solid Electrolyte

（中温における固体電解質を用いた窒素電解還元）

袁 瑶

Doctoral Dissertation

Electrochemical Nitrogen Reduction at Intermediate Temperature Using Solid Electrolyte

中温における固体電解質を用いた窒素電解還元

Yao YUAN

Department of Chemical System Engineering

School of Engineering

The University of Tokyo

Table of Contents

Chapter 1: Introduction

1.1 Haber-Bosch process

Nitrogen (N_2) constitutes 78% of the air, and N_2 fixation in nature is essential for life owing to the fact that the inorganic N-containing compounds are the sources of organic N-containing compounds biosynthesis. Though N_2 is chemical inactive due to the high bonding energy of the triple bonds (941 kJ mol^{-1}) and the N_2 molecular is non-polar. N_2 fixation is carried out naturally by bacteria to ammonia (NH_3) or by lightening to NO_x, which are soluble in soil. Fritz Haber was awarded the 1918 Nobel Prize in Chemistry for his *Synthesis of ammonia from its element*.[1] Later, Carl Bosch developed this high-pressure process on a large industrial scale and was awarded the 1931 Nobel Prize in Chemistry.[2] The reaction carried out under high temperature and pressure (500-600 °C, 200 atm at that time) by iron catalyst is given as:

$$N_2 + 3H_2 \rightarrow 2NH_3 \quad \Delta H° = -91.8\ \text{kJ/mol}$$

H_2 resource is from reactions between natural gas (CH_4) and steam by steam-methane reforming (SMR) and water-gas shift (WGS) which are given as:

$$CH_4 + H_2O \rightarrow CO + 3H_2 \quad \Delta H° = +206.1\ \text{kJ/mol}$$

$$CO + H_2O \rightarrow CO_2 + H_2 \quad \Delta H° = -41.2\ \text{kJ/mol}$$

NH_3 production contributes about 2% of the world's energy consumption annually, most of the consumption is from the strongly endothermic SMR at 800-1000 °C. other major energy consumption processes include CO_2 removal section, reactant gases purification section, reactant gases compression for NH_3 synthesis section and NH_3 separation section.[3]

The industrial iron catalyst composed mainly by magnetite (Fe_3O_4). Oxides such as K_2O, Al_2O_3, and CaO are added as promotors. Fe_3O_4 then reduced in syngas feed and finally

form α-Fe phase, which is commonly called “ammonia iron”. The promoted Ru-based catalysts are reported as the second generation NH_3 catalysts, which are carried out at 300-400 °C and ambient pressure and achieve much higher activities than Fe-based catalysts under same conditions. While when the operation conditions are same with Fe-based catalysts used in conventional high-pressure industrial processes, the overall cost would be higher than system with Ru-based catalysts. This is the reason why industrial system with Ru-based catalysts constitute less than 5% of NH_3 production.[4]

The Harbor process was purchased by the German chemical company BASF, and the first Haber process plant, Oppau plant in Germany, initially achieved 9000 tons of NH_3 output annually. During the First World War, the Allies were using large deposits of sodium nitrate in Chile, controlled by a British company, for munitions apply. While Germany had no such nitrates, the Oppau plant was delivered to the explosive industry.[5] While the main motivation of Harbor process was food corps development in order to overcoming the population explosion problem initially, the invention actually caused disaster and millions of people died in armed conflicts in the past 100 years. For environmental issues, total atmosphere emissions of NH_3 and NO_x from the Harbor-Bosch process increased and thus affecting the N-cycle naturally.[6] The increase of more reactive forms of N disrupted the balance of greenhouse gases, and affect the ozone depletion. Since the major source of H_2 in the Harbor-Bosch process is form the reactions of CH_4 and steam by SMR and WGS, about 400 Mt of CO_2 is released annually, which contributes nearly 1% of global green-house gas emissions. Nevertheless, the Harbor-Bosch process fed billions of people and over 80% of produced NH_3 is used for fertilizer production nowadays.

1.2 Catalysts for ammonia synthesis

1.2.1 Metal

An early theoretical calculation study of electrochemical NRR on transition-metals surfaces was introduced by Skúlason *et al.*[7] in 2012. The theoretical limiting potentials for NRR via a Heyrovsky-type mechanism against the chemisorption energies of N adatom (N*) on various transition metal surfaces with an acidic electrolyte (pH = 0) were plotted into a volcano diagram, where the free energies were calculated by density functional theory (DFT) with a standard hydrogen electrode (SHE). In the Heyrovsky-type mechanism, the adsorbed N_2H_x or NH_x species react directly with protons and electrons, in contrast, protons reduced into H adatom (H*) firstly and then react with N_2H_x or NH_x species is called Tafel-type mechanism. According to the volcano diagram, transition metals on the such as Sc, Y, Ti and Zr are expected to have a strong N-bond, and Rh, Ru, Ir, Co, Ni and Pt are likely to be covered with H* in priority, which mainly lead to HER instead of NRR. Transition metals which have strong N-bond are desired for NRR, while they are also easily form oxides and become inactive. Based on the above factors, Fe and Mo are expected to be the most active transition metals for NRR. According to the volcano plot of onset potentials of associative and dissociative reactions on various transition metal nano-clusters surface with the reaction free energy of N*,[8] Fe and Mo are expected to be the most promising candidates for electrochemical NRR via associative mechanism. Fe and Mo are the active sites in the enzyme nitrogenase where NRR occurs via associative enzymatic mechanism naturally.

According to the study by J.-L. Shi *et al.*,[9] the reaction barriers of concerted protons and

electrons transfer process in NRR with Fe, Mo, Rh and Ru have been computed using Fermi's golden rule. The rate constants for each intermediate steps are calculated based on the Marcus theory. As the results, the rate determining step (RDS) on Fe(110) and Mo(110) is *NH→*NH_2, and for Rh(111) and Ru(0001) surface, the RDS is *N_2→*NNH. The reaction rate constants for RDS are in the order of Fe(110) > Mo(110) > Ru(0001) > Rh(111).

1.2.2 Metal-free catalyst

Compared with metal catalysts, metal-free catalysts benefit from low cost. Reported metal-free catalysts mainly include carbon-based catalysts, phosphorous-based catalysts and nonmetallic compounds.[10] Porous carbon-based materials have high surface area, high electronic conductivity and abundant defects, these advantages are in favor of electrochemical NRR.[11] The performance of carbon-based materials can be modified with doped heteroatoms such as N, O and P. Yang *et al.*[12] studied both DFT and experimental observations of O, S, Se, Te doped carbon materials. For the first step of N_2 adsorption, it is greatly enhanced on S, Se, Te doped carbon materials, which implies charge accumulation on carbon atom plays a significant role. For the following protonation step to form *NNH, it is greatly enhanced on Se, Te doped carbon materials, which implies the contribution of spin polarization is obvious. The theoretical calculation corresponded to the experimental results that NRR was significantly promoted with Se, Te doped carbon materials. Te-doped carbon achieved an NH_3 yield rate of 1.91 μg /(h cm^2) (3.12×10^{-11} mol /(s cm^2) equivalent) and a FE of 4.67%. N-doped porous carbon derived from a zeolite imidazolate framework pyrolysis achieved an NH_3 yield rate of

0.84 μmol /(h cm^2) (2.33 × 10^{-10} mol /(s cm^2) equivalent) and a maximum FE of 1.42% at ambient condition.[13] NH_3 yield rate of 31.37 μg/(h mg-cat) and FE of 5.07% was achieved by a few-layer black phosphorous at ambient condition.[14] It was found that N_2 can be fixed via MvK mechanism in C_3N_4 by $^{15}N_2$ isotope labeling experiment[15]. A 2-D C_3N_4 with plentiful nitrogen vacancy was used for electrochemical NRR, an NH_3 yield rate of 17.85 μg /(h mg-cat) and a FE of 10.96% were obtained.[16] There is an abundance of metal-free materials such as carbon, and those metal-free materials have lower potential risk such as environmental pollution compared with metal. These advantages enable metal free materials to be a candidate of promising catalysts for large-scale NH_3 production.

1.2.3 Nitride

Recent theoretical calculation with DFT suggests that transition metal nitrides (TMNs) are promising electrochemical NRR catalysts at ambient conditions. The results from Abghoui *et al.*[17] support that electrochemical NRR with TMNs is favorable via Mars-van Krevelen (MvK) mechanism than with conventional associative mechanism. VN, NbN, CrN and ZrN were studied as promising nitrides candidates, and the overpotentials of the reduction from N_2 to NH_3 via MvK mechanism are smaller than mixed associative-dissociative mechanism.

1.2.4 Perovskite

Metal oxides are regarded as promising electrocatalysts for NRR because the catalytic

performance in the electrochemistry NRR is largely related to oxygen vacancies[18]. Metal oxides such as ceramics have lower cost than noble metals, as well as high chemical stability[19]. Perovskite compounds, generally expressed as ABO_3 (where A and B are typical cations), have variety interesting electronic properties and are widely used in electrochemical studies [20]. Recently, several La-based and transition metal doped perovskites with electronic conductivity were used as electrode catalysts for NRR. $La_2Ti_2O_7$ nanosheet loaded on carbon paper achieved an NH_3 yield rate of 25.15 μg/(h mg-cat) (4.11×10^{-11} mol/(s cm^2) equivalent) and a Faradic efficiency of 4.55% at ambient condition[21]. $LaFeO_3$ nanofiber loaded on carbon paper achieved an NH_3 yield rate of 25.15 μg/(h mg-cat) (3.04×10^{-11} mol/(s cm^2) equivalent) and a Faradic efficiency of 8.77% at ambient condition[22]. $La_{0.5}Sr_{0.5}FeO_{3-\delta}$ loaded on carbon paper achieved an NH_3 yield rate of 11.51 μg/(h mg-cat) and a Faradic efficiency of 0.54%, and oxygen vacancy could assist the overall reaction according to the DFT calculation[23]. While not only NH_3 yield rate but also Faradic efficiency with perovskite catalysts is still much lower than with metal catalysts, perovskites are tolerable to acidic or basic electrolytes and have lower cost thus might be suitable for large-scale industrial production.

1.2.5 Complex

Number of transition metal centered complexes such as $(\pi\text{-}C_5H_5)_2TiCl_2$[24], (3,5-(2,4,6-i-$Pr_3C_6H_2)_2C_6H_3$)Mo(Cl) [25], *trans*-[Fe(1,2-bis(bis(methoxypropyl)phosphino)ethane)$_2$H(N_2)]$^+$ [26] were reported for catalytic N_2 fixation in the last years. Several complexes $(\pi\text{-}C_5H_5)_2TiCl_2$[27], Ni3s8[28] such as were tried for electrochemical N_2 reduction. Complex catalysts exhibit high selectivity to form NH_3

and/or N_2H_4. The non-aqueous operation environment can suppress the proton activity.

1.2.6 Biological catalyst

Biologically dinitrogen reduction by nitrogenases provides a dominant route for nitrogen fixation into amino acids and nucleotides. One of the most effective components in the enzyme nitrogenase is the FeMo-cofactor protein. The FeMo-cofactor contains an 4Fe:3S cluster and a Mo:3Fe:3S cluster.[29] the center of the triangular prism formed by six Fe provides favorable interaction sites for dinitrogen and reduced dinitrogen. While the distances between Fe in the cofactor are longer than those in metallic Fe, the spacing of the Fe atoms in the cofactor are like that of the metallic Fe surfaces used as industrial Haber-Bosch catalysts.[30] The overall dinitrogen reduction can be given as[31]:

$$N_2 + 8H^+ + 8e^- + 16\text{MgATP} \rightarrow 2NH_3 + H_2 + 16\text{MgADP} + 16\text{Pi}$$

In theory, the enzyme can be able to be controlled electrochemically as a bioelctrocatalyst. In the work by Ross D. Milton *et al.*,[32] a bioelectrochemical system with hydrogenase used as anode, nitrogenase used as cathode, and methyl viologen used as an electron mediator for both anode and cathode achieved an NH_3 yield rate of 2.1±0.5 μmol/mg-cat and a Faradic efficiency of 58.8±6.1 %. Since nitrogenase is an ATP-dependent enzyme, an ATP regeneration system was applied. In the work by D. P. Hickey *et al.*,[33] a direct bioelectrochemical synthesis of NH_3 was carried out without ATP and electron mediator. An NH_3 yield rate of 1.1±0.2 μmol/mg-cat was achieved. The bioelectrosynthesis can achieve high Faradic efficiency, however, the biocatalysts exhibit low stability. In the case of an ATP-dependent enzyme used as bioelectrode, an expensive ATP regeneration system is required.[34]

1.3 Electrocatalytic nitrogen reduction

Various electrolytic cells with solid and liquid electrolytes have been reported for electrochemical nitrogen reduction over a wide temperature range. While those electrolytic cells can be classified according to various criteria, they are divided into three categories in the following discussion: low temperature (T < 100 °C), medium temperature (100 °C < T < 500 °C) and high temperature (T > 500 °C). Equilibrium potentials of HER and NRR reactions are shown in Table 1.

Table 1 Equilibrium potentials of HER and NRR reactions.[35]

Reaction	E°(V)
$2H^+(aq) + 2e^- \rightleftharpoons H_2(g)$	0 (versus SHE)
$2H_2O(l) + 2e^- \rightleftharpoons H_2(g) + 2OH^-(aq)$	-0.828 (versus SHE, pH 14)
$N_2(g) + 6H^+(aq) + 6e^- \rightleftharpoons 2NH_3(g)$	+0.55 (versus NHE)
$N_2(g) + 8H^+(aq) + e^- \rightleftharpoons 2NH_4^+(aq)$	+0.274 (versus SHE)
$N_2(g) + 2H_2O(l) + 6H^+(aq) + 6e^- \rightleftharpoons 2NH_3 \cdot H_2O(aq)$	+0.092 (versus SHE)
$N_2(g) + 6H_2O(l) + 6e^- \rightleftharpoons 2NH_3(g) + 6OH^-(aq)$	-0.736 (versus SHE, pH 14)
$N_2(g) + H^+(aq) + e^- \rightleftharpoons N_2H(g)$	-3.2 (versus RHE)
$N_2(g) + 4H^+(aq) + 4e^- \rightleftharpoons N_2H_4(g)$	-0.36 (versus RHE)

SHE: standard hydrogen electrode (E = 0.000 V, activity of H^+ = 1mol/L)

NHE: normal hydrogen electrode (E ≈ 0.000 V, concentration of H^+ = 1mol/L)

RHE: reversible hydrogen electrode (E = 0.000 V – 0.0591×pH)

1.3.1 At low temperature (T < 100 °C)

Electrochemical NRR below 100 °C takes advantages of direct usage of solvent as proton source, and can be applied to water electrolysis system. There are generally four types of reactors which are illustrated in Fig. 1 in recent experimental investigations, which are divided by the differences on the cell configuration.

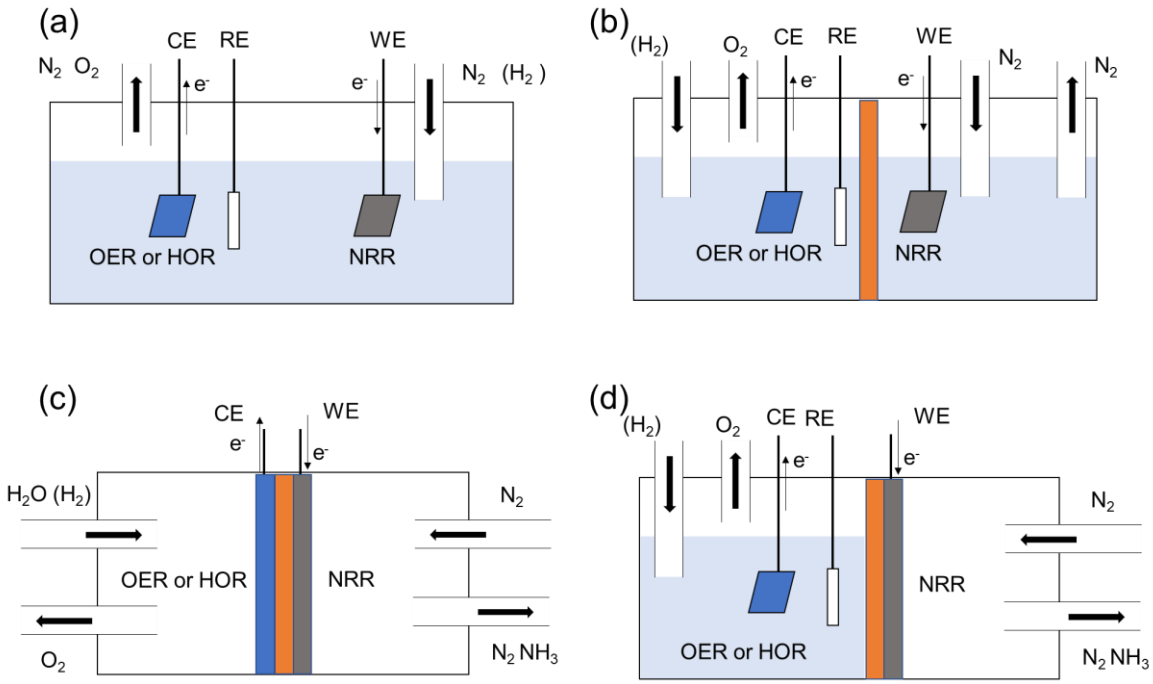

Figure 1 Schematics of four types of electrochemical cells for NRR at low temperature (<100 °C). RE: reference electrode. CE: counter electrode. WE: working electrode. OER: oxygen evolution reaction. HOR: hydrogen oxidation reaction. (a) Single chamber cell with liquid electrolyte. (b) H-type cell with liquid electrolyte. (c) Back-to-back cell. (d) Polymer electrolyte membrane (PEM)-type cell.

Generally, there are two main limitations of the liquid electrolyte-based electrochemical NRR cell. One is the extremely low solubility of N_2 in aqueous media, the other is HER

is dominant at almost the same potential of NRR. For the single-chamber cell, another limitation comes from the oxidation on the anode side of products formed on the cathode side. A membrane used to separate the anode and cathode area can suppress the decomposition of produced NH_3 effectively. One of the most popular choice is Nafion membrane. Nafion was discovered in 1960s by Dupont. The proton conductivity comes from the sulfonic acid ($-SO_3H$) group. Because of the acidity, produced basic NH_3 can dissolve into the membrane to form NH_4^+, and leads to decrease of proton conductivity. A significant contribution was achieved by Lan *et al.*[36] The Nafion membrane was exchanged in Li_2SO_4 solution and then a DC voltage was applied overnight to convert the proton conducting membrane to $Li^+/H^+/NH_4^+$ conducting membrane. While due to the proton block effect of added Li^+ ions, the proton conductivity decreased, NH_3 was successfully produced with a formation rate of 9.37×10^{-6} mol m^{-2} s^{-1} (equivalent of 9.37×10^{-10} mol cm^{-2} s^{-1}) and FE of 0.83% from water and air at 80 °C.

1.3.2 At intermediate temperature (100 °C < T < 500 °C)

There are generally three types of electrolytes applied to electrochemical NRR at intermediate temperature range, molten alkali chlorides, molten alkali hydroxides and solid-state acids. Electrochemical reaction on the cathode side with molten alkali chlorides electrolyte such as KCl-LiCl and Li_3N added KCl-LiCl is given as[37]:

$$1/2N_2 + 3e^- \rightarrow N^{3-}$$

Nitride ions are continuously supplied by the reduction of N_2, and the competing reaction is N_2 evolution on the anode side which is given as:

$$N^{3-} \rightarrow 1/2N_2 + 3e^-$$

Expect for the above reaction, another reason for NH_3 losses is the chemically dissolution of NH_3 presence as NH_2^- in the molten electrolyte.[38] This kind of novel method achieved high FE (up to 72%) among electrochemical NRR processes. Dissolution of H_2 into the molten electrolyte instead of the N_2 dissociation is the rate-determining step can contribute to such high FE. Mixture of NaOH and KOH is typically used as electrolyte because of the low molten point. OH^- becomes conductors instead of H^+ mentioned above, water and N_2 supply are on the same side of the cell where the reactant N_2 gas is diluted. Licht *et al.* achieved a FE of 35% in a molten NaOH-KOH suspension of nano-Fe_2O_3 at 200 °C from air and water.[39] Phosphate such as CsH_2PO_4 and $CsH_5(PO_4)_2$ is typically used as electrolyte at intermediate temperature. These inorganic acids have high proton conductivity and stability. CsH_2PO_4 mixed with SiP_2O_7 as a matrix achieves a proton conductivity value of 10^{-2} S/cm at 220 °C. However, CsH_2PO_4 will decompose without added steam. Added H_2O can occupy the N active sites or even oxidize the NRR catalyst. Like Nafion membrane mentioned above, produced NH_3 can dissolve into the acidic electrolyte and leads to a degradation.

Because N_2 is activated by the catalyst, the type of cathode catalyst used determines the efficiency of the direct electrochemical synthesis of NH_3. Ni mesh,[40 41] Pt/C, and Ru/C[42] have been reported as cathode catalysts for use at a temperature of approximately 200 °C. Bicer and Dincer reported the use of a Ni mesh cathode and nano-Fe_2O_3 particles suspended in a molten NaOH-KOH mixture as the electrolyte for an electrolytic cell, which produced NH_3 from N_2 and H_2 at 200 °C at a maximum formation rate of 4.41×10^{-9} mol/(s·cm^2) with a Faradaic efficiency of 14.17%. Using a Ru/C cathode and CsH_2PO_4/SiP_2O_7 electrolyte for the synthesis of NH_3 from N_2 and H_2O at 220 °C through solid–state electrolysis, a maximum reaction rate of 1.9×10^{-11} mol/(s·cm^2) and a Faradaic

efficiency of 0.06% was achieved.

1.3.3 At high temperature (T > 500 °C)

Proton conducting perovskite-type oxides such as Y-doped $SrZrO_3$ (SZY),[43] Y-doped $SrCeO_3$ (SCY)[44] and Y-doped $BaCeO_3$ (BCY)[45] used as an electrolyte for electrolytic NH_3 synthesis operated at about 500 ˚C and under ambient pressure have been reported. Reaction rate of 2.36×10^{-9} mol/(cm^2 s)[46] and Faradaic efficiency of 60% were achieved with BCY electrolyte and Ag-Pd cathode catalysts by N_2 and H_2. Ag, Pt, $La_{0.6}Sr_{0.4}Co_{0.2}Fe_{0.8}O_{3-\delta}$ (LSCF) as cathode material with a Y-doped $BaZrO_3$ (BZY) electrolyte from steam and N_2.[47]

1.4 Selectivity challenge

Lots of electrochemical NRR works as well as the DFT studies demonstrated that the hydrogen evolution reaction (HER) is a major competing reaction for NRR. In order to achieve higher selectivity against HER, there are generally three kinds of approaches.

1.4.1 Optimizing the structure of the catalysts and improve their inherent catalytic behavior.

Single atom catalysts (SACs) displayed high performance in electrochemical NRR because of the highly dispersed active sites. Such catalysts have high metal usage efficiency and can reduce the cost especially for noble metals such as Pt, Au and Pd.[48] A graphitic carbon nitride (C_3N_4) is now wildly used as substrate for metal atoms dispersion.[49] Increasing the porosity of the catalysts can not only improve the dispersion of active sites but also obtain a longer reactant gas residence time.

1.4.2 Suppressing proton activity and conductivity.

Since the rate-determining step of NRR is mostly supposed to be the cleavage of NN triple bond, and it seems unlikely to be proton-concentration limited. Excess proton covers the surface of catalysts and would occupy the spaces corresponding to N adsorption active sites. Numbers of aprotic electrolytes such as ionic liquid[50] and organic liquid[51] were used in order to control the proton concentration and achieved high Faradic efficiencies.

1.4.3 Developing the performance of electrolysis system and extending the life of used materials.

Catalysts-electrolyte interface engineering has been suggested as a powerful strategy for improvement of the electrolysis system. A H_2 permeable Ag-Pb alloy membrane was used between the Ru-based cathode catalyst and the acidic phosphate electrolyte[52] which would protect the catalyst from the electrolyte and thus extend the life of the system.

1.5 Mechanism of nitrogen reduction

In general, the mechanisms of nitrogen reduction reaction (NRR) can be classified as dissociative mechanism and associative mechanism illustrated in Fig. 2. Depending on the different hydrogenation processes, the associative mechanisms can be further classified as distal pathway, alternating pathway and enzymatic pathway. In the dissociative mechanism, the triple bond of the N_2 molecule is completely broken before bonding with the H atom. In contrast, in the associative mechanism, the triple bond of the N_2 molecule is cleaved and simultaneously bonded to the H atom.

The DFT calculations compared reactions on various metals theoretically, and are plotted in the free energy change in the rate limiting reaction against the N atom adsorption energy. In the case of the early transition metals such as Sc to Fe, the protonation reaction to form $*N_2H$ is the rate determining step, while in the later transition metals such as Pt and Pd, N_2 dissociation is the rate determining step.[7] For less reactive transition metals with weak nitrogen binding, the protonation of $*N_2$ to form $*N_2H$ is the potential determining step, while for reactive transition metals with strong nitrogen binding, the protonation of *NH to form $*NH_2$ or the desorption of $*NH_2$ is the potential determining step. Inspired by the intermediates of $*N_2H$, *NH and $*NH_2$, the improvement of N_2 electroreduction can be achieved generally by stabilization of $*N_2H$ and destabilization of *NH and $*NH_2$. However, $*N_2H$, *NH and $*NH_2$ only interact with metallic catalysts surface with a single N atom, therefore it is difficult to distinguish the binding of these adsorbates and catalysts.[53]

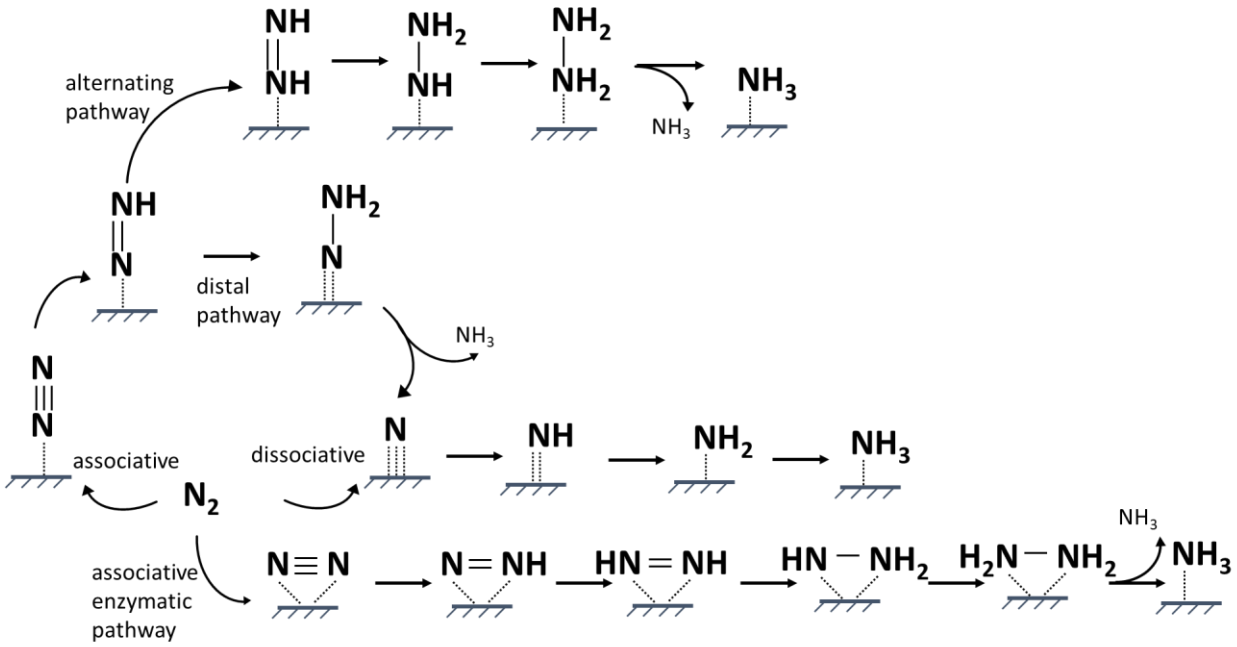

Figure 2 Mechanisms of nitrogen reduction reaction (NRR). The associative and dissociative pathways are illustrated.

1.5.1 Mars-van Krevelen (MvK) mechanism

In the Mars-van Krevelen (MvK) mechanism, the adsorbed NH_x or N_2H_x protonated to from NH_3, then the desorption of produced NH_3 creates an empty site and the next N_2 adsorbed on this regenerated site rather than on the present sites. MvK mechanism was first developed to explain the kinetics of SO_2 oxidation,[54] and is generally used for reactions such as selective oxidation of hydrocarbons, hydrodesulfurization and NOx removal nowadays.[55] Some recent theoretical studies of NRR on the surface of transition metal nitrides (TMNs) suggest NRR with TMNs via MvK pathway is more favorable than associative or dissociative mechanism at ambient conditions.

1.6 Ammonia detection and hydrazine detection

1.6.1 Nessler's reaction

Nessler's reagent gives a colored complex when determine a small amount of NH_3 in the water. However, because of strong basicity of the mercury solution, various metal cations and hydrazine (N_2H_4) cause serious interference in Nessler's method. Since the reagent of the Nessler's method contains mercury that is treated as a hazard waste.

$$2K_2HgI_4 + NH_3 + 3KOH \rightarrow HgO \cdot Hg(NH_2)I \downarrow + 7KI + 2H_2O$$

1.6.2 Indophenol reaction (Berthelot reaction)[56]

The indophenol reaction is the reaction of NH_4^+ and phenol to form indophenol dye under oxidation conditions. With the formation of indophenol dye, solution colors change from light yellow to blue, where indophenol dye has a strongly absorption between 630 and 720 nm which is specific for NH_3 quantification. The sensitivity of the detection limit is usually in the order of mg-NH_4^+/L, which is sensitive than the Nessler's method, and no interference from N_2H_4 at 2 mg-N_2H_4/L was observed.[57]

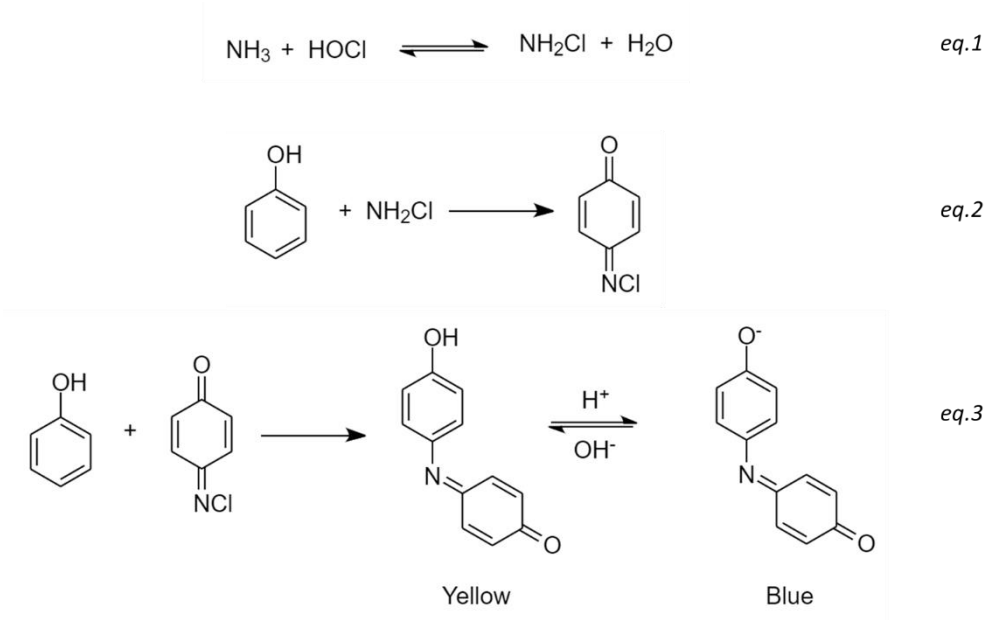

A modified indophenol reaction with sodium salicylate used as phenol is commonly called salicylate method investigated by Krom.[58] The maximum absorption wavelength of the formed blue dye is between 650-660 nm. During the reactions, an intermediate 5-aminosalisylate forms and accelerates the production of indophenol dye which was supported by the fact that solution contained only NH_3, sodium salicylate and chlorinating agent exhibited a slow dye formation.

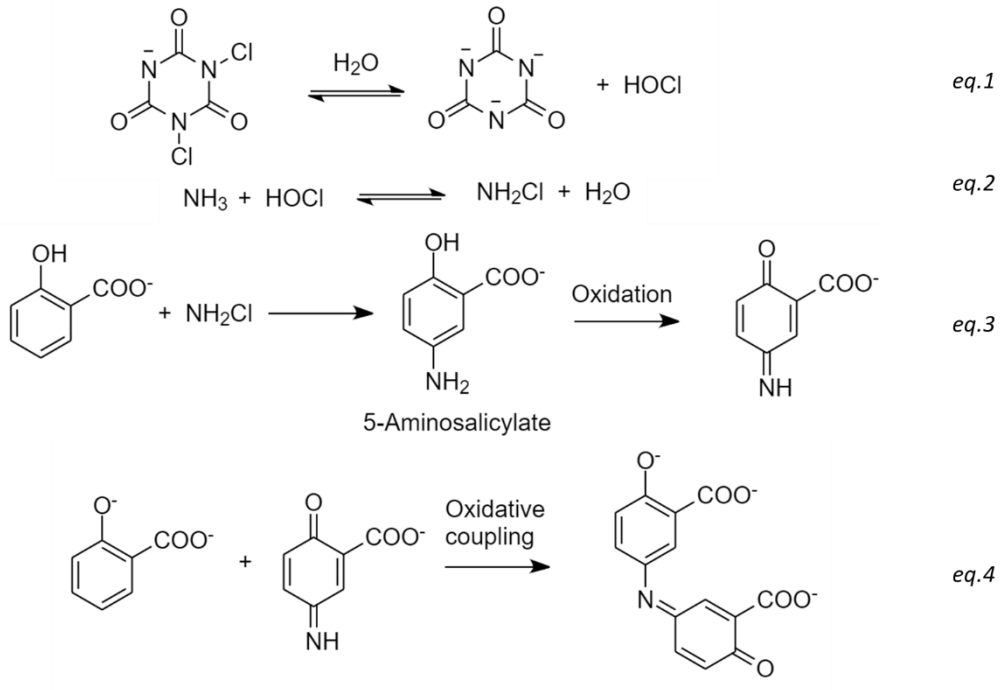

1.6.3 Fluorometric method[59]

The fluoresent product exhibits the maximum excitation wavelength at 362 nm and the maxinum emission wavelength at 423 nm, this specific spestral charicteriscs can be used for NH_3 quantification in solutions. The detection limit by fluorometric method is tipiclly in the order of μg-NH_4^+/L that the sensitivity is much higer than indophenol method. This method was developed for flow injection analysis and could be applied to sea and estuarine water.[60] Amines are the potential interference in this method. The comparison of Nessler's method, indophenol method and fluorometric method is summarized in Table 2.

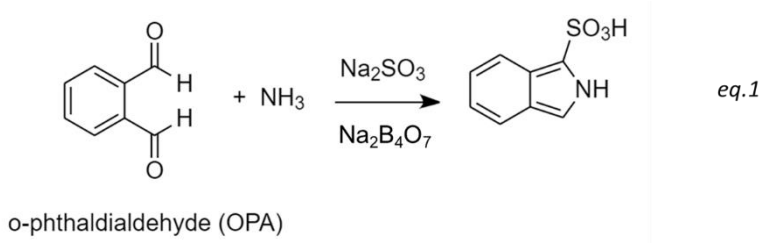

Table 2 Summary of colorimetric methods for NH_3 quantification.

	Nessler's Method	Indophenol Method	Fluorometric method
Sensitivity	Low →		High
Interference	Metal cations, N_2H_4	Excess N_2H_4, nitrates	Amines

1.6.4 ^{1}H NMR

Proton nuclear magnetic resonance (^{1}H NMR) with chemical shifts and spin-spin couplings give the information of the chemical structure. The diagnostic $^{14}NH_4^+$ triplet peaks appear at 7.29 ppm.[61]

1.6.5 Isotopic labelling

^{15}N isotopic labelling is strongly recommended, and the formed $^{15}NH_4^+$ product has high sensitivity with ^{1}H NMR or mass-spectroscopy. In the ^{1}H NMR spectra of $^{15}NH_4^+$ and $^{14}NH_4^+$ of 1mg/L concentration, $^{14}NH_4^+$ shows triplet peaks in the range of 6.8-7.05 ppm,

while $^{14}NH_4^+$ shows doublet peaks.[62]

1.6.6 Ion chromatography

Ion chromatography is a method for separating ions in an aqueous solution which is called mobile phase. The mobile phase is constantly fed into the column packed with ion exchange resin, which is called the stationary phase. Ions are separated by their different affinity with the stationary phase.[63]

1.6.7 Conductivity method

The principle of the conductivity method is that the electrical conductance of a standard acid solution decreases as NH_3 is absorbed.[64] For NH_3 absorbed in sulfuric acid given as:

$$2NH_3 + H_2SO_4 \rightarrow (NH_4)_2SO_4$$

Protons in the acid solution are changed into NH_4^+ ions, and conductance decreases because the mobility of NH_4^+ is lower than proton. Mobilities are listed in Table 3. Based on the conductivity change of the acid solution, the absorbed amount of NH_3 can be quantified. The continuous conductivity method is fast and simple.

Table 3 Mobilities of proton, SO_4^{2-} and NH_4^+.[64]

Ions	Mobility
H^+	350
SO_4^{2-}	78
NH_4^+	74.5

1.6.8 N_2H_4 determination method

The reaction between N_2H_4 and p-dimethylaminobenzaldehyde to form an azine complex with the yellow color change has a high selectivity and sensitivity. This N_2H_4 determination method is commonly called Watt and Chrisp's method which is investigated at 1952. The colored azine complex exhibits a maximum absorption wavelength at 455 nm, and typically has a detection limit at the order of μg-N_2H_4/L. in addition, there is almost no intereference in this method only if the solution contains access NH_3 (a higher concentration than 10 mg-NH_3/L for example).

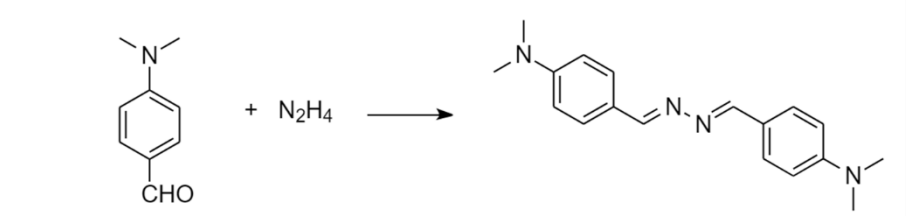

p-Dimethylaminobenzaldehyde

eq.1

1.7 Control experiments

The reported electrochemical NH_3 production rates are typically in the range of 10^{-13}-10^{-8} mol/(s cm^2), which are very small compared with the quantity of NH_3 in the laboratory environment and lead to hard NRR proof. The N-containing contaminants are common in catalysts or electrolytes precursors, reactant gases, experimental equipment and even from human breath. Some recent works recommend rigorous NRR experimental and NH_3 quantification protocol,[65] [66] [67] which includes following tests and controls.

- N-containing materials

In some cases, the active catalysts are N-containing materials, or the precursors and solvents at any step of the electrolytes and catalysts synthesis are N-containing materials such as nitrates and amines, those contaminants can be the sources of detected NH_3. Repeatedly Ar control experiments are desired in these cases.

- Gas purification

NO_x contaminants in the N_2 (even in $^{15}N_2$) gas supply can be reduced electrochemically to NH_3. Therefore, the reactant gas supply is desired to be purified in order to remove the containing NH_3 as well as NO_x.

- Ar control experiments

Ar control experiments are carried out to exclude the possibility of ambient NH_3 absorption in the gas lines, catalyst surface and accumulated environment NH_3 on the surface of the NH_3 trap.

- Open circuit control experiments

Open circuit control experiments under reactant gases are carried out to exclude NH_3 and NO_x in the N_2 supply. In addition, in the case of two chamber reactor, the N_2 supply chamber and H_2 supply chamber are separate, the open circuit control experiments can

examine whether the gas leakage between the anode and cathode chambers could cause catalytic NH_3 production.

- Isotopic-labeled $^{15}N_2$ tests

With isotopic-labeled $^{15}N_2$ tests, $^{14}NH_4^+$ can be quantify separately from $^{15}NH_4^+$ using ^1H NMR. It is also helpful for mechanism study.

- Reproducibility

Since NH_3 production rates and current densities are typically small in most cases, errors in individual data are significant. It is desired to reproduce the data under same conditions and give the standard deviations as error bars.

1.8 Research objectives and Outline

The objective of this work is to develop electrolysis cells with higher NH_3 production rate, and higher selectivity. In order to achieve this goal, the following tasks will be conducted.

- Preparation of appropriate cathode catalysts. → [Chapter 2]

In this work, I focused on Fe, which has high N_2 dissociation activity via an associative mechanism. To improve the proton conductivity, Fe was mixed and sintered with BZY, which is a proton conductor. To further increase the durability of the cathode catalyst, Ru was added.

- Investigation of the reaction mechanism. → [Chapters 3, 4, 5]

It is important to investigate the reaction mechanism for improving selectivity and production rate of the catalyst. For the experiments with the double-chamber setup carried out at 220 °C, not only NH_3 but also N_2H_4 was detected from the productions. In order to investigate the intermediates on the surface of the cathode catalyst, the potentiostatic pulse experiment was conducted, and the current change over time was fitted with a new model suggested in this work. For the experiments with the single-chamber setup carried out at 500 °C, the reaction rate change over time was fitted with the model of the reaction rate equations. In addition to the simulations based on the above models, *in situ* DRIFT was applied to directly observe the adsorbed species on the catalyst surface.

Chapter 2: Cathode catalyst

In this work, Fe was selected as the NRR catalyst. As an acceptant cathode catalyst for NRR, such materials are expected to have (1) NRR catalytic activity, (2) electronic conductivity, and (3) proton conductivity. In order to add proton conductivity to metal Fe, which already has an electronic conductivity, a proton conductor yttrium-doped barium zirconate with Y dopant concentration of 0.2 ($BaZr_{0.8}Y_{0.2}O_{3-\delta}$) was added. $BaZr_{0.8}Y_{0.2}O_{3-\delta}$ (BZY20), as an electrolyte material with perovskite structure for proton conducting fuel cells, exhibits high bulk proton conductivity in intermediate temperature range, as well as high chemical stability and excellent mechanical strength.[68] The following is a detailed description of the preparation and characterization of the catalysts. In this chapter, all the symbol BZY represents BZY20.

2.1 Experimental

The $BaZr_{0.8}Y_{0.2}O_{3-\delta}$ powder was prepared by a conventional solid-state reaction. The reagents used were $BaCO_3$ (98% purity, Wako Pure Chemical Industries Ltd, Osaka, Japan), Y_2O_3 (99.9% purity, Wako Pure Chemical Industries Ltd, Osaka, Japan), and ZrO_2 (98% purity, Wako Pure Chemical Industries Ltd, Osaka, Japan). The materials were mixed in stoichiometric quantities and ball milled in ethanol overnight. After drying, the precursor was calcined at 1400 °C for 12 h to yield the BZY powder. The BZY powder and α-Fe_2O_3 (20–40 nm, Wako Pure Chemical Industries Ltd, Tokyo, Japan) were mixed in a weight ratio of 1 : 4 and ball milled in ethanol overnight. After drying, the mixture was sintered at 1300 °C for 12 h to form an α-Fe_2O_3/BZY composite. The resultant α-Fe_2O_3/BZY composite was reduced in H_2 atmosphere at 500 °C for 1 h and cooled to 25 °C under N_2.[69]

In CsH_2PO_4/SiP_2O_7-used cell, in order to suppress the oxidation of Fe, the reduced α-Fe_2O_3/BZY was mixed with RuO_2 (Practical Grade, Wako Pure Chemical Industries Ltd, Osaka, Japan) and ground to fabricate the cathode materials.

2.2 Characteristics

X-ray diffraction was performed at 100 kV and 40 mA in the 2θ range of 20–80° (XRD, Rigaku RINT 2400). The cross-sectional morphologies of the electrolysis cells were observed by scanning electron microscopy (SEM, Hitachi S-4700, Tokyo, Japan) and energy dispersive X-ray spectroscopy (EDX, Super Xerophy, Horiba, Kyoto, Japan). Temperature-programmed reduction (TPR) experiments were performed in a flow system (Quantachrome, CHEMBET-3000, Florida, USA). To confirm that the addition of the Ru species could suppress the oxidation of Fe, the samples were pretreated at 220 °C for 30 min in Ar at a flow rate of 50 mL min^{-1} and heating rate of 10 °C min^{-1} and cooled to room temperature. After flushing with diluted H_2 (5% H_2 in Ar) at a flow rate of 50 mL min^{-1} for 1 h, the samples were heated to 220 °C at a heating rate of 10 °C min^{-1} and reduced for 1 h. After flushing with Ar at a flow rate of 50 mL min^{-1} for 30 min, the samples were oxidized in diluted O_2 (5% O_2 in He) at a flow rate of 50 mL min^{-1} for 30 min and cooled to room temperature in Ar. The samples were again flushed with diluted H_2 and heated to 1000 °C.

XRD patterns of the α-Fe_2O_3, BZY, and Fe_2O_3/BZY composites are shown in Fig. 3. In Fig. 3 (b), all the peaks could be assigned to those of a typical perovskite structure, suggesting that BZY was successfully synthesized. According to Fig. 3 (d), after the mixture of BZY powder and α-Fe_2O_3 was sintered at 1300 °C, some of the BZY was decomposed into carbonates and oxides, and the phase transition of α-Fe_2O_3 to ε-Fe_2O_3 and γ-Fe_2O_3 occurred simultaneously. The iron oxides were reduced to a metallic state, as shown in Fig. 3 (c). In contrast, the perovskite structure in the composite remained stable after the reduction treatment.

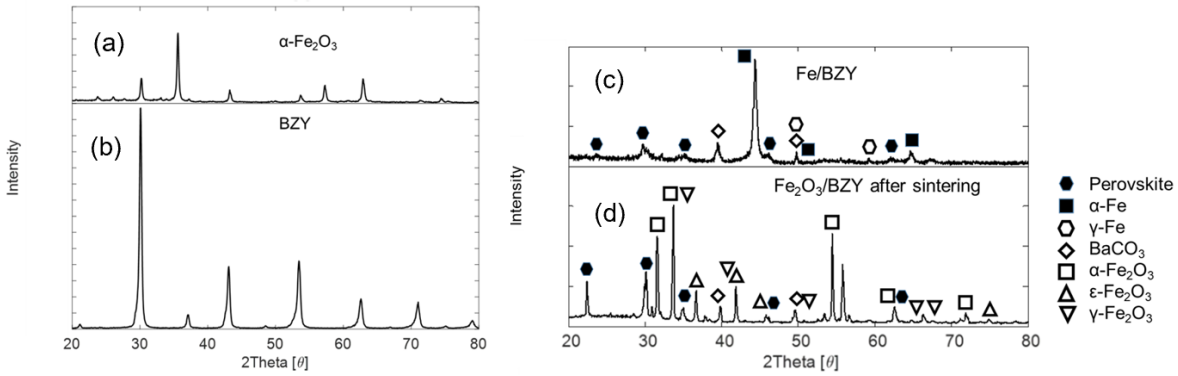

Figure 3 XRD patterns of (a) as-obtained α-Fe_2O_3, (b) as-calcined BZY powders, (c) Fe_2O_3/BZY reduced at 500 °C for 1 h, and (d) as-synthesized Fe_2O_3/BZY at a weight ratio of 4:1 and calcined at 1300 °C for 12 h in air.

Morphology of cross section in Fig. 4 indicates a dense structure of sintered Fe_2O_3/BZY. After electrocatalytic reaction, spent Fe/BZY became porous, and different shapes, such as blocks, layers, particles, coexisted in Fig. 5. Most interestingly, several hexagons with diameters of less than 2 μm distributed on the surfaces of blocks in Fig. 5 (c). Those hexagons are inferred to be γ-Fe, which has fcc phase and exists at high temperature and low pressure.[70] γ-Fe and α-Fe with bcc phase coexist at about 600 ˚C.[71] Effect of applied voltage might lead to phase transformation from α-Fe to γ-Fe at 500 ˚C, ambient pressure.

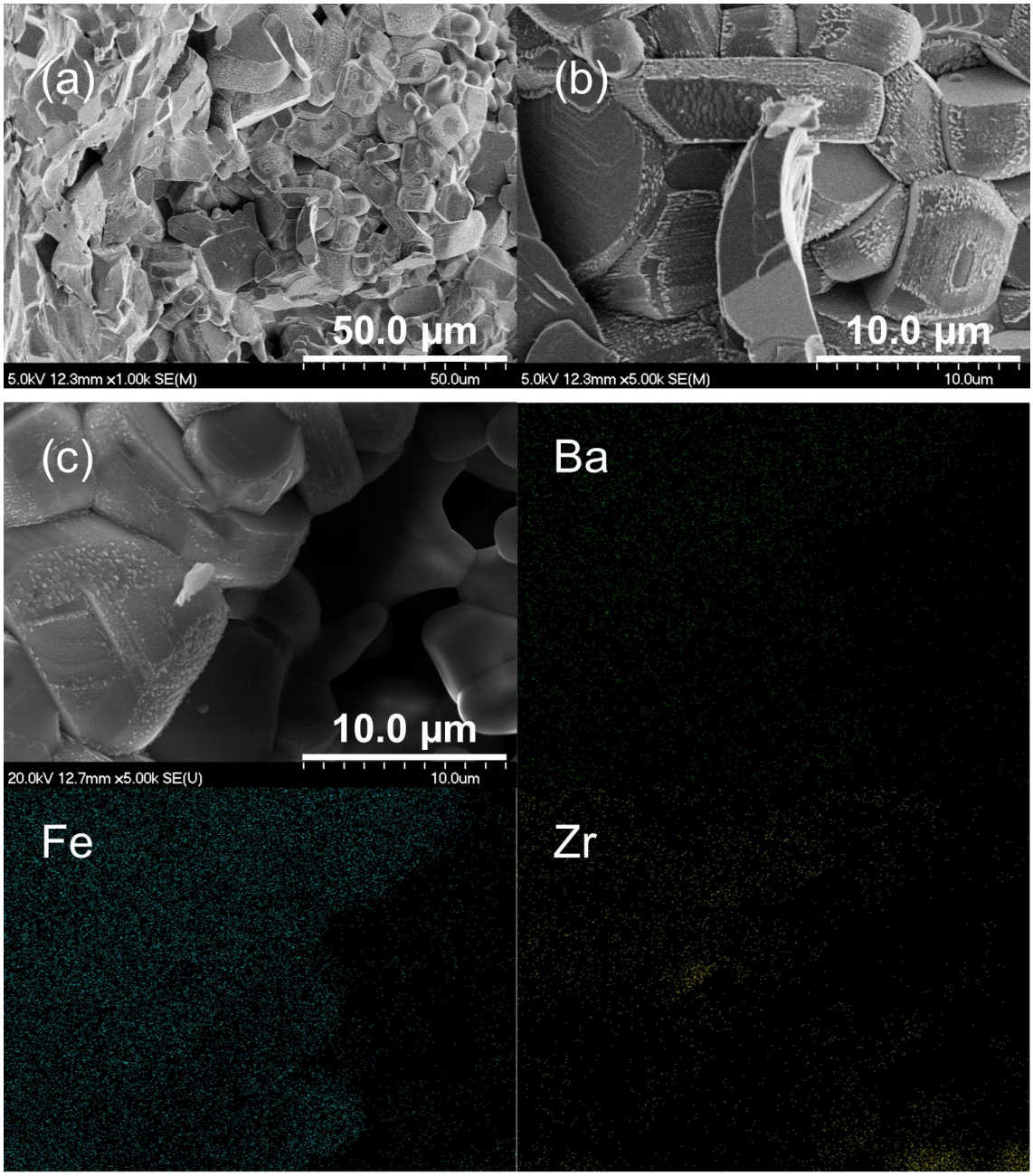

Figure 4 (a), (b), (c) Cross sectional SEM-EDS images of the sintered Fe_2O_3/BZY disk with weight ratio of 4:1 and corresponding EDX mapping of Ba, Fe and Zr.

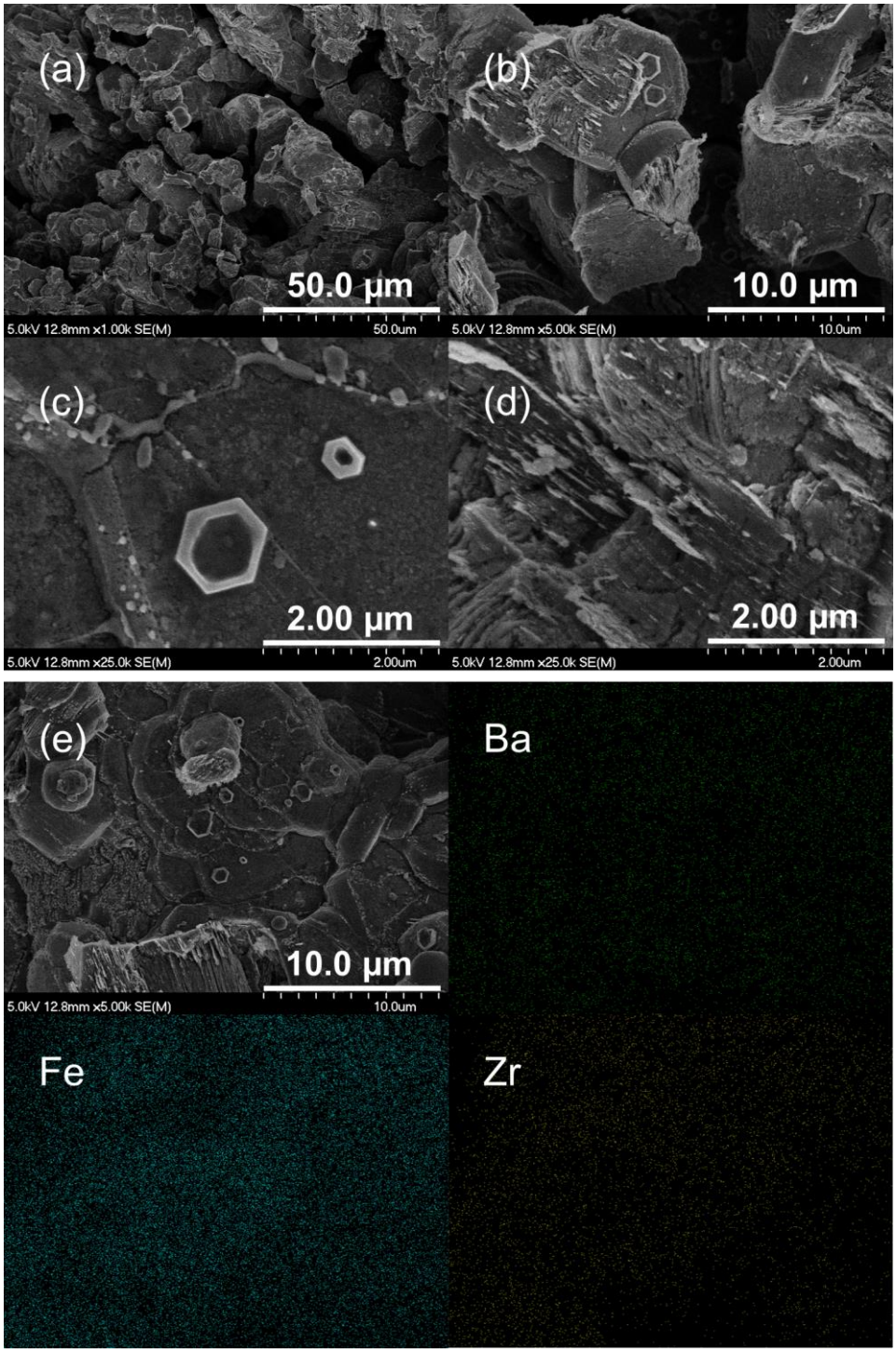

Figure 5 (a), (b), (c), (d), (e) SEM-EDS images of the reduced Fe/BZY (reduced from Fe_2O_3/BZY disk with weight ratio of 4:1) and corresponding EDX mapping of Ba, Fe and Zr. Hexagons can be observed in (b), (c), and (e).

The reducibility of Fe/BZY and Fe/BZY–RuO_2 was investigated by TPR by the procedures shown in Fig. 6. In the TPR profile, a sharp peak appears at low temperatures and a broad peak appears at high temperatures. The low temperature peak exists only in the profile of the RuO_2-containing catalysts, whereas the high temperature peak is observed in the Fe/BZY-containing catalysts. Accordingly, the low- and high-temperature peaks are attributed to the reduction of the RuO_2 and iron oxide species, respectively. The low temperature peaks, indicated by Fig. 7 (a), (b)-① and ② in the TPR profiles, correspond to the reduction of the RuO_2 oxidized by the dilute O_2/He gas at 220 °C. The reduction temperatures of RuO_2 in Fig. 7 (b)-① are lower than those shown in Fig. 7 (a)-②, which implies that fresh RuO_2 is more easily reduced. The TPR profile of Fe/BZY shown in Fig. 7 (a)-③, ④ indicates that the iron component in the prepared Fe/BZY was partially oxidized in ambient atmosphere. The high temperature peaks, indicated by Fig. 7 (b)-③, ④ in the TPR profile, can most likely be assigned to the reduction of Fe_2O_3 to Fe_3O_4. The peaks indicated by Fig. 7 (b)-⑤, ⑥ are derived from the reduction of Fe_3O_4 to Fe. Only in the TPR profile of Fe/BZY–RuO_2 (red) in Fig. 7 (b)-⑦ is a new peak observed at 186 °C. This peak could stem from the reduction of the fresh Fe_2O_3 formed on the surface of Fe in dilute O_2/He gas at 220 °C. It follows that with the addition of RuO_2 (the RuO_2 is partially reduced by H_2 generated at the cathode), the *in situ* oxidized Fe, which most likely forms by the steam present under the electrolysis conditions, could be reduced at 220 °C, and thus the activity of the Fe/BZY catalyst could be regained.

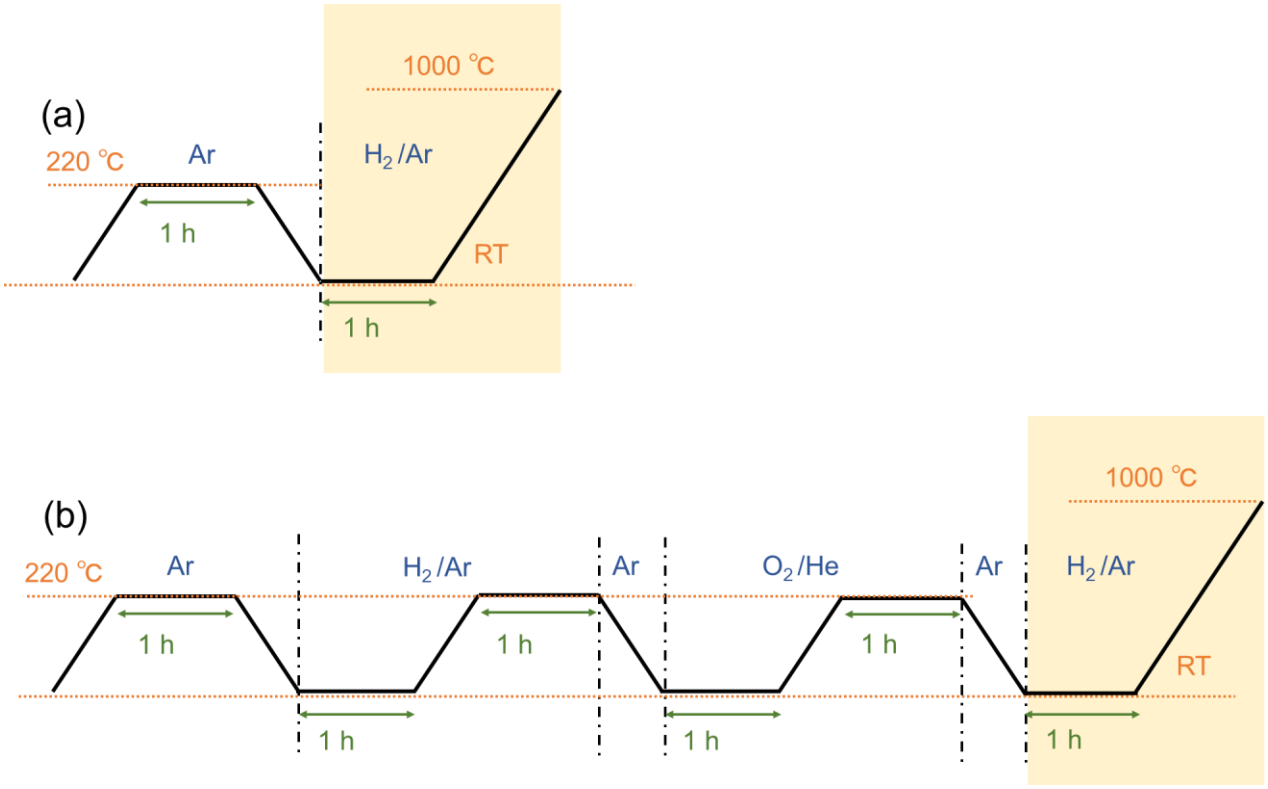

Figure 6 Procedures for TPR measurement. (a) Pretreatment, reduction process (without oxidization process). (b) Pretreatment, reduction, oxidization, reduction process.

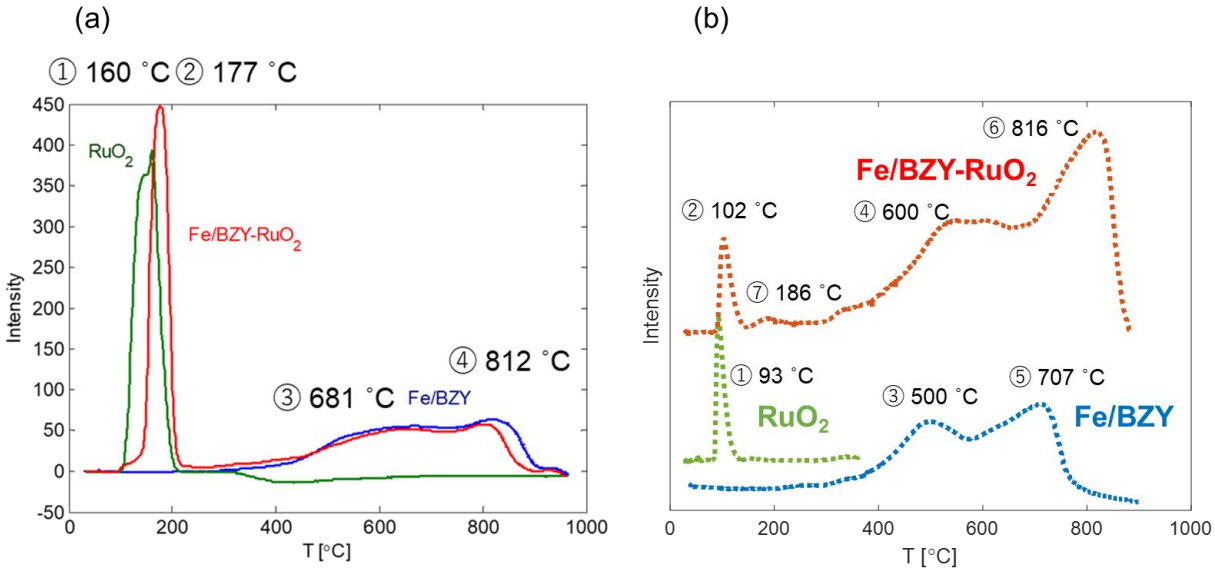

Figure 7 TPR results of (a) 5 mg RuO_2 (green), 30 mg Fe/BZY (blue), 5 mg RuO_2 and 30 mg Fe/BZY mixture (red) followed the procedure in Fig. 6 (a). (b) 5 mg RuO_2 (green), 5 mg Fe/BZY (blue), 5 mg RuO_2, and 5 mg of the Fe/BZY mixture (red) followed the procedure in Fig. 6 (b).

2.3 Catalytic activity

The catalytic activity of Fe/BZY was confirmed under 10 ml/min N_2 and 30 ml/min H_2 feeding gas at 500 °C. Catalytic reaction procedures were shown in Fig. 8, amount of 0.19 g prepared catalyst grains was used and outlet gases were trapped by distilled water in a water trap for 3 min with a 30 min interval. Before the catalytic reaction, catalyst was reduced in 30 ml/min H_2 flow for 30 min. Diameters of the grains were about 2 mm, and the reaction was carried out at ambient atmosphere. the results of catalytic NH_3 production rate by Fe/BZY are shown in Table 4.

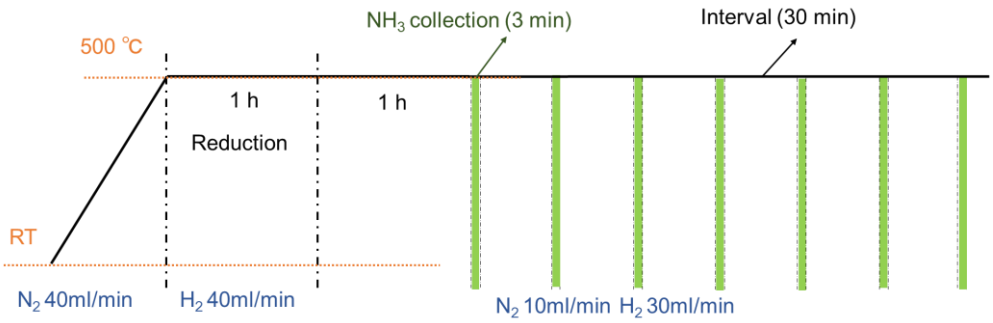

Figure 8 Catalytic reaction procedures. The green traps stand for NH_3 collection periods.

Table 4 Catalytic NH_3 production rate by Fe/BZY at 500 °C.

Cycle	1	2	3	4	5	6
Reaction rate [mol/(s·g-cat.)]	6.5×10^{-8}	2.3×10^{-8}	4.1×10^{-8}	2.8×10^{-8}	5.7×10^{-8}	4.6×10^{-8}

Commercial α-Fe_2O_3 and Fe_2O_3/BZY without reduction process were also tested under the same conditions. As the results, Fe_2O_3/BZY without reduction exhibited no NRR activity. The average reaction rate by commercial α-Fe_2O_3 was 2.2 mol/(s·g-cat.), which was lower than by Fe/BZY. The as-prepared Fe/BZY presented a high NRR catalytic activity, cations such as Ba^{2+} in the catalyst composites can play a role as promoter.[72] Other catalysts formed by the mixture of α-Fe_2O_3 and oxides were also tested by the same procedures in Fig. 8, and results are listed in Table 5.

Table 5 Catalytic activities of the α-Fe_2O_3 and the mixture of α-Fe_2O_3 and oxides at 500 °C.

Activities at 500 °C Reduced at 500 °C	**Reaction rate (mol g-cat^{-1} s^{-1})**	**Reaction rate (mol g-Fe^{-1} s^{-1})**
Nano α-Fe_2O_3	2.2×10^{-8}	3.1×10^{-8}
Sintered α-Fe_2O_3	1.1×10^{-8}	1.6×10^{-8}
Sintered α-Fe_2O_3/ Y_2O_3 (1:1)	0	0
Sintered α-Fe_2O_3/$BaCO_3$ (1:1)	0	0
Sintered α-Fe_2O_3/ ZrO_2 (1:1)	2.1×10^{-8}	5.9×10^{-8}
Sintered α-Fe_2O_3/ ZrO_2 (3:1)	3.8×10^{-8}	7.3×10^{-8}
Sintered α-Fe_2O_3 /BZY (2:1)	0	0
Sintered α-Fe_2O_3/BZY (4:1)	4.3×10^{-8}	7.7×10^{-8}

2.4 Electronic conductivity of Fe_2O_3/BZY with different mixing rate

The electronic properties of Fe_2O_3/BZY without reduction were also studied. Normally, Fe_2O_3 can be thought as a semiconductor, and BZY is an insulator. In this work, it was investigated that Fe_2O_3/BZY composites with different weight mixing ratio exhibited different electronic conductivity at room temperature. Moreover, the electronic conductivity of Fe_2O_3/BZY composites increased along with the rise of sintering temperature. Fig. 9 shows the conductivities measured under ambient atmosphere and the fitting curves applied by the binary-phase EMA. the EMA model is described in Appendix. 6. Here, the symbol p is the volume fraction of BZY. As the Fe_2O_3/BZY mixture was prepared by mixing in weight proportions, the following calculation were conducted to determine the volume fraction of BZY.

$$p_{BZY} = \frac{m_{BZY}}{\rho_{BZY}} / V_{pellet}$$

The mass of the BZY used is m_{BZY}, and ρ_{BZY} is calculated from the density of sintered BZY, which is 5.90 g/cm^3. The V_{pellet} is the volume of sintered Fe_2O_3/BZY. The simulation results were shown in Fig. 10. The adopted parameters are m = 2.17, σ_0 = 1.00 × 10^{-9} S/cm and σ_2 = 1.48 × 10^{-7} S/cm for samples sintered at 1250 ˚C, and m = 2.45, σ_0 = 1.00 × 10^{-9} S/m and σ_2 = 2.85 × 10^{-7} S/m for samples sintered at 1400 ˚C. The largest conductivities will be achieved where p = 0.14 at 1250 ˚C samples, and p = 0.07 at 1400 ˚C samples from the fitting curves. The value of m at 1400 ˚C samples is larger than at 1250 ˚C samples imply not only the interfacial conductivity increased but also the boundary layer got thicker at higher temperature. Fitting results of 1250 ˚C samples show greater loss than 1400 ˚C samples. The fitting losses are due to the chemical reaction between BZY and Fe_2O_3 during sintering, resulting in the presence of multiple substances with different conductivities within the mixture, however the EMA

calculations are approximated using a binary-phase mixture. The pellets of the same composition at 1250 ˚C were lower than those at 1400 ˚C and resulted in more fitting losses, probably due to the larger spacing among different phases as well as the multiphase substances in the pellets.

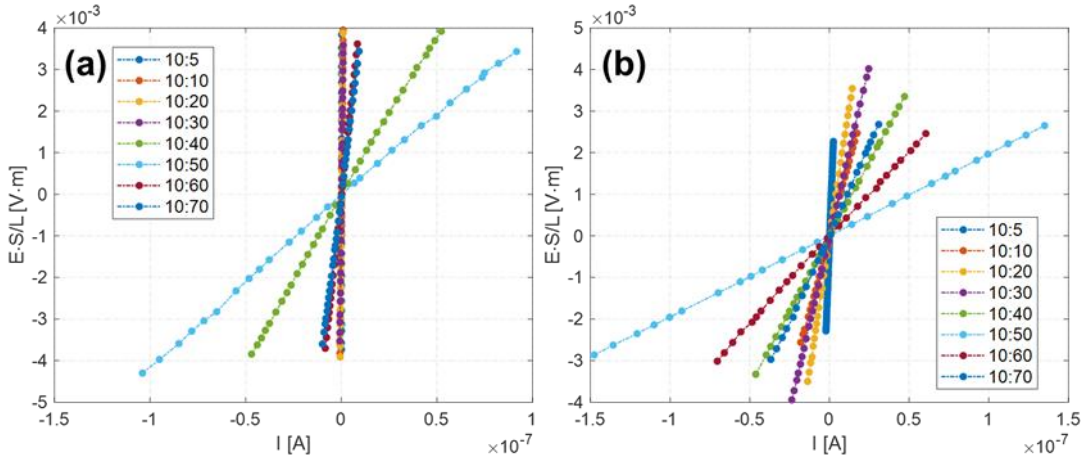

Figure 9 The IV curves of (a) Sintered at 1250 ˚C, and (b) Sintered at 1400 ˚C with different weight ratios. In order to compare pellets with different shapes, the voltage (E) was multiplied by S/L. S is the area of the pellet, and L is the thickness.

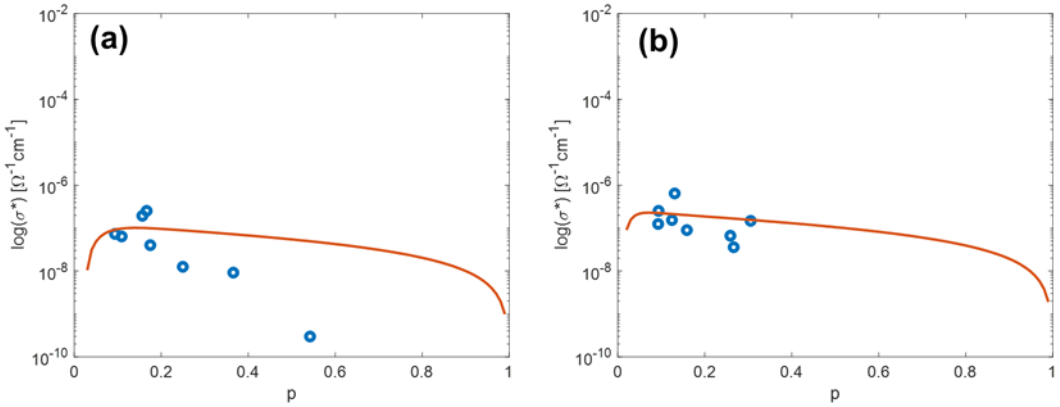

Figure 10 The electronic conductivities of Fe_2O_3/BZY sintered at (a) 1250 ˚C. (b) 1400 ˚C. The symbol p means the volume fraction of the insulator BZY. Bule circles are experimental data, and the red line is the simulation curve.

2.5 Summary and prospects

A suitable cathode catalyst for N_2 reduction must have a combination of catalytic activity, electronic conductivity and proton conductivity as shown in Fig. 11. Fe is an industrial catalyst for NH_3 production based on Haber-Bosch process. Therefore, Fe is a material that has catalytic activity and electronic conductivity. In order to add proton conductivity to Fe, Fe was composited with BZY, which exhibits proton conductivity. In addition, basic Ba^{2+} is expected to act a promoter. Due to the difficult of mixing the metallic Fe and the oxide BZY homogeneously, an Fe_2O_3/BZY composite was produced by sintering. Then the Fe_2O_3/BZY precursor was reduced in H_2 flow to form metallic Fe, and the as-prepared catalyst was called Fe/BZY. The preparation process is illustrated in Fig. 12. From the characteristic results, not only α-Fe, but also γ-Fe exited in Fe/BZY. For electrochemical NH_3 synthesis with CDP electrolyte, as water vapor was introduced into the reactor, Fe is easily oxidized and loses its activity. In order to prevent the oxidation of Fe, Ru was added to Fe/BZY. The spillover effect of Ru is expected to prevent the oxidation of Fe, which was confirmed by the H_2-TPR experiments.

In order to increase the activity of the catalyst, it is possible to increase the porosity of the catalyst. The fractal bodies such as the Menger sponges have extremely high porosity, surface area, and can create novel functions. H. Mayama *et al.*[73] reported Menger sponge-like fractal body created by a novel templated method. In this study, AKD, a kind of wax, was used to spontaneously form the fractal particles, and then was added to the sol-gel, finally, the particles were removed to form a porous fractal body. Referring to this method, a sol-gel could be made by gradually adding a basic solution such as NaOH to a solution of $FeCl_3$, $BaCl_2$, $ZrOCl_2$ and YCl_3. Then the formed sol-gel will be cooled and water crystallizes into ice. After the frozen so-gel is melted, a porous fractal body will be formed.

Except for Fe/BZY, the electronic property of Fe_2O_3/BZY was also studied. Although Fe_2O_3/BZY was not applied in this work, the characteristics of this material make it promising for used as an electronic conductor with high stability in oxidizing atmosphere.

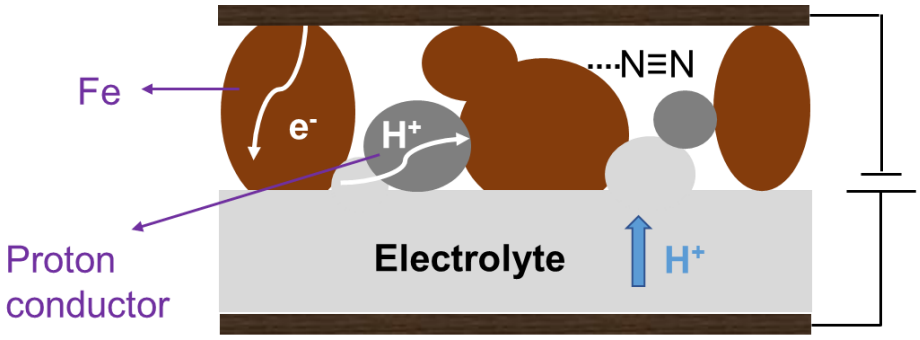

Figure 11 Schematic imagine of the preferred cathode catalyst with electronic conductivity, proton conductivity and catalytic activity.

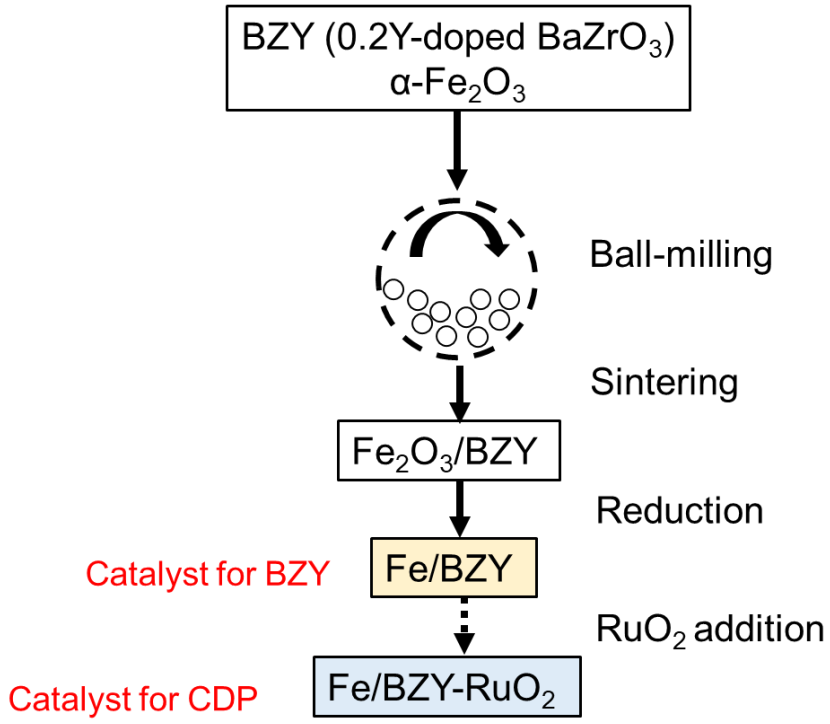

Figure 12 Catalyst preparation process. Produced Fe/BZY catalyst was used for NH_3 synthesis activation test, and used as cathode catalyst with BZY and CDP electrolyte. Fe/BZY with the addition of RuO_2 was used as cathode catalyst with CDP electrolyte.

Chapter 3: Electrocatalytic nitrogen reduction using CsH_2PO_4/SiP_2O_7 electrolyte

3.1 Experimental

3.1.1 Preparation of electrolysis cell

CsH_2PO_4 was prepared using Cs_2CO_3 (Wako 1st Grade, Wako Pure Chemical Industries Ltd, Osaka, Japan) and H_3PO_4 (85 wt% in water, Sigma-Aldrich Co. LLC, Missouri, USA) in stoichiometric quantities. After dissolution in distilled water, the precursor was dried at 120 °C overnight. SiP_2O_7 was prepared from SiO_2 (99.9% purity, Wako Pure Chemical Industries Ltd, Osaka, Japan) and H_3PO_4 as follows: SiO_2 and H_3PO_4 were mixed in a molar ratio of 1 : 2.5, and heated at 200 °C for 3 h. After drying at 100 °C for 24 h, the precursor was ground into a powder and heated at 122 °C for 24 h. Finally, the powder was calcined at 700 °C for 3 h to attain the SiP_2O_7 phase. Subsequently, the prepared CsH_2PO_4 and SiP_2O_7 were mixed in a molar ratio of 1:1 and ground to form the CsH_2PO_4/SiP_2O_7 composite. The preparation method of the cathode catalyst was described in Chapter 2.

The CsH_2PO_4/SiP_2O_7 powder was pressed into a ⌀20 mm disk. The reduced α-Fe_2O_3/BZY (0.075 g) and RuO_2 (0.075 g) powders were mixed and loaded on the cathode side of the CsH_2PO_4/SiP_2O_7 disk and pressed at a pressure of 20 MPa for 10 min. Porous carbon paper (⌀10 mm, TGP-H-120, Toray Industries, Inc., Tokyo, Japan) was used as the current collector on the cathode side. A Pt/C loaded carbon paper of ⌀10 mm (Pt loading of 1 mg cm^{-2}, Miclab, Kanagawa, Japan) was used as the anode catalyst. Pt wires connected to the Pt mesh or Pt/C were used as the terminal on the anode side, while the Pt wires connected to the carbon paper acted as the terminal on the cathode side.

Polytetrafluoroethylene (PTFE) sheet (Gore Hyper-Sheet Gasket, W. L. Gore & Associate, Inc., Delaware, USA) layers with an appropriate thickness were used as the gas seal. Figure 14 shows a schematic of the electrolysis cell.

3.1.2 Pretreatment of the cell

The cell was heated from 25 °C to 220 °C at a heating rate of 2.8 °C/min, with a gas flow of dry N_2 on the cathode side and dry Ar on the anode side from 25 °C to 120 °C in a double-chamber reactor as illustrated in Fig. 13. From 120 °C to 220 °C, humidified H_2 gas was fed to the anode. In the steady state, a voltage of -2 V (vs. OCV) was applied to the cell for 1 h to reduce RuO_2.

3.1.3 Blank experiments

The following three blank experiments were conducted at 220 °C at OCV conditions before performing the reaction tests. Blank experiment 1 was conducted using a gas flow of 3%-humidified H_2 on the anode side and dry N_2 on the cathode side. Blank experiment 2 was performed with a gas flow of 20%-humidified Ar on the anode side and dry Ar on the cathode side. Blank experiment 3 was conducted with a gas flow of 20%-humidified Ar on the anode side and dry N_2 on the cathode side. Electrolysis was performed under the same conditions as Blank experiment 1. A direct current voltage vs. OCV was applied between the anode and cathode under potentiostatic conditions. The total gas flow rate was kept constant at 25 mL (STP)/min on both sides. The outlet gases were trapped in a distilled water trap for 30 min. The amount of NH_3 and hydrazine in the distilled water

trap was quantified by the salicylate method and Watt and Chrisp's method.

An error in quantification might occur if NH_3 from the ambient atmosphere adsorbs on the cell or NH_3 is absorbed by the water trap. Accordingly, three kinds of blank experiments were conducted under open-circuit conditions. Blank experiments 1 and 2 were intended to exclude the possibility of ambient NH_3 absorption in the water trap. Blank experiment 3 aimed to examine whether the gas leakage between the anode and cathode chambers could cause catalytic NH_3 production in the H_2 and N_2 gas flows to the anode and cathode, respectively. The amount of trapped NH_3 during the blank experiments, which included a collection time of 30 min, was below the detection limit (0.01 mg-N/L, equivalent to 2.5×10^{-11} mol/(s·cm^2)). Therefore, both the ambient and catalytically generated NH_3 could be ignored. Furthermore, N_2H_4 could not be detected in the blank experiments, which suggests that the colorimetric error due to other factors could be ignored (1 μg N_2H_4/L is equivalent to 1.1×10^{-12} mol/(s·cm^2)) (Table S 1). Since the reagents used to synthesize the catalyst and electrolyte did not contain any N, the origin of NH_3 could be confirmed to be from the reaction of the feeding N_2 gas flow. The results of blank experiments are summarized in Table 6, and the experimental procedures are shown in Fig. 15.

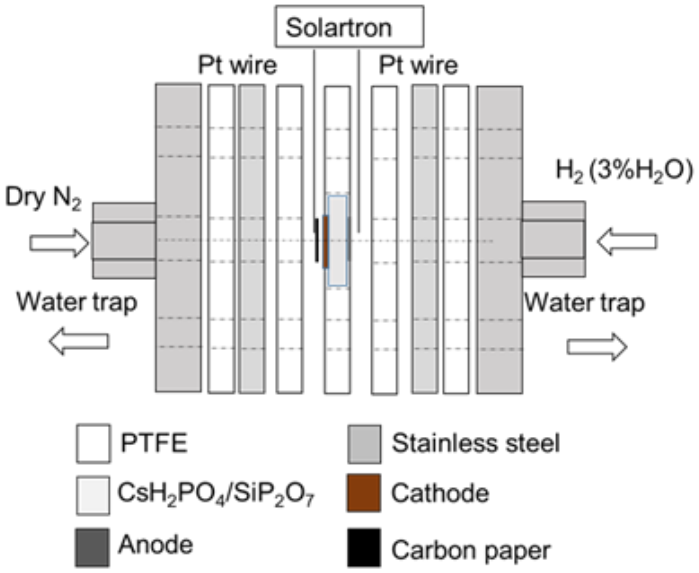

Figure 13 Illustration of the two-chamber setup.

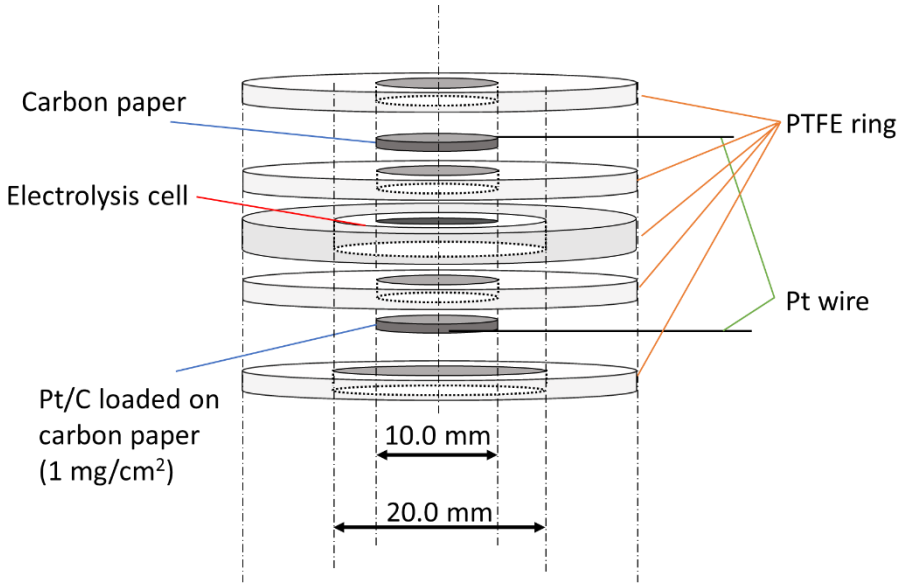

Figure 14 A schematic of electrolysis cell.

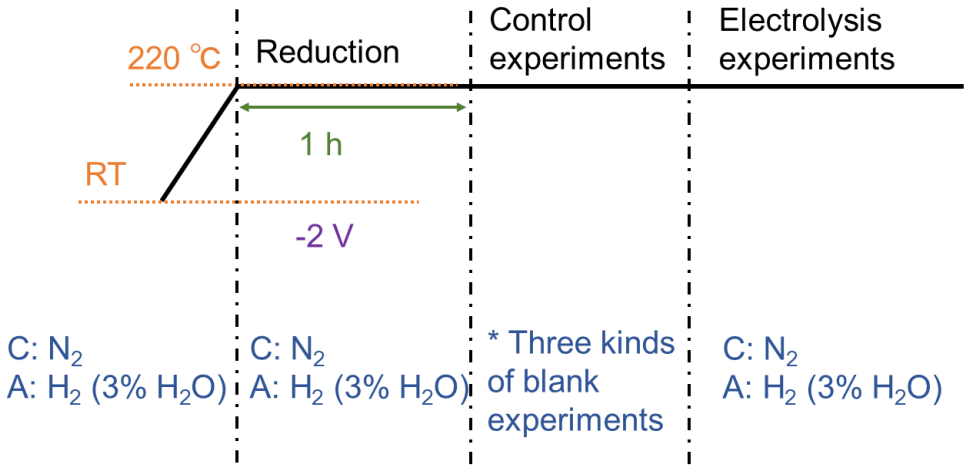

Figure 15 Experimental procedures of electrochemical NH_3 synthesis with CDP cell.

Table 6 Blank experiments results for NH_3 contamination from the atmosphere and catalytic NH_3 formation from gas leakage between anode and cathode are below the detection limit (BLD).

		Collected on cathode side [mol/(s·cm^2)]		Collected on anode side [mol/(s·cm^2)]	
		NH_3	N_2H_4	NH_3	N_2H_4
Blank exp. 1	Anode: Ar (20%H_2O)	BLD	BLD	BLD	BLD
	Cathode: dry N_2	BLD	BLD	BLD	BLD
Blank exp. 2	Anode: Ar (20%H_2O)	BLD	BLD	BLD	BLD
	Cathode: dry Ar	BLD	BLD	BLD	BLD
Blank exp. 3	Anode: H_2 (3% H_2O)	BLD	BLD	BLD	BLD
	Cathode: dry N_2	BLD	BLD	BLD	BLD

3.2 Results and discussion

3.2.1 Characteristics

Figure 16 shows the SEM-EDS cross-sectional images of the electrolysis cells containing the Fe_2O_3/BZY-RuO_2 cathode catalyst. It is evident from Fig. 16 (a) and (b) that the cathode catalyst layer reduced in size after the electrolysis reaction, which probably resulted from the reduction of RuO_2. In addition, it is clear that the particle size of the cathode catalyst increased after electrolysis. The particle size increase is also supported by the EDS mapping images of the Ru species (Fig. 16 (c) and (d)), which indicates that a slight aggregation of the Ru species occurred during the pre-reduction treatment and electrolysis reaction. The aggregation might have been caused by the reduction of RuO_2 and the NRR on the active sites. Nevertheless, even after the electrolysis reaction, the Ru species were uniformly dispersed over Fe/BZY, as indicated in the magnified SEM-EDS image (Fig. 16 (e)). There seems to be no clear interpenetration of the electrolyte material into the cathode catalyst layer after electrolysis because the distribution of P, Si, and Cs is confined to the electrolyte phase before and after the electrolysis test, as shown in Fig. 16 (c) and (d). This implies that no reaction occurred between the acidic electrolyte material and cathode catalyst. In some fuel cells where caesium phosphate-based electrolytes are used, the electrolyte materials penetrate the electrode layers after current loading.[74] This is because the wettability of the electrolyte materials towards the electrocatalyst materials is low, and accordingly the electrolyte materials are retained within the electrolyte layer.

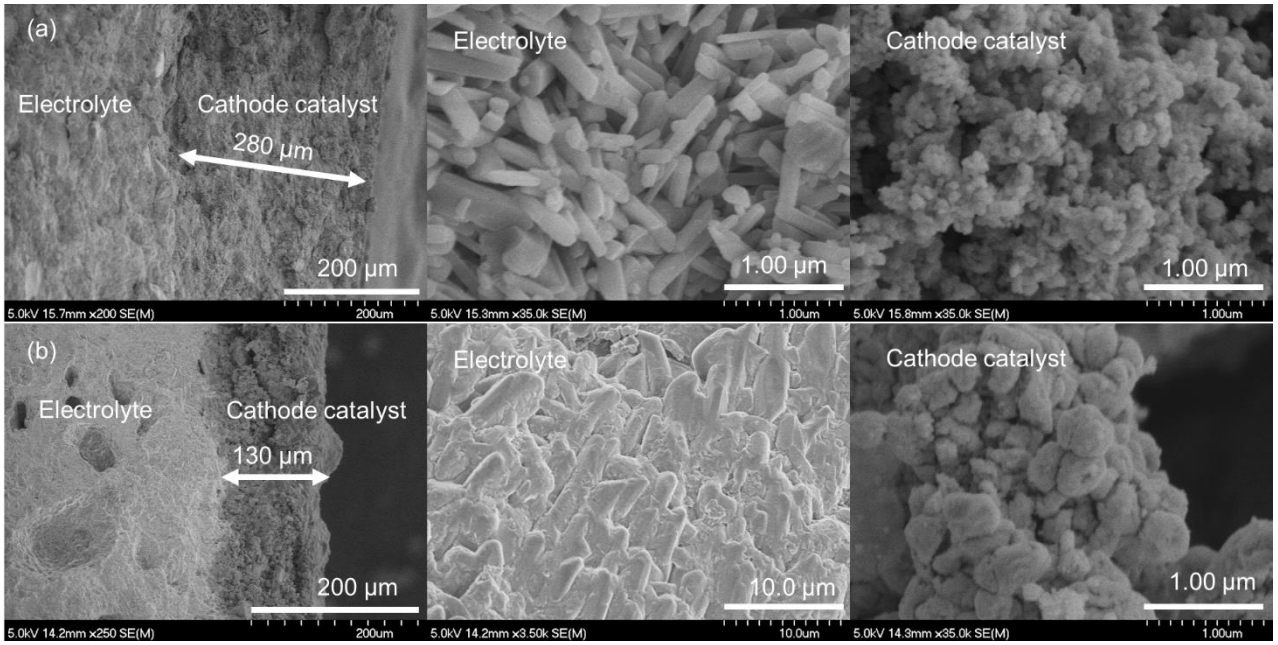
(a)
Electrolyte
Cathode catalyst
280 μm
200 μm
5.0kV 15.7mm x200 SE(M)
200um
Electrolyte
1.00 μm
5.0kV 15.3mm x35.0k SE(M)
1.00um
Cathode catalyst
1.00 μm
5.0kV 15.8mm x35.0k SE(M)
1.00um
(b)
Electrolyte
Cathode catalyst
130 μm
200 μm
5.0kV 14.2mm x250 SE(M)
200um
Electrolyte
10.0 μm
5.0kV 14.2mm x3.50k SE(M)
10.0um
Cathode catalyst
1.00 μm
5.0kV 14.3mm x35.0k SE(M)
1.00um

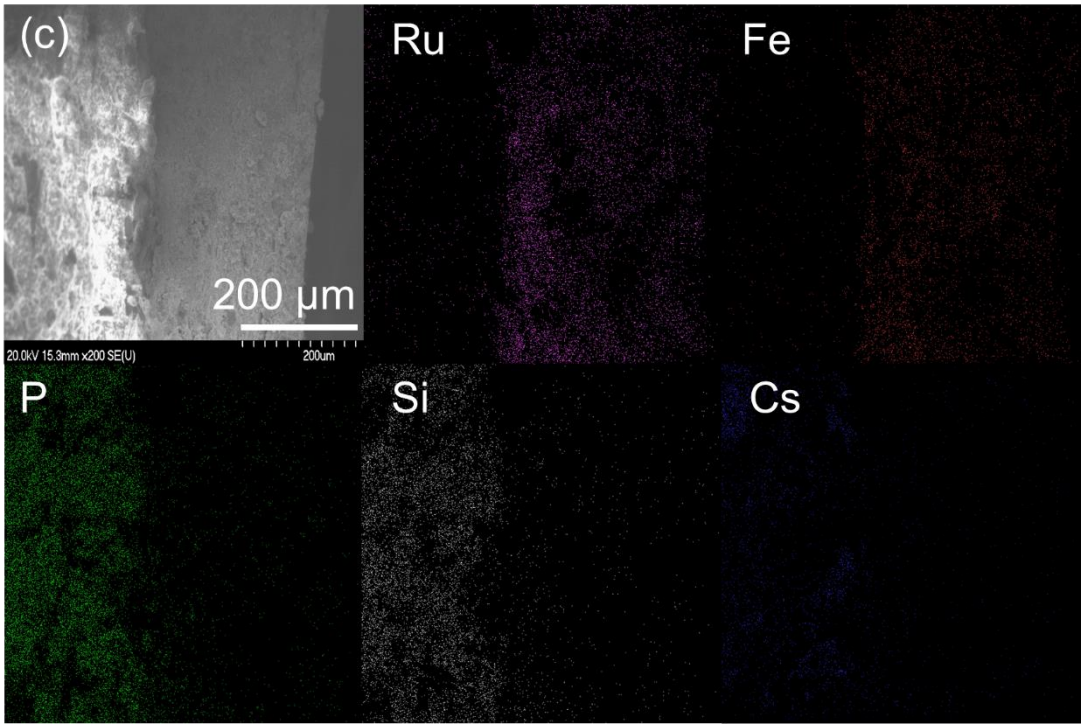
(c)
200 μm
20.0kV 15.3mm x200 SE(U)
200um
Ru
Fe
P
Si
Cs

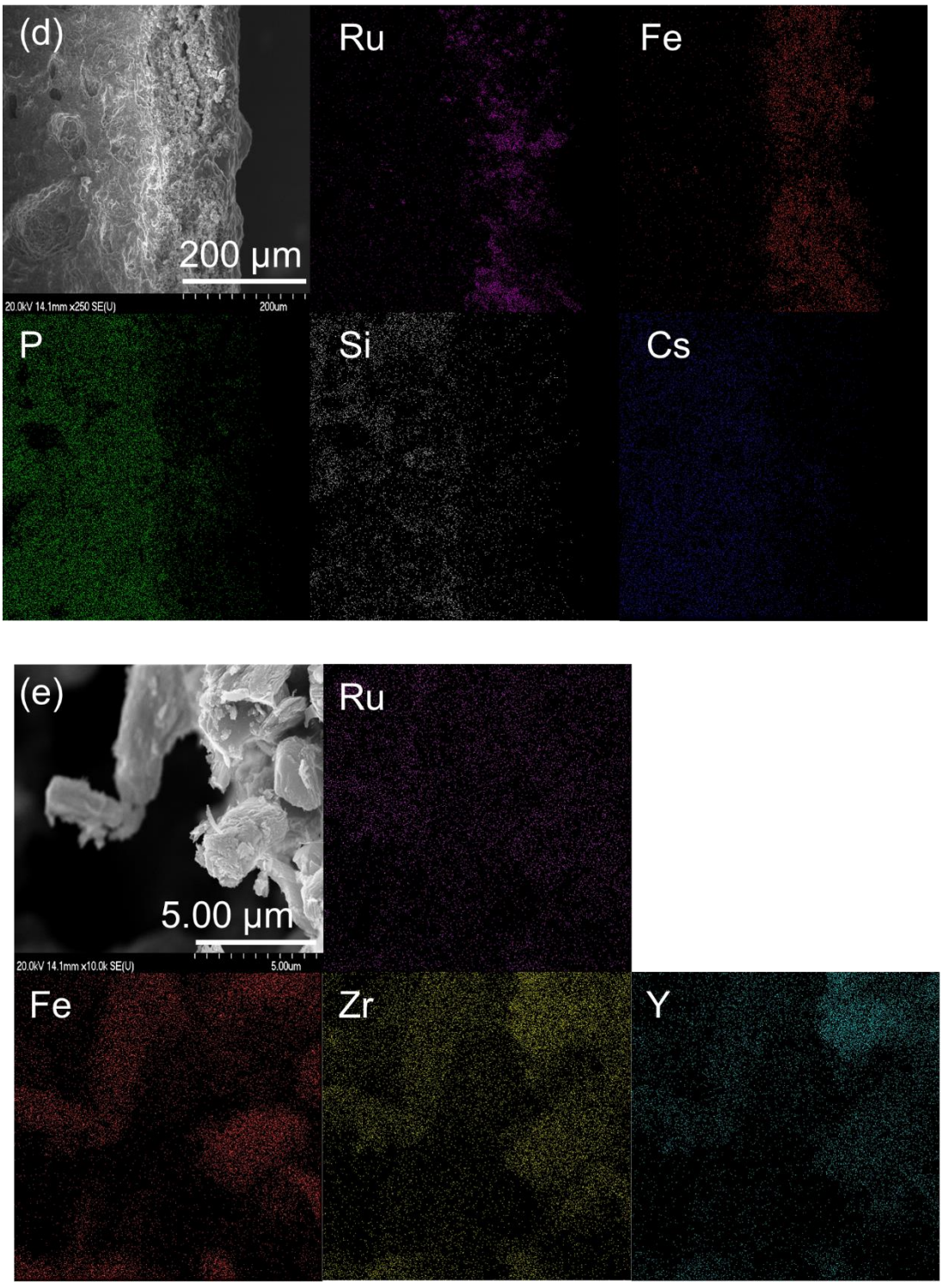

Figure 16 Cross sectional SEM-EDS images of the electrolysis cells containing a cathode catalyst which consists of a mixture of 75 mg Fe/BZY and 75 mg RuO_2: (a) as-prepared before H_2 reduction, but prior to electrocatalytic tests, (b) after

electrocatalytic tests, (c) as-prepared before H_2 reduction, but prior to electrocatalytic tests, (d) after electrocatalytic tests, and (e) magnified image after electrocatalytic tests.

3.2.2 Electrolysis results

The electrolysis cell was polarized under the flow of dry N_2 to the cathode and humidified H_2 to the anode, and the effluent gas from the electrode chambers was passed through a water trap for gas collection and analysis. Figure 19 summarizes the gas analysis results for the voltages applied (*vs.* OCV). Both NH_3 and N_2H_4 were detected in the applied voltage range from −0.1 V to −2.5 V. Because the products were only detected in the water trap of the cathode side, the cross leakage between the anode and cathode could be neglected. The detection of N_2H_4 suggests that N_2 reduction proceeded via the association mechanism. Notably, the NH_3 production rate when using only RuO_2 (Fig. 17) or Fe/BZY (Fig. 18) as the cathode catalyst was approximately 1×10^{-10} mol (s $cm^2)^{-1}$; no N_2H_4 was detected. The nitrogen reduction rate over the RuO_2 cathode reduced prior to electrolysis, at low applied voltages, was comparable to that over the Fe/BZY–RuO_2 catalyst. Despite the similar nitrogen reduction rates at low applied voltages, no N_2H_4 was detected over the RuO_2 catalyst, which supports the theory that the N–N bond dissociation in the intermediates is fast over precious metal catalysts during the associative mechanism. Another possibility is that the NRR proceeds *via* the dissociation mechanism when only the RuO_2 catalyst is used. When the applied voltage was higher, the faradaic efficiency decreased to 0.5%, which indicates that the RuO_2 electrode surface was mainly occupied by H_2 species and H_2 evolution was prominent. Over the Fe/BZY

catalyst, a similar nitrogen reduction rate was attained, but the faradaic efficiency was quite low (less than 1%). As indicated by the TPR spectrum in Figure 7, the Fe surface of the Fe/BZY electrode catalyst could be partially oxidized. Because iron oxides are rather inactive in the NRR, such partially oxidized Fe surfaces function as H_2 generation sites, leading to a small faradaic efficiency over the Fe/BZY catalyst.

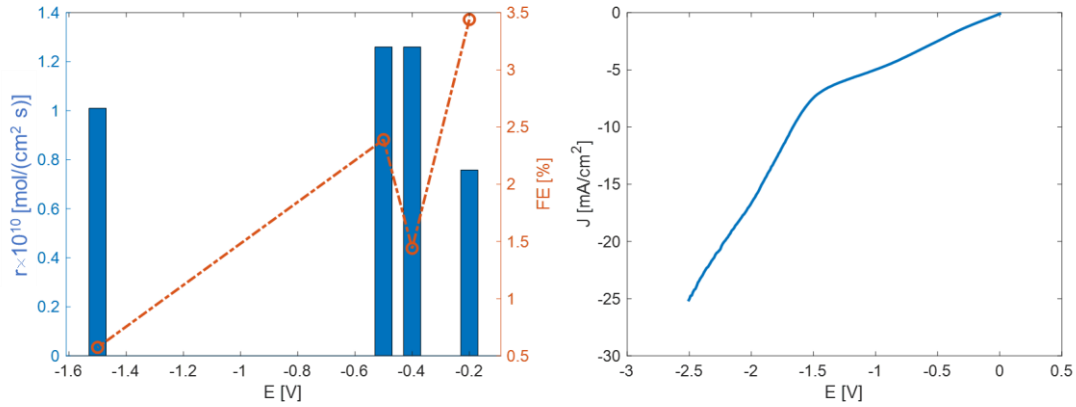

Figure 17 Electrolysis results of a cell with 0.075 g RuO_2 cathode catalyst under dry N_2 cathode atmosphere. (a) Production rate and corresponding Faradaic efficiency (FE) of NH_3, (b) the corresponding IV curve.

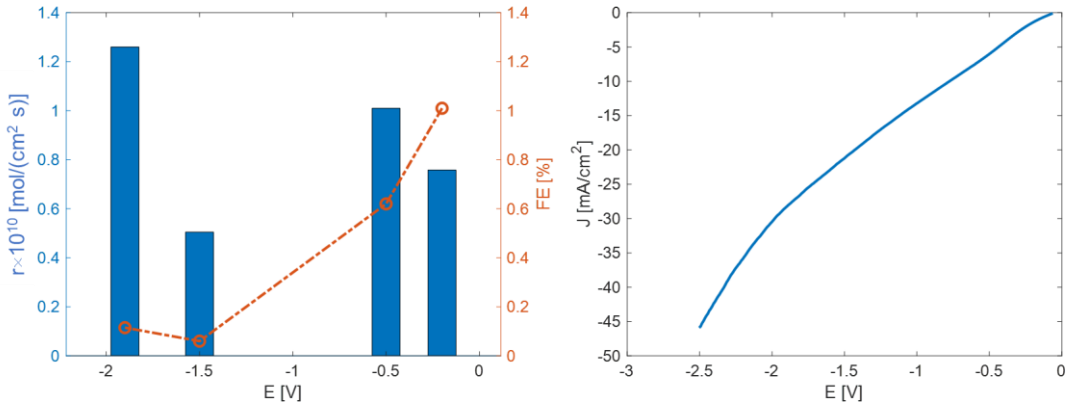

Figure 18 Electrolysis results of a cell with 0.075 g Fe/BZY cathode catalyst under dry N_2 cathode atmosphere. (a) Production rate and corresponding Faradaic efficiency (FE) of NH_3, (b) the corresponding IV curve.

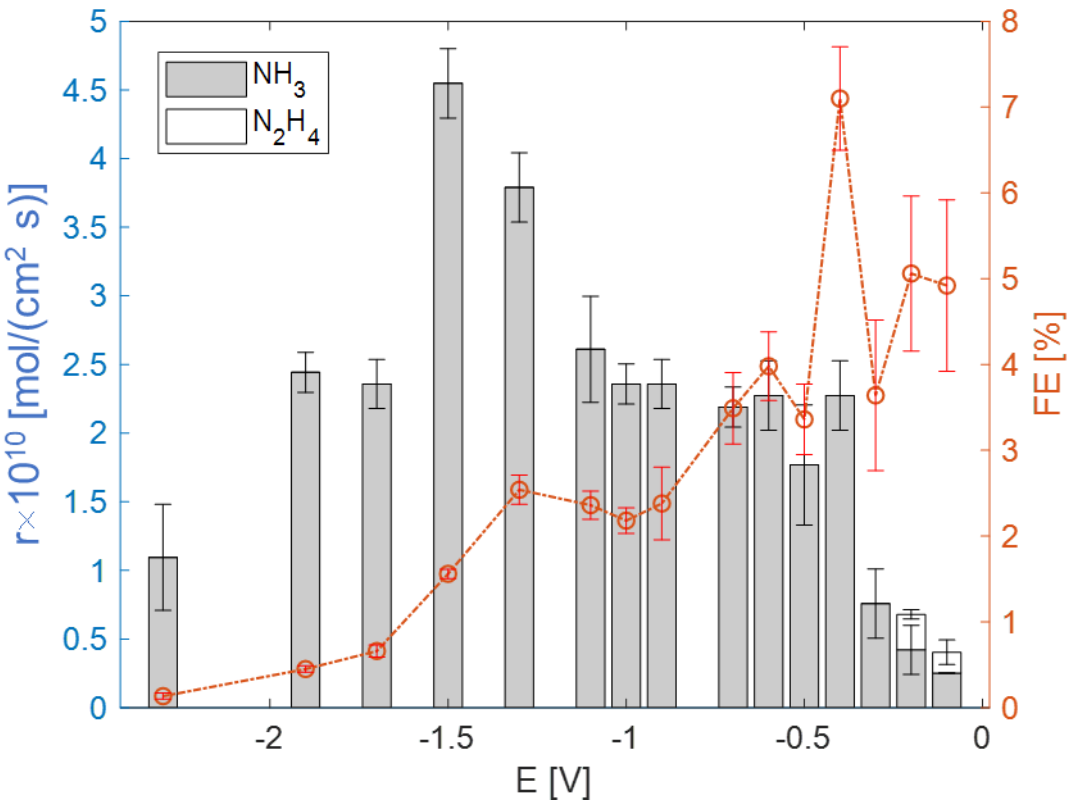

Figure 19 Production rate and corresponding faradaic efficiency (FE) of NH_3 and N_2H_4 with 0.075 g Fe/BZY cathode catalyst under 3% humidified H_2 anode atmosphere. The error bars are standard deviations.

Figure 20, 21 show the impedance spectrum measured under dry N_2 in the cathode and humidified H_2 in the anode, as represented in the Nyquist plot. Figure 22 (a) shows the equivalent circuit model used to fit the impedance spectra. In the equivalent circuit, one ohmic resistance (R_s) and two parallel circuits of a constant phase element (CPE) and resistance (R_1, R_2) are included to express the electrode reaction processes, along with an inductor (L_1). The inductance is attributed to the inductance of the cables used in the impedance measurement apparatus, and thus was invariant to measurement conditions. Figure 22 (b) summarizes R_s, R_1, and R_2 at different bias potentials. R_s is mainly attributable to the ohmic resistance of the electrolyte, whereas R_1 and R_2 are attributed to non-ohmic polarization resistance. The ohmic resistance is constant irrespective of the applied voltage, and the non-ohmic polarization resistance decreases from −0.1 V to −0.5 V. The impedance fitting results in Table 7 were calculated by Appendix. 3. The characteristic frequency of the arc for R_2 (f_2 in Table 7) is less than 10 Hz at the applied voltages, and consequently, the process characterized by the arc of R_2 in the RC parallel circuit can be assigned to a slow process, such as gas diffusion in the electrode. In addition, the characteristic frequency of the high-frequency arc is in the order of kHz. Accordingly, it is feasible that the process characterized by the high-frequency arc of R_1 is related to electrochemical reactions at the electrode surface and electrode/electrolyte interface. Notably, the smallest non-ohmic polarization resistance at −0.4 V corresponds to the highest faradaic efficiency at −0.4 V, as shown in Figure 19.

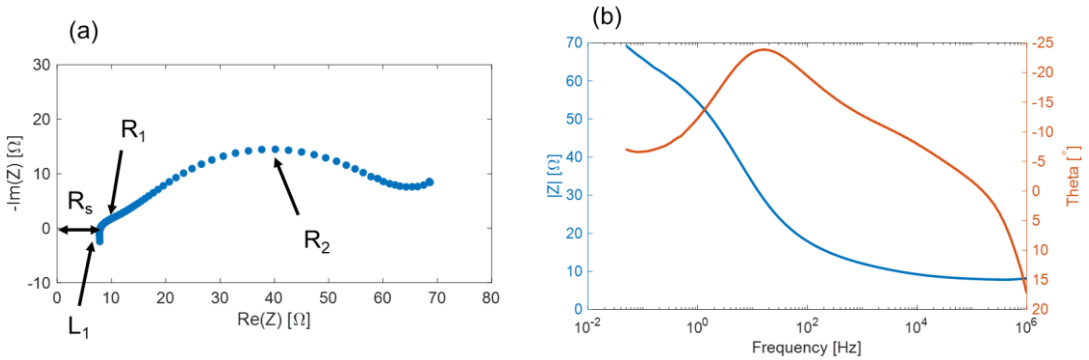

Figure 20 Impedance under dry N_2 cathode atmosphere and 3%-humidified H_2 anode atmosphere at OCV. (a) Nyquist plot. (B) Bode plot.

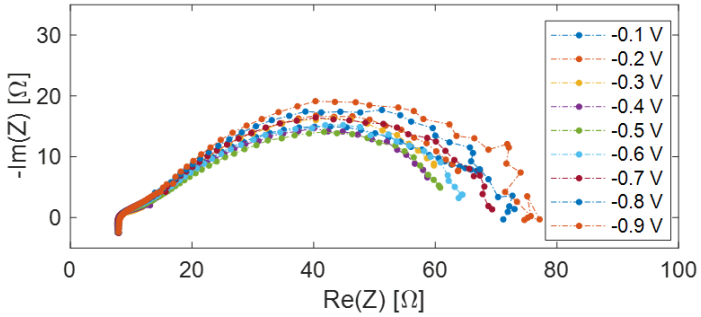

Figure 21 Nyquist plots at different bias under dry N_2 cathode atmosphere and 3%-humidified H_2 anode atmosphere.

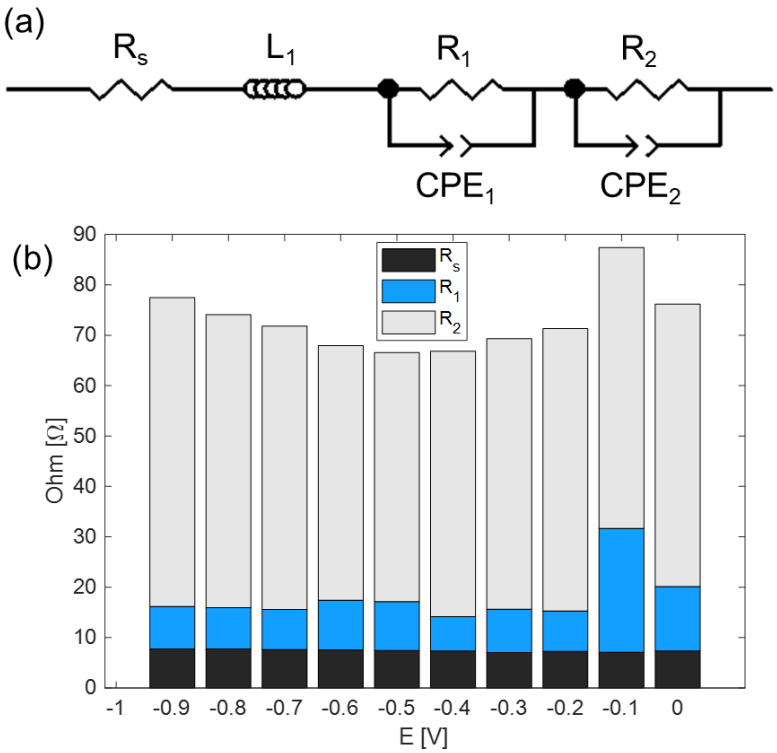

Figure 22 (a) Simplified equivalent circuit model. (b) R_s, R_1, and R_2 parameters obtained from the equivalent circuit fitting results.

Table 7 Impedance fitting result under dry N_2 on the cathode side.

applied voltage [V]	Rs [Ω]	L1 [H] $\times10^{-7}$	R1 [Ω]	CPE1-T [$F \cdot s^{CPE1-P-1}$] $\times10^{-3}$	CPE1-P $\times10^{-1}$	R2 [Ω]	CPE2-T [$F \cdot s^{CPE2-P-1}$] $\times10^{-3}$	CPE2-P $\times10^{-1}$	f1 [Hz]	f2 [Hz]
0	7.33	4.34	12.78	2.59	9.02	56.08	7.16	3.69	6.98	1.89
-0.1	7.09	4.42	24.57	4.98	7.94	55.74	1.44	3.03	2.24	0.33
-0.2	7.23	4.32	8.03	9.20	3.42	56.04	8.02	6.58	319.59	0.54
-0.3	7.03	4.44	8.57	1.41	3.02	53.73	1.07	6.57	173.53	0.37
-0.4	7.36	4.19	6.78	5.30	4.06	52.69	9.36	6.16	570.60	0.50
-0.5	7.42	4.19	9.73	6.32	3.92	49.41	8.07	6.30	195.09	0.68
-0.6	7.56	4.17	9.85	4.41	4.34	50.54	4.9	6.60	220.66	1.30
-0.7	7.62	4.14	7.96	3.11	4.68	56.25	3.37	6.62	427.71	1.96
-0.8	7.73	4.08	8.18	3.30	4.55	58.18	2.55	6.83	448.44	2.6
-0.9	7.74	4.10	8.42	3.01	4.55	61.31	1.94	6.97	511.14	3.37

3.3 Thermochemical calculation

Experimental equilibrium constants (K_{exp}) and N_2 conversion fraction were calculated under different applied voltages in the two-chamber reactor at 220 °C. The theoretical equilibrium constant (K_{eq}) at 220 °C was calculated by thermochemical properties in Appendix. 1, and is 0.239. The flow rate of N_2 at the cathode side where the NH_3 formation reaction occurred is 25 ml/min. Calculated under the assumption of an ideal gas, the flow rate is given as:

$$\frac{PV}{t} = \frac{nRT}{t}$$

Where $PV = nRT$ is from the ideal gas law, t is time, and $\frac{V}{t}$ stands for the flow rate. Based on the equation, $\frac{n}{t}$ of N_2 is 1.03×10^{-5} mol/s. Since H_2 gas is only supplied on the anode side, the flow rate of H_2 on the cathode side comes from the proton pumping, and is given as:

$$r(\mathrm{H_2}) = \frac{\mathrm{I}}{\mathrm{e} \times \mathrm{N_A}} \times \frac{1 - \mathrm{FE}}{2}$$

Where e is the elementary charge, N_A is Avogadro constant, I is the constant current, and FE is the Faraday efficiency for NH_3 synthesis. Thereby, the flow rate of H_2 on the cathode side can be given with the unit of mol/s. The experimental equilibrium constants K_{exp} is given as:

$$K_{exp} = \frac{r^2(\mathrm{NH_3})}{r(\mathrm{N_2})r^3(\mathrm{H_2})}\left(r(\mathrm{N_2}) + r(\mathrm{H_2}) + r(\mathrm{NH_3})\right)^2$$

From Figure 23, the value of K_{exp} from -0.1 V to -0.7 V is larger than the theoretical equilibrium constant K_{eq}. It may be due to the H_2 leakage from the anode side to the cathode side. The minimum amount of H_2 leakage for the K_{exp} to be the same as the K_{eq} was calculated. Assume that $r'_{min}(\mathrm{H_2})$ is the minimum amount of the leaking H_2,

$r'_{min}(\mathrm{H_2})$ can be calculated from:

$$\frac{r^2(\mathrm{NH_3})}{r(\mathrm{N_2})\left(r(\mathrm{H_2})+r'_{min}(\mathrm{H_2})\right)^3}\left(r(\mathrm{N_2})+r(\mathrm{H_2})+r'_{min}(\mathrm{H_2})+r(\mathrm{NH_3})\right)^2 = K_{eq}$$

The calculated results are shown in Figure 24. The minimum amount of the leaking H_2 is equivalent to only less than 0.02 ml/min. This means that even very small H_2 leaks can lead to large discrepancies in K_{exp} calculation.

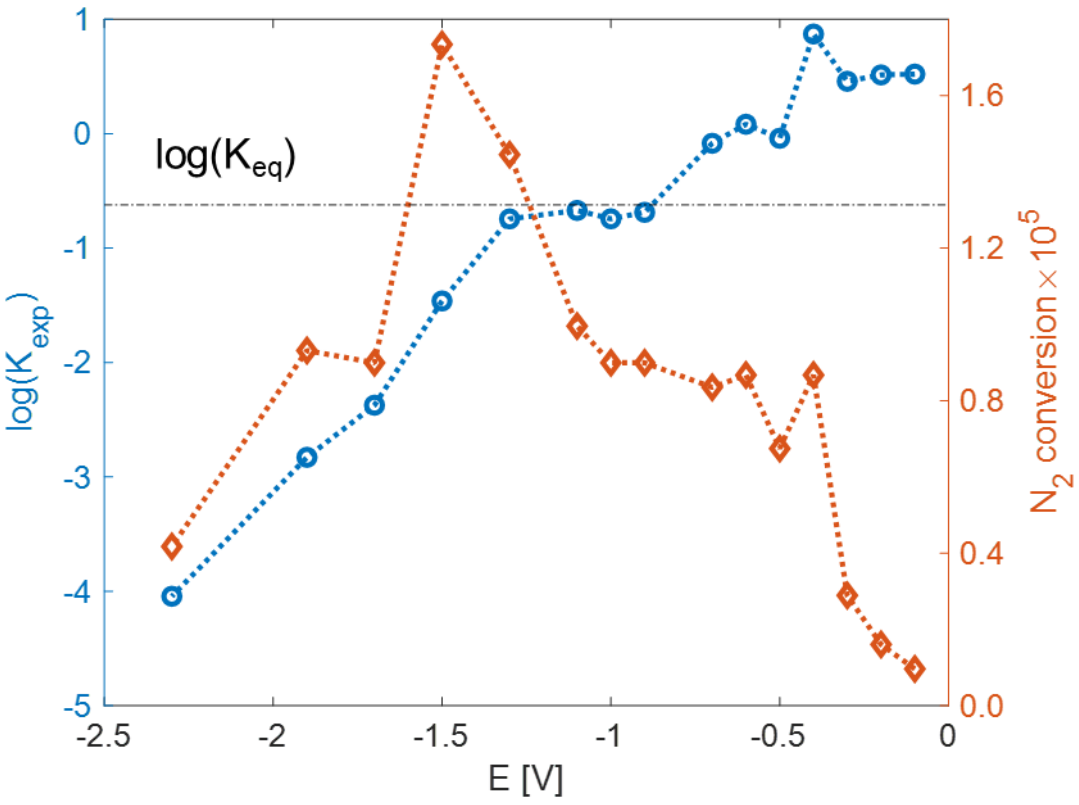

Figure 23 Experimental equilibrium constants (K_{exp}) and N_2 conversion fraction under different applied voltages at 220 °C in the two-chamber reactor.

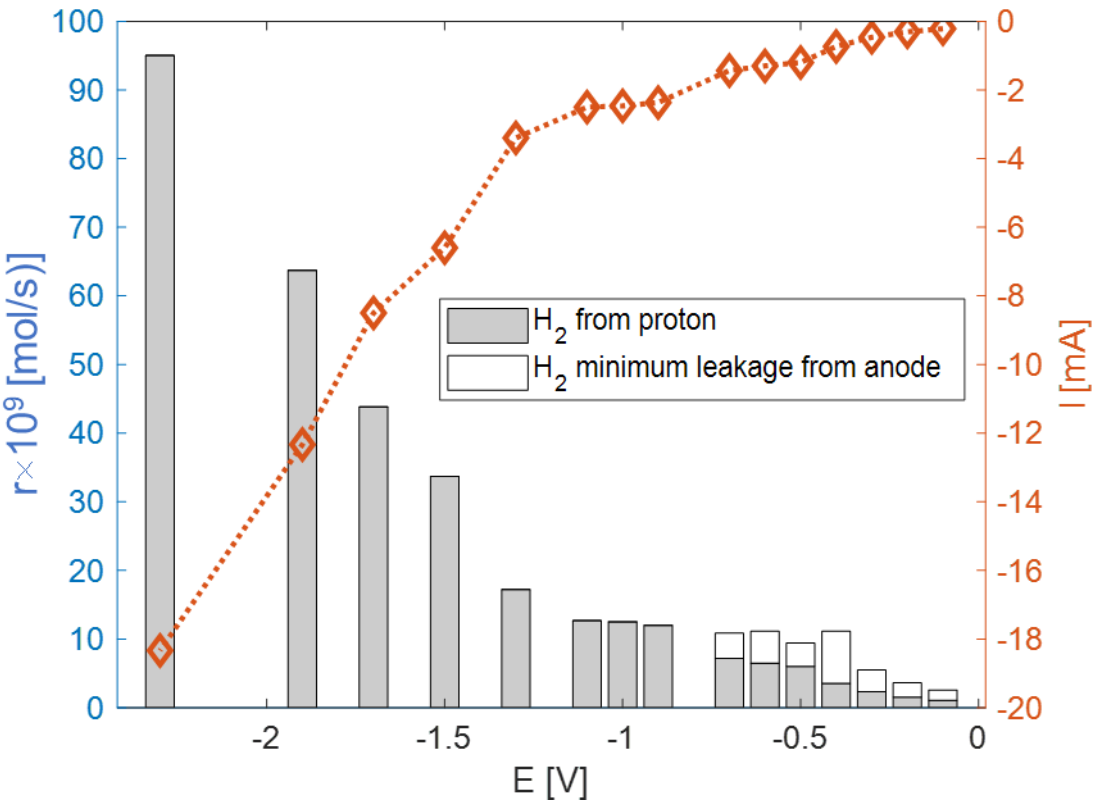

Figure 24 H_2 formed from proton (gray) and assumed minimum H_2 leakage from anode side (white). Corresponding currents (red dotted line) against right y axis.

3.4 Model of potentiostatic pulse experiment

Figure 25 illustrates the potential step program and current response during the potentiostatic pulse experiment. In this experiment, first, a constant current of i_w is loaded at an applied voltage of E_w for the period t_w. Consequently, the applied voltage is quickly converted stepwise to the OCV. Upon the quick return of the applied voltage to the OCV, the current starts to flow contrarily to i_w and gradually ceases to 0. Here, the reverse current is denoted as i_{ocv}, and the period for i_{ocv} to reach 0 is t_{ocv}. In the following experiments, E_w was applied for the period t_w = 400 s.

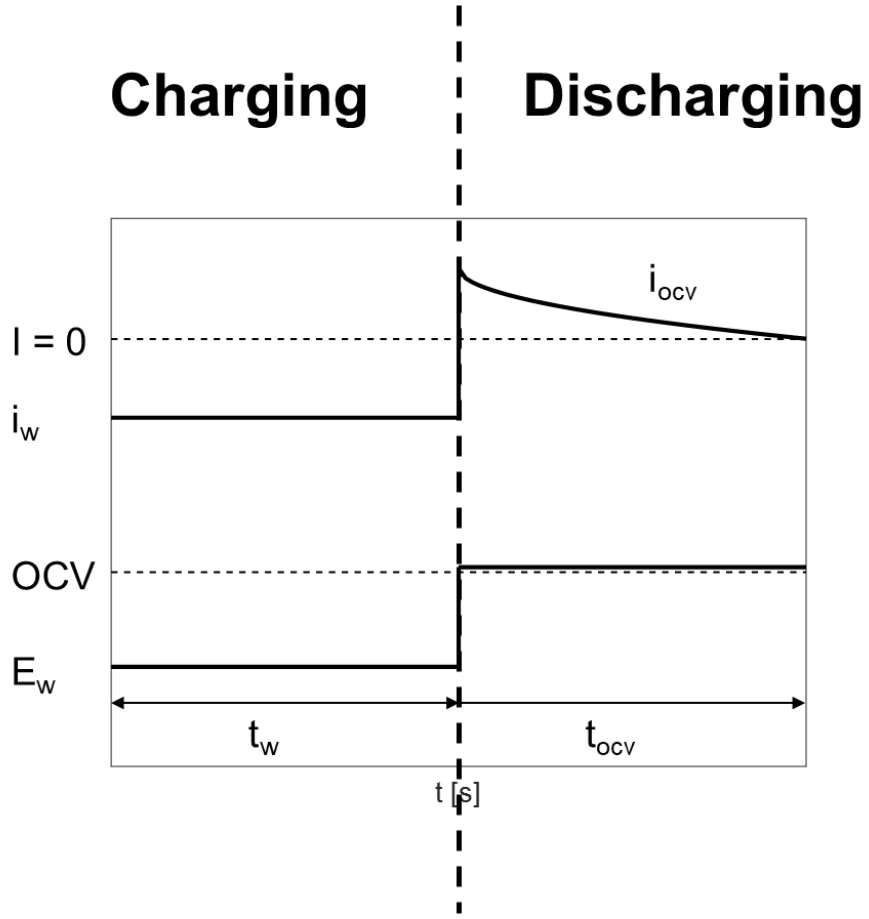

Figure 25 Illustration of potentiostatic pulse experiment.

The potentiostatic pulse experiments were conducted by feeding humidified H_2 to the anode and dry N_2 or dry Ar to the cathode. The former condition is similar to the electrolysis mode used for the synthesis of NH_3; in the latter, the same gas atmosphere is used at the cathode side as in proton pumping, general model profiles are shown in Figure 26. During the period t_w, protons are transferred from the anode to cathode and electrons are received to form a H layer (H_{ads1}) at the electrolyte/cathode interface. Subsequently, the adsorbed H_{ads1} atoms dissolve into the cathode, where they are in equilibrium with the H_{metal} concentration just below the cathode/electrolyte interface (H_{metal} denotes H atoms in the bulk metal of the cathode catalyst). This is followed by the diffusion and trapping of the H_{metal} atoms in the bulk metal. The H_{metal} atoms then cross the cathode to the cathode/gas interface and reach an equilibrium value (H_{ads2}) on the cathode surface. When dry Ar feed is used in the cathode, only H_{ads2} is assumed to reside at the surface of the electrode catalyst during the period t_w, while under a dry N_2 feed, N_2-containing species (N_2H_{ads2} and/or NH_{ads2}) could adsorb on the electrode catalyst surface in addition to H_{ads2}. In this model, i_{ocv} is derived from three types of reactions illustrated in Figure 27. The first reaction involves the decomposition and ionisation of adsorbed species on the surface of the cathode catalyst. When using a dry Ar feed, only the $H_{ads2} \rightarrow H^+ + e^-$ reaction needs to be considered as the reverse current source during t_{ocv}. When using a dry N_2 feed, the decomposition reactions of the intermediates, such as N_2H_{ads2} and/or NH_{ads2}, should also be considered. The second reaction stems from the remaining H_{metal} in the bulk metal, while the third reaction is due to the electrical double layer.

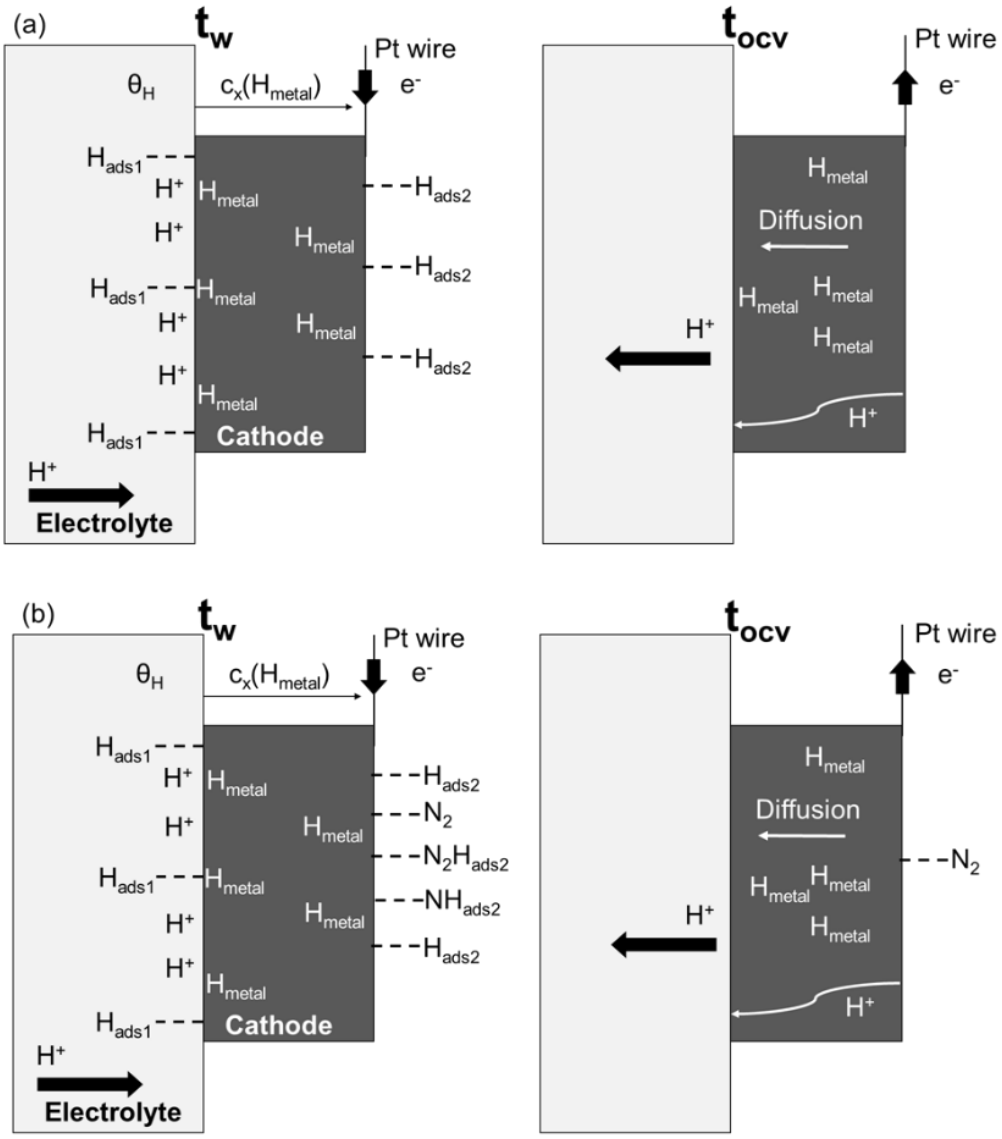

Figure 26 General model profiles of cathode side (a) under Ar (b) under N_2, where t_w and t_{ocv} correspond to charging and discharging process.

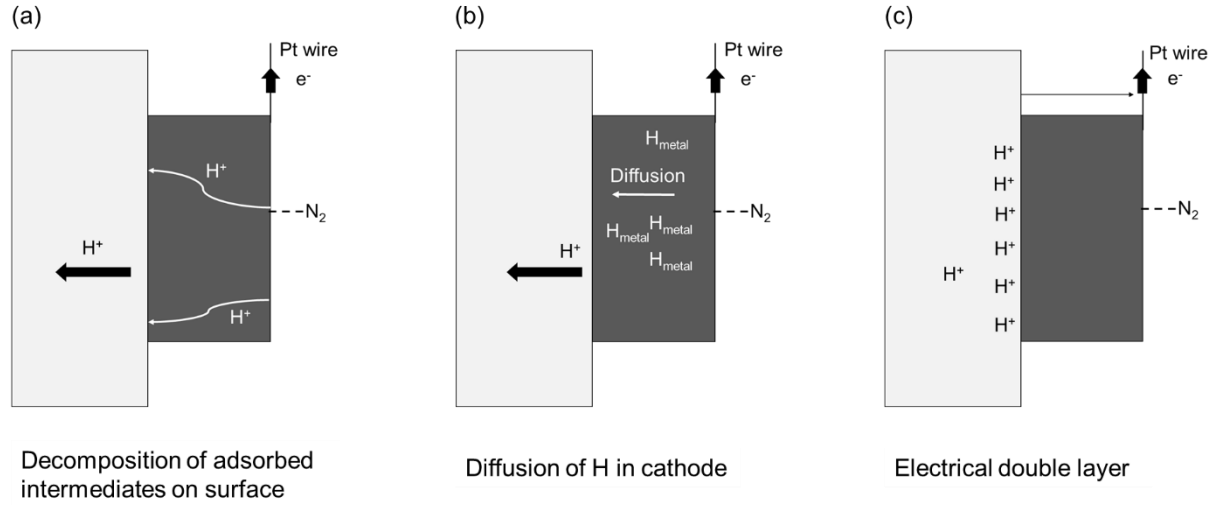

Figure 27 Illustrations of three kinds of reactions correspond to i_{ocv}.

The i_{ocv} from the remaining H_{metal} in the bulk metal will be discussed first, based on the following analyses. According to Pound *et al.*[75 76] , when the proton transfer across the cathode/electrolyte interface is very fast, the i_{ocv} from $H_{metal} \rightarrow H^+ + e^-$ is only controlled by the diffusion of H_{metal}. They adopted the following boundary conditions at the electrode surface as

$$\begin{cases} c(0,t) = 1 \\ \dfrac{\partial c}{\partial x}(x,0) = 0 \\ c \rightarrow 0 \; as \; x \rightarrow \infty \end{cases}$$

where x is the distance from the electrolyte/cathode interface, t is the diffusion time and c stands for the consentration,[26] because H_{metal} cannot diffuse to the electrode/gas boundary within a charge time of less than 20 seconds, which they applied to the analysis of their experimental results エラー! ブックマークが定義されていません。. In this work, we adopted a long enough charging time of 400 seconds, and accordingly H_{metal} atoms are considered to diffuse to the cathode/gas interface to form the adsorbed hydrogen on the cathode surface, and are released as gaseous H_2 in a steady state. Therefore, the boundary

conditions are different from those by Pound *et al*., and with appropriate boundary conditions in our study it is feasible to take into account the contributions of the decomposition of the adsorbed species at the cathode surface and the electrical double layer at the cathode/electrolyte interface to the $i_{ocv.}$

At the charging step, it can be assumed that the H atom traps are unsaturated, and therefore the trapping rate constant, *k,* remains constant. Fick's second law of diffusion can be modified with *kc*, where *k* is the trapping rate constant and *c*(*x*, *t*) is the concentration of H_{metal} at a distance *x* from the electrolyte/cathode interface and at a time *t*, which starts from $t_w = 0$. *D* is the diffusion coefficient of H_{metal} in the cathode.

$$D\frac{d^2c}{dx^2} = kc \quad \#\text{Eq. 1}$$

$$c = Ae^{\sqrt{k/D}x} + Be^{-\sqrt{k/D}x} \quad \#\text{Eq. 2}$$

θ in Eq. 3 represents the adsorbed H on the electrolyte side at the interface of the cathode and electrolyte. The boundary conditions thus become:

$$\begin{cases} D\frac{dc}{dx}(0) = k_{ex}c(0) - k_{in}\theta \\ D\frac{dc}{dx}(X) = -k^{ex}c(X) \end{cases} \quad \#\text{Eq. 3}$$

where k_{ex} and k_{in} are the rate constants of H moving out of the cathode and the ingress of H into the cathode at the electrolyte/cathode interface, respectively. The symbol *X* represents the thickness of the cathode catalyst, and has a value of 200 μm, as shown in Fig. 3(a) and (b). By substituting Eq. 2 into Eq. 3, the following is obtained:

$$\begin{cases} \sqrt{kD}(A - B) = k_{ex}(A + B) - k_{in}\theta \\ \sqrt{kD}\left(Ae^{\sqrt{k/D}X} - Be^{-\sqrt{k/D}X}\right) = -k^{ex}\left(Ae^{\sqrt{k/D}X} + Be^{-\sqrt{k/D}X}\right) \end{cases} \quad \#\text{Eq. 4}$$

Thus, *A* and *B* can be obtained by Eq. 5 and 6.

$$\mathrm{Be}^{-\sqrt{\mathrm{k/D}}\mathrm{X}} = \frac{\sqrt{\mathrm{kD}}+\mathrm{k}^{\mathrm{ex}}}{\sqrt{\mathrm{kD}}-\mathrm{k}^{\mathrm{ex}}}\mathrm{Ae}^{\sqrt{\mathrm{k/D}}\mathrm{X}}, \#\text{Eq. 5}$$

$$k_{\mathrm{in}}\theta = \left(\left(k_{\mathrm{ex}} - \sqrt{kD}\right) + \left(k_{\mathrm{ex}} + \sqrt{kD}\right)\frac{\sqrt{kD}+k^{\mathrm{ex}}}{\sqrt{kD}-k^{\mathrm{ex}}}e^{2\sqrt{k/D}X}\right)A \ \#\text{Eq. 6}$$

In the discharging step, taking into account the effect of the H_{metal} atoms trapped in the bulk metal, Fick's second law of diffusion can be modified with *kc*; time *t* starts from t_{ocv} = 0.

$$\frac{\partial c}{\partial t} - D\frac{\partial^2 c}{\partial x^2} = -kc \ \#\text{Eq. 7}$$

The boundary conditions thus become:

$$\begin{cases} c(0,t) = 0 \\ \frac{\partial c}{\partial x}(X,t) = 0 \end{cases} \#\text{Eq. 8}$$

The following assumption is then made:

$$\begin{cases} c(x,t) = f(x)g(t) \\ D\frac{d^2 f}{dx^2} = k_f f \end{cases} \#\text{Eq. 9}$$

where, if $k_f > 0$, then $f = ae^{\sqrt{k_f/D}x} + be^{-\sqrt{k_f/D}x}$. By substituting the boundary conditions, $f = 0$ can be obtained. If there is no H trapping, which implies $k = 0$, then $f = 0$. If $k_f < 0$, then $f = a_{k_f}\cos\sqrt{-k_f/D}x + b_{k_f}\sin\sqrt{-k_f/D}x$. By substituting the boundary conditions, $a_{k_f} = 0$ and $b_{k_f} \neq 0 \Rightarrow \sqrt{-k_f/D}X = \left(n+\frac{1}{2}\right)\pi$, where *n* is an integer. Because $k_g = k_f - k < 0$, $\frac{dg}{dt} = k_g g \Rightarrow g = c_{k_g}e^{k_g t}$. *F* is Faraday's constant. Thus, the following is obtained:

$$c(x,t) = \sum_n A_n \sin\left(n+\frac{1}{2}\right)\pi\frac{x}{X}e^{-\left(\left((n+1/2)\pi/X\right)^2 D+k\right)t} \ \#\text{Eq. 10}$$

$$i = FD\frac{dc}{dx}(0,t) = \pi FD\sum_n\left(n+\frac{1}{2}\right)\frac{A_n}{X}e^{-\left(\left((n+1/2)\pi/X\right)^2 D+k\right)t} \ \#\text{Eq. 11}$$

By substituting Eq. 2 into Eq. 10, the initial discharging condition is obtained as:

$$Ae^{\sqrt{k/D}x} + Be^{-\sqrt{k/D}x} = \sum_n A_n \sin\left(n+\frac{1}{2}\right)\pi\frac{x}{X} \ \#\text{Eq. 12}$$

Taking integrals on both sides of $Ae^{\sqrt{k/D}x} + Be^{-\sqrt{k/D}x} = \sum_n A_n \sin\left(n+\frac{1}{2}\right)\pi\frac{x}{X}$ #Eq. 12, Eq.13 obtained:

$$\int_0^X \sin\left(n+\frac{1}{2}\right)\pi\frac{x}{X}\left(Ae^{\sqrt{k/D}x} + Be^{-\sqrt{k/D}x}\right)dx = A_n\int_0^X \sin^2\left(n+\frac{1}{2}\right)\pi\frac{x}{X}dx \quad \#\text{Eq. 13}$$

Assuming $p = \sqrt{k/D}$ and $q = \left(n+{}^1/_2\right){}^\pi/_X$, Eq. 14 and Eq. 15 obtained,

$$\begin{cases} A_n\int_0^X \sin^2\left(n+\frac{1}{2}\right)\pi\frac{x}{X}dx = {}^{A_nX}/_2 \\ \int_0^X \sin\left(n+\frac{1}{2}\right)\pi\frac{x}{X}(Ae^{px}+Be^{-px})dx = \frac{(-1)^n p\left(Ae^{pX}-Be^{-pX}\right)+q(A+B)}{p^2+q^2} \end{cases} \quad \#\text{Eq. 14}$$

$$A_n = \frac{2}{X}\frac{(-1)^n p\left(Ae^{pX}-Be^{-pX}\right)+q(A+B)}{p^2+q^2} \quad \#\text{Eq. 15}$$

Thus, i_{ocv} derived from H_{metal} is given as:

$$i(t) = \pi FD\sum_n\left(n+\frac{1}{2}\right)\frac{A_n}{X}e^{-\left(\left((n+1/2)\pi/X\right)^2 D+k\right)t}$$

$$= \frac{\pi FD}{X^2}\sum_n(2n+1)\frac{(-1)^n\sqrt{k/D}\left(Ae^{\sqrt{k/D}X}-Be^{-\sqrt{k/D}X}\right)+\left(n+{}^1/_2\right)^\pi/_X(A+B)}{\left({}^k/_D+\left(\left(n+{}^1/_2\right)^\pi/_X\right)^2\right)e^{\left(\left((n+1/2)\pi/X\right)^2 D+k\right)t}} \quad \#\text{Eq. 16}$$

For the adsorbed species on the surface with dry Ar feed, only the $H_{ads2}\rightarrow H^+ + e^-$ reaction occurs on the surface of the cathode. Here, k_1 represents the reaction rate constant of $H_{ads2}\rightarrow H^+ + e^-$, and β_H is the amount of adsorbed H atoms.

$$\begin{cases} \frac{d\theta_H}{dt} = -k_1\beta_H \\ \beta_H = A_H e^{-k_1 t} \end{cases} \quad \#\text{Eq. 17}$$

When using a dry N_2 feed, if the NRR is mainly in accordance with the associative mechanism, $N_2H_{ads2}\rightarrow N_{2ads2}+H_{ads2}$ and $H_{ads2}\rightarrow H^+ + e^-$ are the reactions that occur on the surface of the cathode. Otherwise, $NH_{ads2}\rightarrow N_{ads2}+H_{ads2}$ and $H_{ads2}\rightarrow H^+ + e^-$ reactions occur. Here, k_2 represents the reaction rate constant of NH or N_2H decomposition, and $\beta_{NH\ or\ N2H}$ is the amount of NH or N_2H adsorbed.

$$\begin{cases} \frac{d\beta_H}{dt} = -k_1\beta_H + k_2\beta_{N_2H\ or\ NH} \\ \frac{d\beta_{N_2H\ or\ NH}}{dt} = -k_2\beta_{N_2H\ or\ NH} \\ \beta_H = B_H e^{-k_1 t} + C_2 e^{-k_2 t} \end{cases}$$ #Eq. 18

$k_1\beta_{\mathrm{H}} = k_1 B_H e^{-k_1 t} + \frac{k_1 k_2}{k_1 + k_2} B_H e^{-k_2 t}$ #Eq. 19

The third i_{ocv} reaction, which is due to discharge of the capacitor by the electrical double layer, is given as:

$$i_3 = A_C e^{-\frac{1}{RC}t}$$ #Eq. 20

Therefore, the total i_{ocv} in a dry Ar feed and dry N_2 feed is given by:

$$i_{OCV} = \frac{\pi FD}{X^2}\sum_n (2n+1)\frac{(-1)^n\sqrt{k/D}\left(Ae^{\sqrt{k/D}X} - Be^{-\sqrt{k/D}X}\right) + \left(n+1/2\right)\pi/X(A+B)}{\left(k/D + \left(\left(n+1/2\right)\pi/X\right)^2\right)e^{\left(\left(n+1/2\right)\pi/X\right)^2 D+k)t}} + FA_H e^{-k_1 t} +$$

$$A_C e^{-\frac{1}{RC}t}$$ #Eq. 21

$$i_{OCV} = \frac{\pi FD}{X^2}\sum_n (2n+1)\frac{(-1)^n\sqrt{k/D}\left(Ae^{\sqrt{k/D}X} - Be^{-\sqrt{k/D}X}\right) + \left(n+1/2\right)\pi/X(A+B)}{\left(k/D + \left(\left(n+1/2\right)\pi/X\right)^2\right)e^{\left(\left(n+1/2\right)\pi/X\right)^2 D+k)t}} +$$

$$F\left(k_1 B_H e^{-k_1 t} + \frac{k_1 k_2}{k_1 + k_2} B_H e^{-k_2 t}\right) + A_C e^{-\frac{1}{RC}t}$$ #Eq. 22

The raw i_{ocv} to t_{ocv} data, collected at -0.2 V, -0.5 V, -1.5 V, and -1.9 V, were fitted using $i_{OCV} = \frac{\pi FD}{X^2}\ n\square\square(2n+1)\ (-1)^n\ \sqrt{k/D}\left(Ae^{\ \sqrt{k/D}X} - Be^{-\ \sqrt{k/D}X}\right) + \left(n + 1/2\right)\pi/X\ (A+B)\square\left(k/D + \left(\left(n+1/2\right)\pi/X\right)^2\right)\ e\square\ \left(\left(n+1/2\right)\pi/X\right)2D{+}kt{+}FAHe{-}k\square1\square t\square + A_C e^{-\frac{1}{RC}t}$ # Eq. 21 with the D, k, k_1, A_H, $(A{+}B)$, and $Ae^{\sqrt{k/D}X} - Be^{-\sqrt{k/D}X}$ parameters. Based on my assumptions, the D and k parameters do not depend on the applied voltage E; however, k_1, A_H, A, and B does.

According to the Eq. 21 and Eq. 22 i_{ocv} is the sum of several exponential formulas, which are derive from diffusion of H atom in the metal bulk, decomposition of adsorbed species

on the catalyst surface and the discharge of capacitor by electrical double layer. Since the diffusion of H atom part is the infinite sum of exponential formulas, in order to solve the numerical solutions, the diffusion of H atom part is approximated by the sum of n = 0 and n = 1. Because the diffusion of H atom part and the capacitor discharge part decay very quickly, i_{ocv} mainly consists of the decomposition part when t is large. In this work, the raw data were fitted with $FA_{\mathrm{H}}e^{-k_1 t}$ or $F\left(k_1 B_H e^{-k_1 t} + \frac{k_1 k_2}{k_1+k_2} B_H e^{-k_2 t}\right)$ from 50 s to 100 s in Figure 30, 31. The sum of diffusion part and the capacitor discharge part was fitted with the residual.

Values for all the parameters were determined for each *E*, and it was verified that the values of *D* and *k* do not depend on *E*, where *D* is 1.0×10^{-9} m^2/s and *k* is 4.5×10^{-2} s^{-1}. With the *D*, *k*, A_H, and k_1 values obtained for the condition where a dry Ar gas atmosphere was used at the cathode side, the relationship between i_{ocv} and t_{ocv} under the same gas atmosphere under electrolysis conditions is provided by $i_{OCV} = \frac{\pi FD}{X^2}$ n□□$(2n+1)$ $(-1)^n \sqrt{k/D}\left(Ae^{\sqrt{k/D}X} - Be^{-\sqrt{k/D}X}\right) + \left(n + {}^1/_2\right)\pi/_X (A+B)$□$\left({}^k/_D + \left(\left(n + {}^1/_2\right)\pi/_X\right)^2\right)$ e□ $\left(\left(n + {}^1/_2\right)\pi/X\right)$ *2D+kt+Fk1BHe–k* □1□t□ $+ \frac{k_1 k_2}{k_1+k_2} B_H e^{-k_2 t}$□ + $A_C e^{-\frac{1}{RC}t}$ #Eq. 22. The raw i_{ocv} to t_{ocv} data, collected at -0.2 V, -0.5 V, -1.5 V, and -1.9 V, were fitted with the k_2, *(A+B)*, $Ae^{\sqrt{k/D}X} - Be^{-\sqrt{k/D}X}$, C_1, and C_2 parameters. Figure 28 shows the fitting results for the current response at the cathode side under a dry Ar gas atmosphere at the voltages applied (-0.2 V, -0.5 V, -1.5 V, and -1.9 V). In this figure, "surface" denotes the current response by the decomposition of intermediates on the surface of the catalyst, "diffusion" denotes the response by the diffusion of H in the catalyst, "capacitor" denotes the response by the electrical double layer, and "fitted"

represents the summation of these three contributions. Figure 29 summarizes the fitting results at the cathode side under a dry N_2 gas atmosphere at -0.2 V, -0.5 V, -1.5 V, and -1.9 V. The fitting results presented in Figure 28, 29 demonstrate that the developed model fits well with the experimentally measured current responses, and that the current responses assigned to the decomposition of the intermediates, diffusion of H atoms in the catalyst, and the electrical double layer are all positive and thus rational.

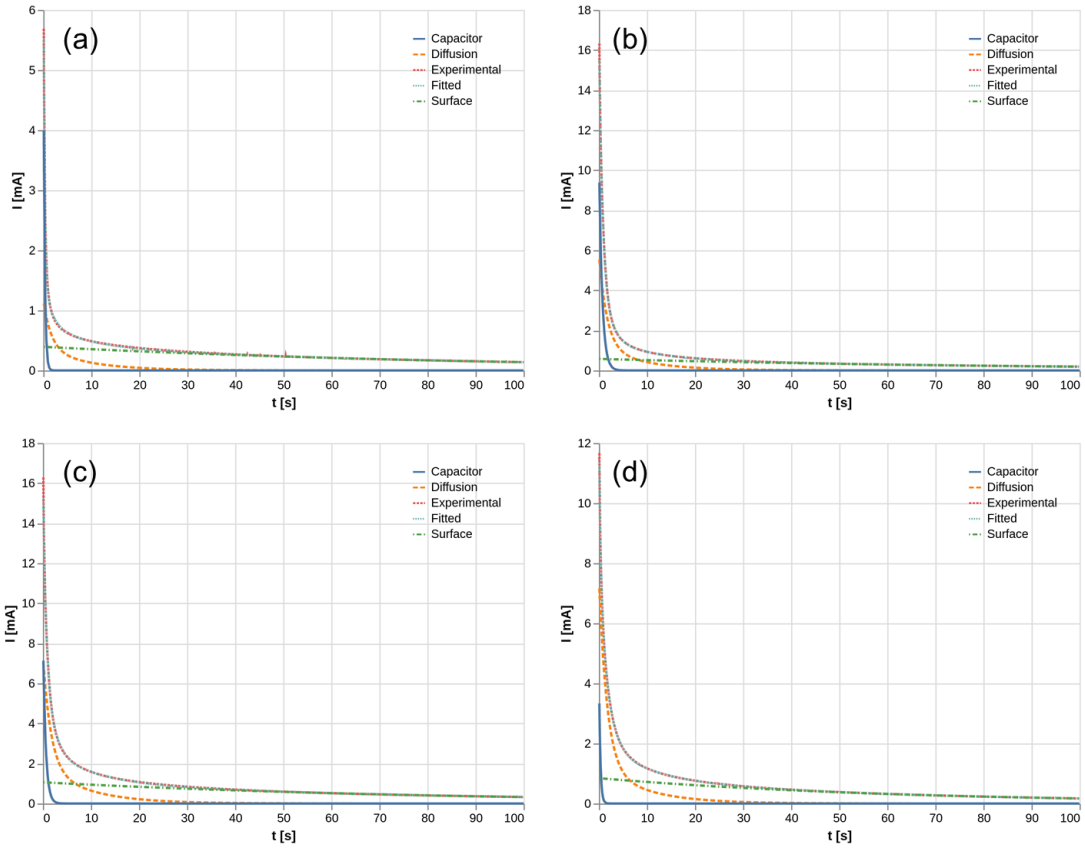

Figure 28 Fitting results under dry Ar gas atmosphere at cathode side. (a) -0.2 V, (b) -0.5 V, (c) -1.5 V, and (d) -1.9 V. Surface (green dash-dot line): decomposition of intermediates on the surface of catalyst. Diffusion (red dashed line): diffusion of H in catalyst. Capacitor (blue solid line): electrical double layer. Experimental (red dotted line): raw data. Fitted (green dotted line): total fitting.

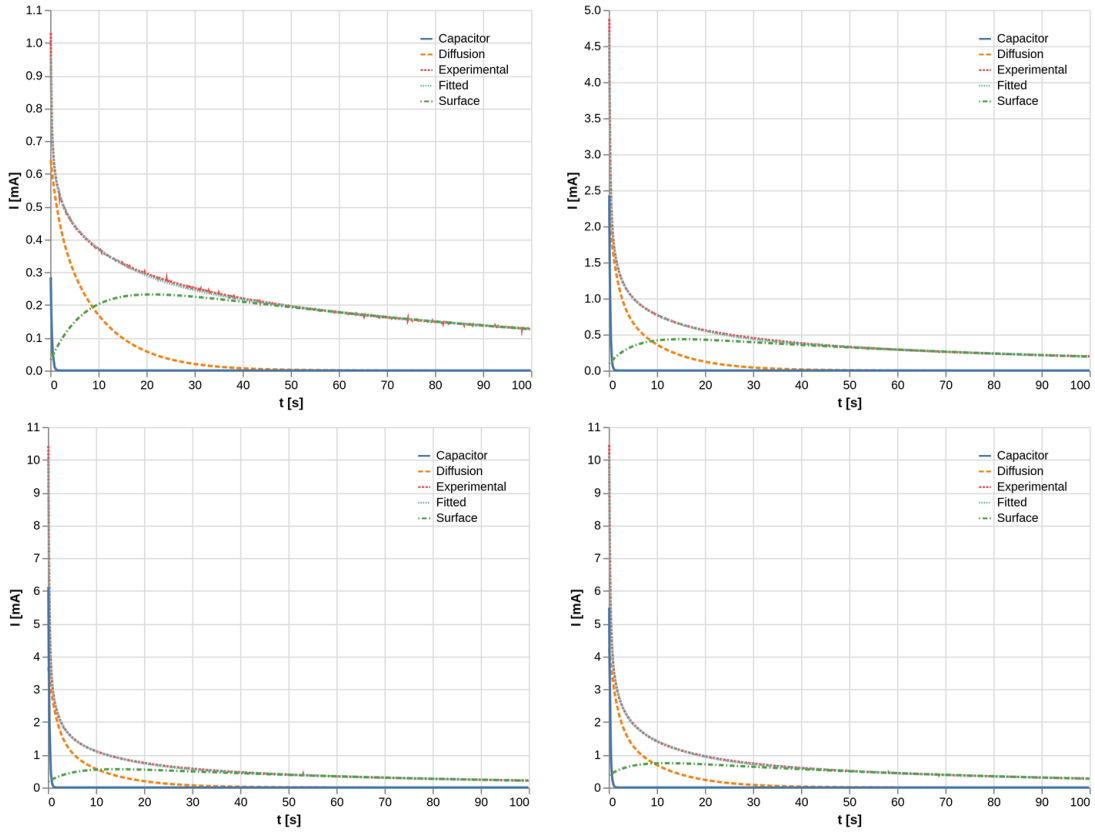

Figure 29 Fitting results under dry N_2 gas atmosphere at cathode side. (a) -0.2 V, (b) -0.5 V, (c) -1.5 V, and (d) -1.9 V. Surface (green dash-dot line): decomposition of intermediates on the surface of catalyst. Diffusion (red dashed line): diffusion of H in catalyst. Capacitor (blue solid line): electrical double layer. Experimental (red dotted line): raw data. Fitted (green dotted line): total fitting.

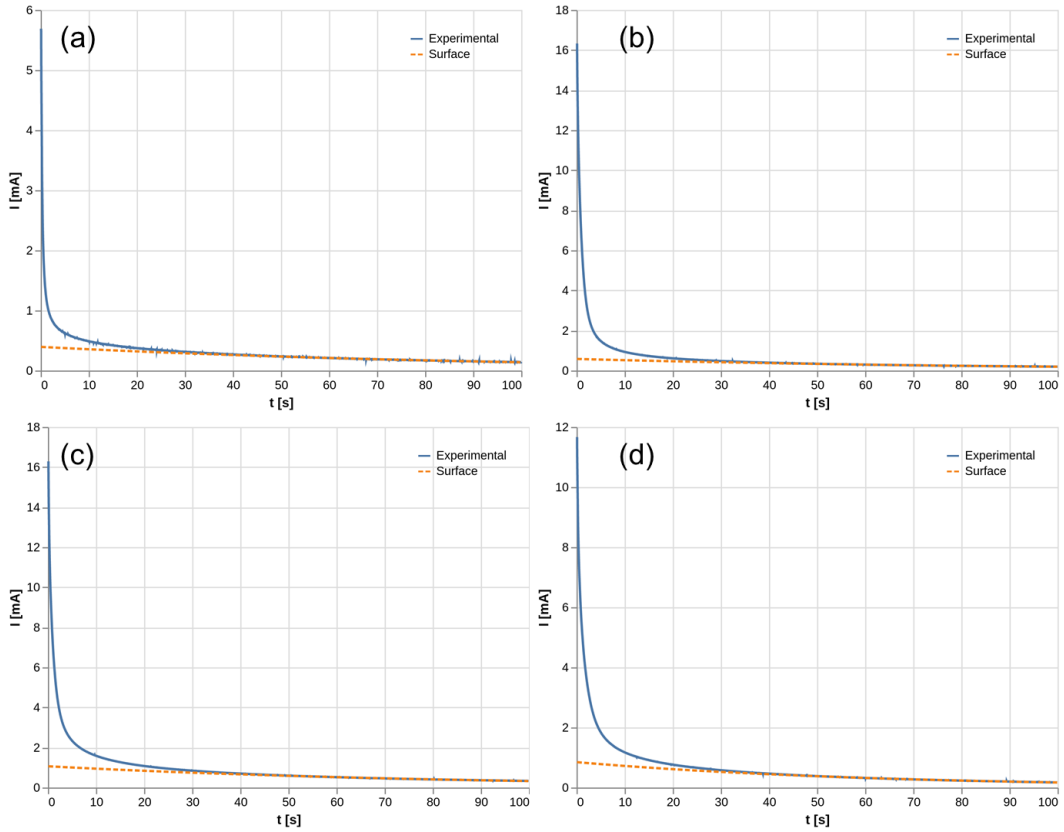

Figure 30 Fitting results of the intermediates decomposition part under dry Ar gas atmosphere at cathode side. (a) -0.2 V (b) -0.5 V (c) -1.5 V (d) -1.9 V.

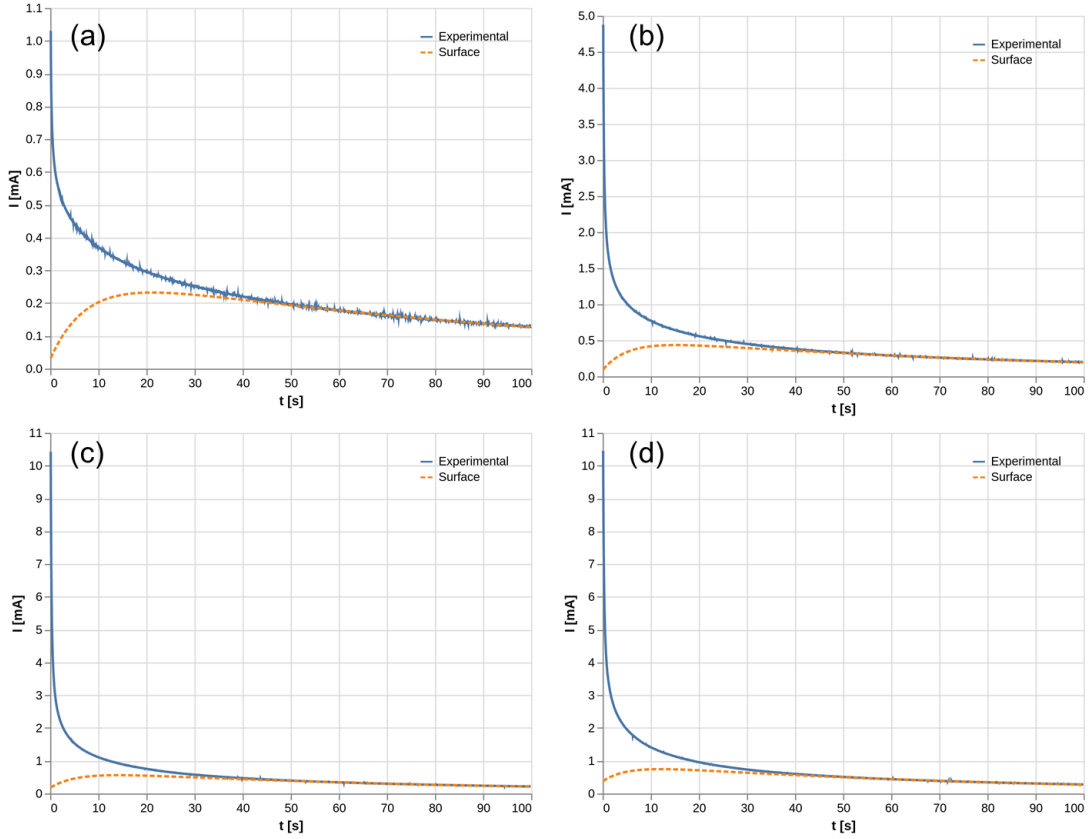

Figure 31 Fitting results of the intermediates decomposition part under dry N_2 gas atmosphere at cathode side. (a) -0.2 V (b) -0.5 V (c) -1.5 V (d) -1.9 V.

Table 8, 9 summarize the parameters obtained from Eq. 21 and 22. The common parameters, k and D, are equal to 0.045 s^{-1} and 1.0×10^{-9} m^2/s, respectively. The value of k_1 for all the applied voltages is approximately 0.012 s^{-1}, which corresponds to the $H_{ads2} \rightarrow H^+ + e^-$ reaction. The values of k_2 at -0.5, -1.5, and -1.9 V are similar, while k_2 at -0.2 V is quite different. This suggests that the main adsorbed species are different depending on the applied voltages, and could explain why N_2H_4 was only detected at -0.2 V. From these results, it is inferred that at -0.2 V, the NRR proceeds mainly in accordance with the associative mechanism, while at higher voltages, the dissociative mechanism dominates. The value of k_2 at -0.2 V is lower than that at -0.5, -1.5, and -1.9 V, which indicates that the energy barrier for the conversion of N_2* to N_2H* is lower than that for the conversion of N* to NH*. From Table 9, it is observed that the amounts of adsorbed NH* at -0.5, -1.5, and -1.9 V are similar, which could be equal to the total number of activation sites on the catalyst surface. The coverage of the activation sites by H atoms increased as the voltage increased; the high coverage could explain why the Faradaic efficiency at -1.5 and -1.9 V is lower than that at -0.2 V and -0.5 V. The highest coverage ratio of NH* and the highest Faradaic efficiency were achieved simultaneously at -0.4 V. Results with Fe/BZY-only or RuO_2-only are summarized in Table 10, 11, 12 and 13.

Table 8 Fitting results with Fe/BZY-RuO_2 under dry Ar gas atmosphere at the cathode side.

E [V]	$k_1 \times 10^2$ [s^{-1}]	$\beta_H \times 10^7$ [mol]	*1/(RC)* [s^{-1}]
-0.2	1.0	3.9	3.9
-0.5	1.1	5.4	1.5
-1.5	1.2	9.2	1.8
-1.9	1.6	5.4	3.7

Table 9 Fitting results with Fe/BZY-RuO_2 under dry N_2 gas atmosphere at the cathode side.

E [V]	$k_1 \times 10^2$ [s^{-1}]	$k_2 \times 10$ [s^{-1}]	$\beta_H \times 10^7$ [mol]	$\beta_{NH\ or\ N_2H} \times 10^7$ [mol]	$\beta_{NH\ or\ N_2H} / (\beta_{NH\ or\ N_2H} + \beta_H)$	*1/(RC)* [s^{-1}]
-0.2	0.86	1.3	0.35	3.0	0.90	4.1
-0.4	1.0	1.8	0.39	4.0	0.91	4.8
-0.5	1.0	1.9	0.89	4.3	0.83	5.0
-1.5	1.2	1.8	1.5	4.2	0.74	4.9
-1.9	1.2	2.0	3.1	4.3	0.58	4.6

Table 10 Fitting results with RuO_2 under dry Ar gas.

E [V]	-0.5	-1.5	-1.9
$k_1 \times 10^2$ [s^{-1}]	1.3	1.3	1.6
$\beta_H \times 10^7$ [mol]	2.7	3.5	4.8
1/(RC) [s^{-1}]	2.1	4.7	5.2

Table 11 Fitting results with RuO_2 under dry N_2 gas.

E [V]	-0.5	-1.5	-1.9
$k_1 \times 10^2$ [s^{-1}]	2.9	2.9	1.6
$k_2 \times 10^2$ [s^{-1}]	3.3	3.3	2.4
$\beta_H \times 10^7$ [mol]	0.19	0.71	2.0
$\boldsymbol{\beta_{NH\ or\ N_2H}} \times 10^8$ [mol]	2.8	2.6	9.4
1/(RC) [s^{-1}]	10.7	9.7	3.1

Table 12 Fitting results with Fe/BZY under dry Ar gas.

E [V]	-0.5	-1.5	-1.9
$k_1 \times 10^2$ [s^{-1}]	1.1	1.0	1.1
$\beta_H \times 10^7$ [mol]	1.7	2.7	2.5
1/(RC) [s^{-1}]	3.3	4.1	4.5

Table 13 Fitting results with Fe/BZY under dry N_2 gas.

E [V]	-0.5	-1.5	-1.9
$k_1 \times 10^2$ [s^{-1}]	1.7	1.3	1.4
$k_2 \times 10^2$ [s^{-1}]	1.9	1.8	1.8
$\beta_H \times 10^7$ [mol]	0.97	2.0	1.7
$\boldsymbol{\beta_{NH\ or\ N_2H}} \times 10^7$ [mol]	0.32	1.0	0.68
1/(RC) [s^{-1}]	3.6	4.4	4.6

3.5 Summary and future improvements

A novel Fe/BZY cathode catalyst was synthesised and applied with the addition of RuO_2 to the electrochemical synthesis of NH_3 using a proton-conducting electrolyte CsH_2PO_4/SiP_2O_7 at 220 °C and ambient pressure. A double chamber reactor was used for electrochemical experiments, and the setup is illustrated in Fig. 32. With the addition of RuO_2, the NH_3 production rate increased and N_2H_4 was detected at -0.2 V; this might be because the oxidation of Fe was suppressed. The highest Faradaic efficiency of 7.1% was achieved at -0.4 V (vs. OCV), which exhibited the highest NH_3 yield rate of 4.5×10^{-10} mol/(s·cm^2) at -1.5 V (vs. OCV). A by-product, N_2H_4, was detected at -0.2 V (vs. OCV). While the electrochemical NH_3 production rate using only Fe/BZY or RuO_2 was approximately 1.0×10^{-10} mol/(s·cm^2), which is comparable to the N_2 reduction rate over Fe/BZY-RuO_2, no N_2H_4 was detected. An equivalent circuit model was suggested to fit the impedance spectra. The fitting results were consistent with the highest Faradaic efficiency achieved at -0.4 V. A model of the current response achieved by the potentiostatic pulse experiment was developed. The model comprised the decomposition of adsorbed intermediates on the surface of the cathode catalyst, diffusion of H in the cathode catalyst, and an electrical double layer. The current response was fitted to the model and the results showed that a high coverage ratio of NH* (and/or N_2H*) was attained at the applied voltage at which a high Faradaic efficiency was achieved, and the coverage of NH* (and/or N_2H*) on mixed Fe/BZY-RuO_2 was much higher than that on only Fe/BZY or RuO_2.

The novel contributions of this research can be summarized as follows.

(1) Ru was added to prevent Fe oxidation in the presence of small amount of steam and its effectiveness was demonstrated by the TPR experiments and the XRD of the cathode catalyst (Fig. 33) after electrolysis experiments.

(2) Since NRR is desired via association route, N_2H_4 could theoretically be produced. However, there are few reports of N_2H_4 being detected. In this work, N_2H_4 was successfully detected at -0.2 V.

(3) A new method of indirectly observing the adsorbed intermediates by modelling the time variation of current of potentiastatic pulse experiment is given. The model included reactions involving various intermediates (the observation target), diffusion of H atoms in the cathode (referred previous work of H diffusion in metal), and the electric double layer (characteristic distribution of charged particles at the boundary between the electrolyte and the electrode). As the results of the fitting based on the model, the parameter at -0.2 V (where N_2H_4 formed) was different from those only NH_3 formed, therefore, the associative reaction mechanism was confirmed.

Although the addition of Ru prevented Fe from being oxidized in the presence of small amount of steam, the NH_3 production rate decreased rapidly with time when the proton source is steam (30% humidified Ar flow on the anode side) rather than H_2. This could be due to the gas leak between the two chambers of the reactor.

I would like to thank the editor and reviewers for careful and thorough reading of the *Ammonia synthesis using Fe/BZY–RuO_2 catalysts and a caesium dihydrogen phosphate-based electrolyte at intermediate temperatures* which formed the core of the Chapter 3 in this doctoral dissertation. The thoughtful comments and constructive suggestions from the editor and reviewers will help to improve this research in the future. In future work, the $^{15}N_2$ isotopic labelling experiments will be conducted for rigorous NH_3 quantification, and it will also be useful to have a deeper understanding of the reaction mechanism. Stability tests by continuous electrolysis especially in the condition when N_2H_4 produced will be conducted.

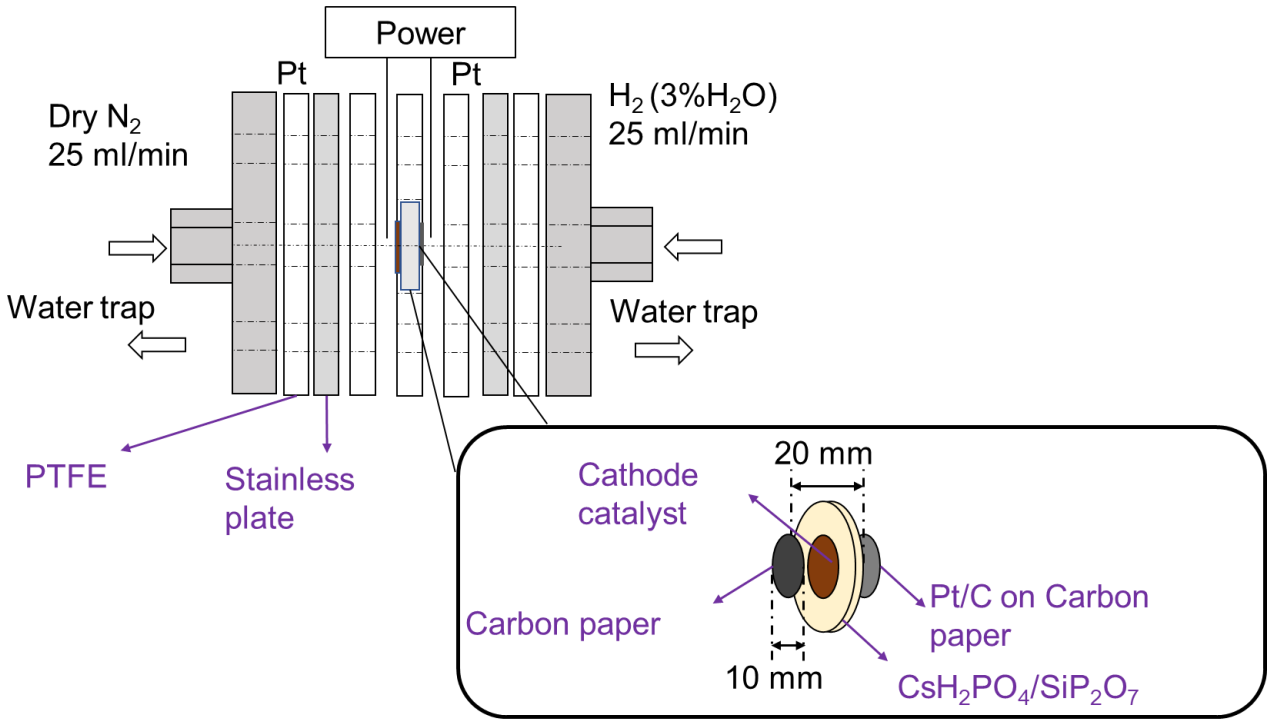

Figure 32 The schematic imagines of the double-chamber reactor and the composition of the electrolysis cell.

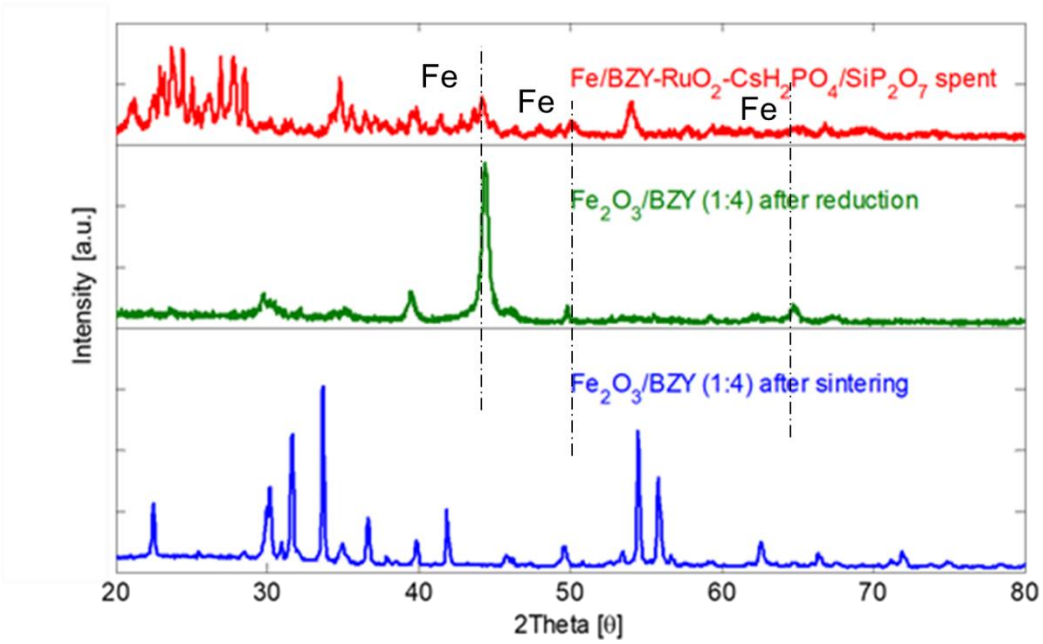

Figure 33 XRD patterns of the cathode catalyst and electrolyte mixture after electrolysis (red), Fe/BZY (green) and sintered Fe_2O_3/BZY (blue). From the red line, peaks of metallic Fe are observed. Other peaks at low degrees could contribute to $CsH_5(PO_4)_2$ phase formed in the electrolyte due to the difficulty of separating the cathode catalyst from the electrolyte.

Chapter 4: Electrocatalytic nitrogen reduction using $BaY_{0.2}Zr_{0.8}O_{3-\delta}$ electrolyte

4.1 Experimental

4.1.1 Yttrium-doped barium zirconate (BZY)

Yttrium-doped barium zirconate (BZY), as an electrolyte material with perovskite structure for proton conducting fuel cells, exhibits high bulk proton conductivity in intermediate temperature range, as well as high chemical stability and excellent mechanical strength.[77] Many studies have concentrated on decreasing grain boundary resistance in BZY. In order to enhance grain boundary conductivity, changing the characteristic of the grain boundary and reducing the grain boundary can be considered [78]. The oxides additives such as ZnO[79] were used as sintering aid in order to enhance grain sizes thus the number density of the grain boundary could be lowered. E. Fabbri *et al.*[80] have studied the effect of Y-dopant concentration on the proton conductivity of BZY. For the chemical stable BZY with Y content in the range of 0.2 to 0.5, both bulk and grain boundary conductivities decreased with increasing Y content. Here, BZY with Y dopant concentration of x is called BZYx. In this work, before the electrochemical NH_3 synthesis experiments, proton conductivities of mixed BZY10-BZY30 were measured.

4.1.1.1 Sample preparations

In this part, BZYx (x = 10, 20, 30) powders were prepared by co-precipitation method. Starting chemical materials were high purity $Ba(NO_3)_2$ (99% purity, Wako Pure Chemical Industries Ltd, Tokyo, Japan), $Y(NO_3)_3{\cdot}xH_2O$ (99% purity, Wako Pure Chemical Industries Ltd, Tokyo, Japan, where x=1.5 was determined by thermogravimetric

analysis) and $ZrO(NO_3)_2 \cdot 2H_2O$ (97% purity, Wako Pure Chemical Industries Ltd, Tokyo, Japan). The nitrates in a desired molar ratio were dissolved in deionized water. $H_2C_2O_4 \cdot 2H_2O$ was dissolved in deionized water and ammonia solution (28%~30%, Wako Pure Chemical Industries Ltd, Tokyo, Japan) was dropped into oxalic acid solution until pH was adjusted to 7~8. The nitrites solution was dropped into thus prepared oxalic ammonium solution. After stirring for one hour, the mixture was filtrated and the precursor was dried at 100 ˚C overnight. The precursor was calcined at 1200 ˚C for 12 hours to yield fine BZYx powders. From Fig. 34, BZY10 and BZY30 have the similar XRD patterns with BZY20.

The so-prepared BZYx powders were mixed with 1 wt% NiO as a sintering aid by ball milling and then the BZYx powders were pressed into pellets by cold isostatic pressing. The pellets were sintered at 1400 ˚C for a period of 12 hours. BZY10 and BZY30 powders added with sintering aid were mixed by ball-milling with different weight ratios of 1:3, 1:2, 1:1, 2:1, 3:1, and then pressed and sintered in the same way.

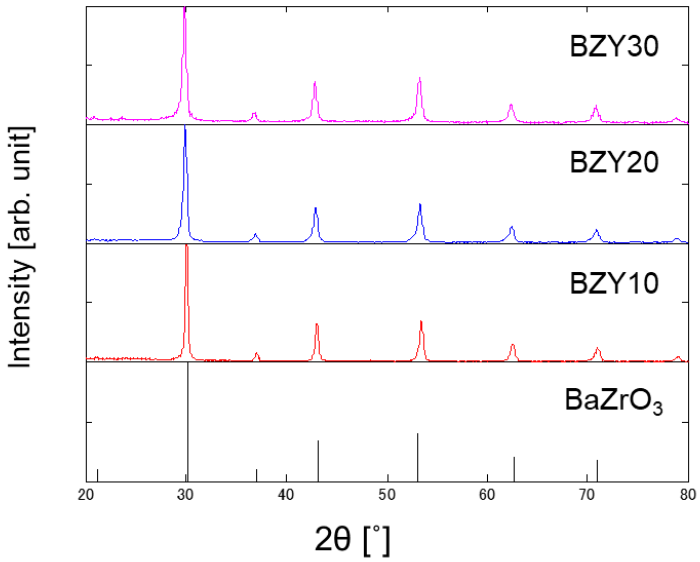

Figure 34 XRD patterns of BZY10, BZY20 and BZY30 powders.

4.1.1.2 Proton conductivity

Proton conductivities were evaluated by alternate current impedance spectra from 1 MHz to 0.05 Hz (Solartron 1260) under 240 ˚C-500 ˚C range at 80 ˚C intervals with an equilibration time of 30 minutes under humidified nitrogen (30% H_2O) with platinum electrodes.

From Fig. 35, mixed BZY10-BZY30 with ratio of 1:1 achieved the highest proton conductivity of 4.85 × 10^{-4} S/cm at 500 ˚C, and the value is higher than the proton conductivity of BZY20 which is 4.55 × 10^{-4} S/cm at 500 ˚C. The activation energies were calculated based on Appendix, and the results are shown in Table. The activation energies of BZYx are in the order of BZY20 > BZY10 > BZY30. As the proportion of BZY10 increases, the activation energy of the mixture increases. This can be easily explained by the greater activation energy of BZY10 compared to BZY30. While with higher proportion of BZY10, the activation energies of the mixtures were even higher than BZY10.

Table 14 Activation energies of BZY10, BZY20 and BZY30.

BZYx	BZY10	BZY20	BZY30
E_a [eV]	0.371	0.391	0.283

Table 15 Activation energies of BZY10:BZY30 with different ratios.

BZY10:BZY30	1:3	1:2	1:1	2:1	3:1
E_a [eV]	0.337	0.366	0.380	0.382	0.387

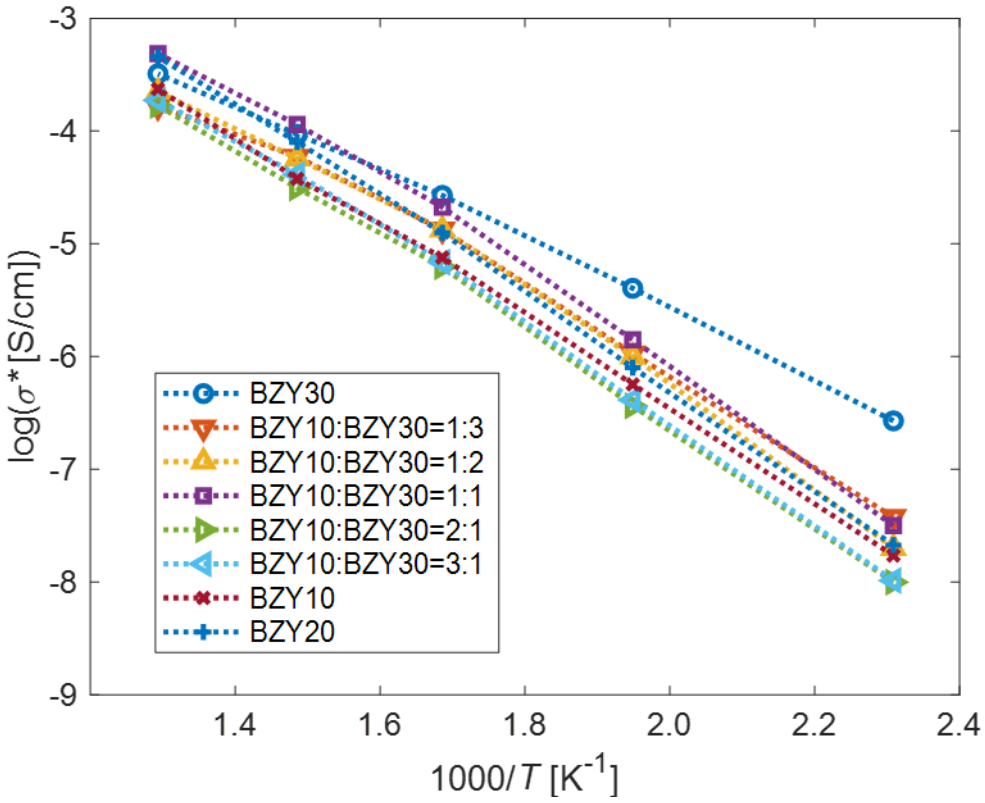

Figure 35 Proton conductivities of BZY10-BZY30 with weight ratios of 0:1, 1:3, 1:2, 1:1, 2:1, 3:1, 1:0 measured from 240 ˚C to 500 ˚C.

4.1.1.3 Interpretation based on the EMA theory

The higher proton conductivity of BZY10-BZY30 than that of BZY10, BZY30 and BZY20 is interpreted by the EMA theory. The calculation was based on Appendix. 6. For the mixed BZY10-BZY30, BZY10 and BZY30 have similar proton conductivities, so BZY10 as matrix phase and BZY30 as matrix phase have been fitted in each case. In the fitting results based on the EMA theory in Fig. 36, simulation losses are lower when BZY30 was assumed to be the matrix phase at low temperatures of 240 ˚C and 320 ˚C. While at higher temperatures of 400 ˚C and 500 ˚C, simulation losses are both high in the two kinds of matrix assumption. Such a result can be explained by the difference in the proton conductivities between BZY10 and BZY30 at different temperatures. From Fig. 35, the conductivity of BZY30 is more than 10 times greater than BZY10. Due to the low activation energy of BZY30, the difference between BZY10 and BZY30 becomes smaller as the temperature increases, therefore the assumption that one of the phases is the matrix and the other is the insulator phase does not work, and the fitting losses became larger. Table 16 summarizes the fitting parameters.

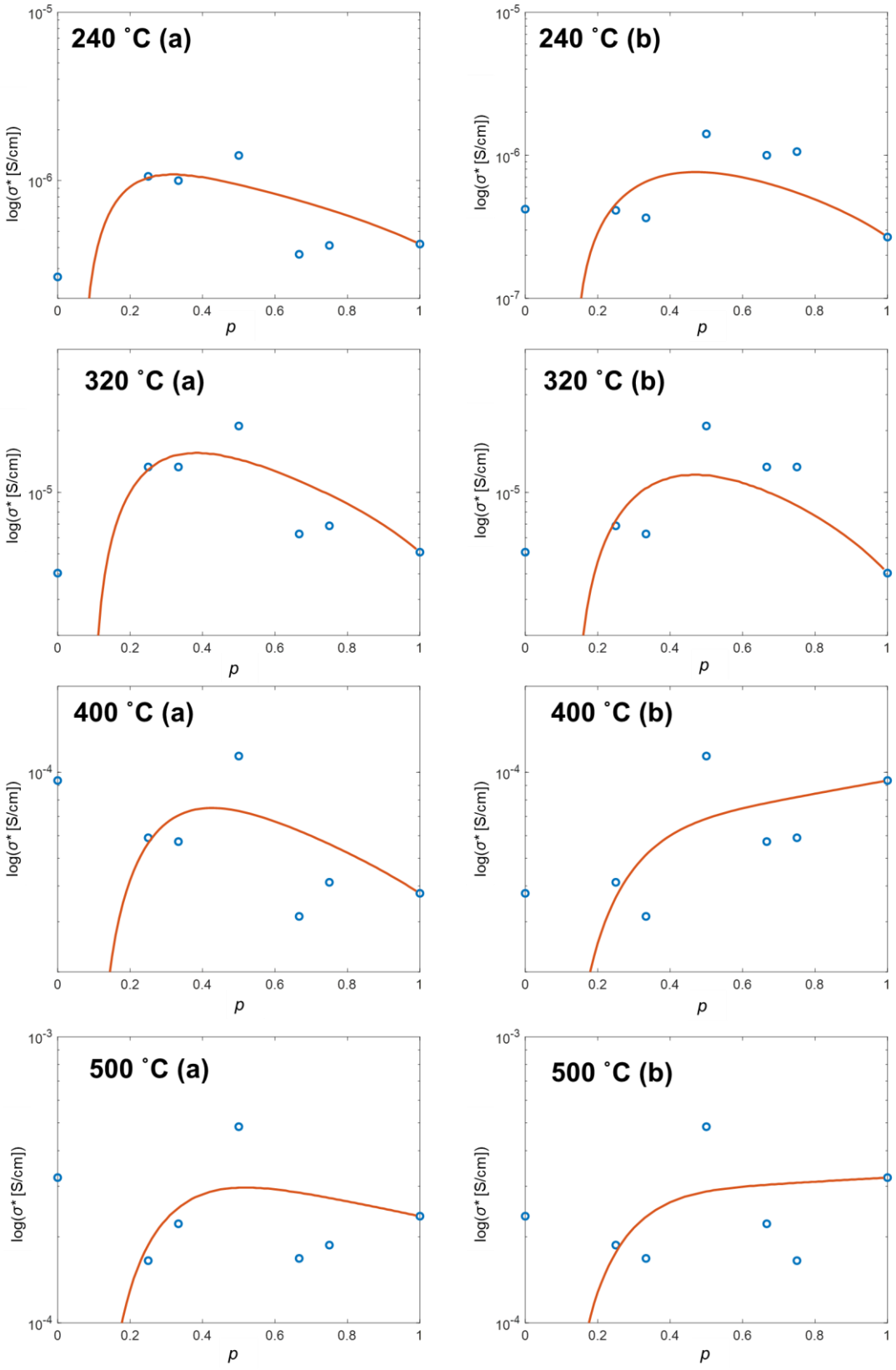

Figure 36 The proton conductivities of mixed BZY10-BZY30 with different ratio. (a)

BZY30 assumed to be the matrix phase. (b) BZY10 assumed to be the matrix phase. Bule circles are experimental data, and the red line is the simulation curve.

Table 16 Parameters obtained with BZY10 as matrix phase and BZY30 as matrix phase.

T [˚C]	p	$\sigma_0 \times 10^8$ [S/cm]	$\sigma_2 \times 10^5$ [S/cm]	m
240	BZY10	3.40	0.172	1.70
	BZY30	0.178	0.178	3.00
320	BZY10	0.299	2.98	4.00
	BZY30	0.311	2.89	3.97
400	BZY10	1.31	13.1	4.00
	BZY30	0.542	5.42	4.00
500	BZY10	4.07	40.7	4.00
	BZY30	2.72	27.2	4.00

4.1.2 Preparation of the electrolysis cell

In the electrochemical experiments, $BaZr_{0.8}Y_{0.2}O_{3-\delta}$ (BZY20) was used as the electrolyte. BZY powders were prepared by a conventional solid-state reaction method. $BaCO_3$ (98% purity, Wako Pure Chemical Industries Ltd, Tokyo, Japan), Y_2O_3 (99.9% purity, Wako Pure Chemical Industries Ltd, Tokyo, Japan) and ZrO_2 (98% purity, Wako Pure Chemical Industries Ltd, Tokyo, Japan) were mixed in stoichiometric quantities by ball-milling in ethanol overnight. The mixture was heated to dry and then calcined at 1400 ˚C for 12 h to form BZY powders. NiO (99.0+% purity, Wako Pure Chemical Industries Ltd, Tokyo, Japan) as sintering aid (1 wt%) was added into the BZY powders, and the mixture was ball-milled followed by press at 20 MPa for 10 min to form a ⌀20 mm pellet. The pellet was then pressed at 200 MPa by cold isostatic pressing for 15 min. After that, it was sintered at 1400 ˚C for 12 h and finally formed a ⌀15 mm, thickness 1 mm pellet.

From Fig. 37, The XRD patterns of BZY exhibit typical perovskite structure. The size of BZY crystallites (sintered NiO-BZY20) is 30.8 nm by Scherrer equation. SEM micrographs in Fig. 38 of the sintered BZY confirms the high density.

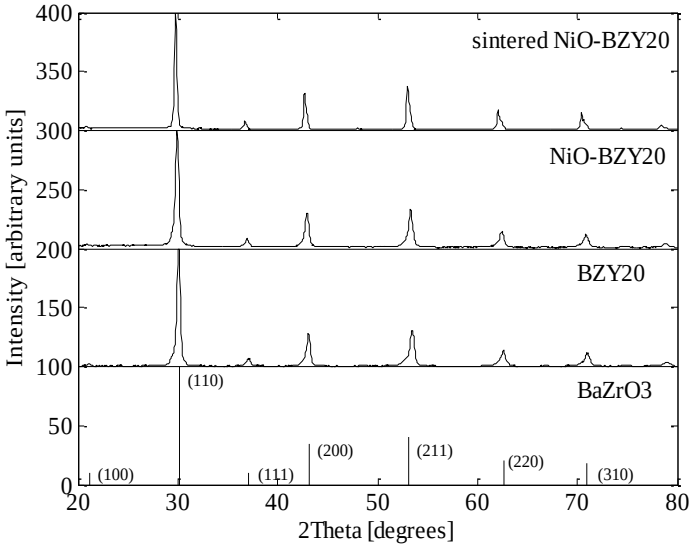

Figure 37 XRD patterns of $BaZrO_3$, BZY powders, BZY powders mixed with 1 wt% NiO after ball milling and sintered BZY.

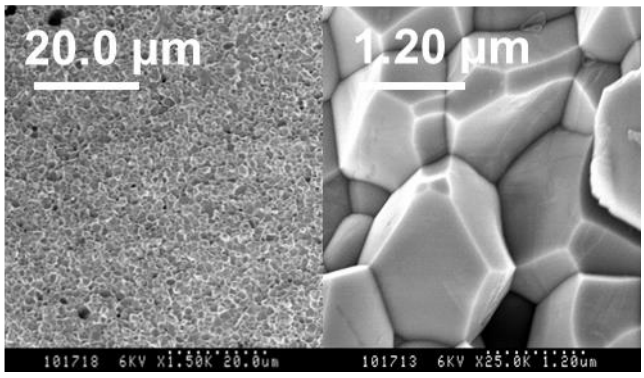

Figure 38 Morphology of sintered BZY.

Proton conductivity of obtained sintered BZY pellet was evaluated by alternate current

impedance spectra from 1 MHz to 0.05 Hz under 80 ˚C-400 ˚C range at 20 ˚C intervals with an equilibration time of 30 minutes under humidified N_2 (30% H_2O) with platinum electrodes. Compared with the reference data with Ag electrodes from Fig. 39, the activation energies of sample in this work and in the reference are 0.391 eV and 0.269 eV.

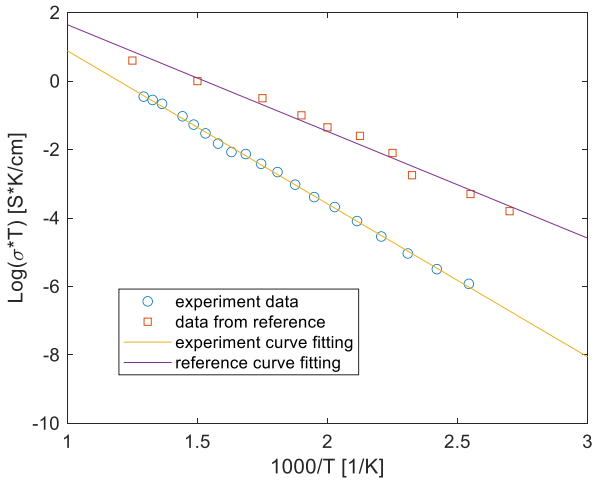

Figure 39 Proton conductivities of the as-prepared BZY pellet and from Babilo *et al.*[81]

4.1.3 Preparation of cells and experimental setup

As-prepared calcined Fe_2O_3/BZY disk was attached to BZY pellet by Pt paste. Pt paste was also used as the anode catalyst for H_2 dissociation. Pt wires connected to the Pt paste on both sides were used as terminals. Finally, the cell was heat-treated at 900 ˚C for 2 h. The-prepared cell was set up in a quartz glass tube with 17 mm diameter as a simple single-chamber reactor illustrated in Fig. 40. Experiments were carried out in a gas mixture of N_2 and H_2 with a total gas flow rate of 50 ml/min at ambient pressure and 500 ˚C. The outlet gas was trapped by distilled water for 30 min and ammonia was quantified

by salicylate method.

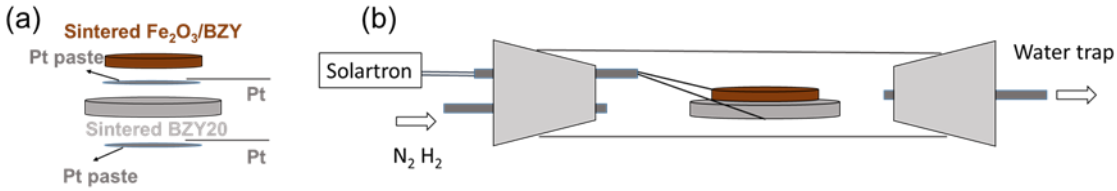

Figure 40 (a) Preparation of the cell for electrocatalytic NH_3 synthesis. (b) Illustration of the single-chamber setup.

4.1.4 Control experiment at open circuit conditions

Because ambient NH_3 in air, nitrogen-containing precursors of the catalyst, and the catalyst itself can be a source of contaminant NH_3, accurate and reliable measurements of NH_3 produced by catalytic and electrocatalytic reactions are necessary.[82] Three types of blank tests for the accurate and reliable NH_3 quantification were carried out: Blank experiment 1 was carried out at 500 °C in dry Ar gas flow of 50 mL/min at open circuit voltage, Blank experiment 2 was carried out at 500 °C in dry N_2 gas flow of 25 mL/min at open circuit voltage, and Blank experiment 3 was carried out at 500 °C in dry H_2 gas flow of 25 mL/min at open circuit voltage and applied voltage of -0.6 V. The outlet gas was trapped by distilled water for 30 min and then analysed. The collection time is longer than or equal to that in the following catalytic and electrolysis experiments.

The amount of trapped NH_3 during the blank experiments was below the detection limit (0.01 mg-N/L, equivalent to 2.5×10^{-11} mol/(s cm^2) during 30 min of collection period).

Therefore, the effect of ambient NH_3 could be ignored. Furthermore, there is no N_2H_4 detected in the blank experiments (1 μg N_2H_4/L is equivalent to 1.1×10^{-12} mol/(s cm^2) during 30 min of collection period). Since the reagents used to synthesize the catalyst and electrolyte did not contain any N, it was confirmed that the origin of N in the produced NH_3 could be from the N_2 gas in the feed.

4.1.5 Evaluation of catalytic activity for thermochemical reaction and electrochemical reactions

The cell was pretreated at 500 °C for 1 hour in H_2 gas flow (50 mL/min) before NH_3 synthesis tests. After the pretreatment, the gas flow was turned to a gas mixture of N_2 (25 mL/min) and H_2 (25 mL/min). In order to distinguish NH_3 produced by thermochemical or/and electrochemical effect from the total reaction rate, NH_3 synthesis experiments at open circuit voltage using the as-prepared cell were carried out. The outlet gas was trapped by distilled water for 10 min at an interval of 10 min until the reaction rates reached to the steady rates.

In an electrolysis mode for NH_3 synthesis, a direct current voltage versus open circuit voltage was applied between the anode and cathode in a potentiostatic mode. The outlet gas was trapped by distilled water for 30 min.

4.1.6 Characterizations of prepared materials

An X-ray diffractometer was operated at 100 kV-40 mA in 20°-80° 2θ range (XRD, Rigaku RINT 2400). Morphology of the cross section obtained by mechanical

cracking of the sample was observed by a scanning electron microscopy (SEM, Hitachi S-900). The elemental composition was analysed by a SEM equipped with an energy dispersive X-ray (EDX, Super Xerophy, Horiba) detector. Alternative current impedance was measured from 1 MHz to 0.05 Hz with a voltage amplitude of 14.1 mV (Bio-Logic SP 300, Seyssinet-Pariset).

4.2 Results and discussion

4.2.1 Results of characterizations

After sintering at 1300 °C for 12 hours, part of α-Fe_2O_3 was transformed into ε-Fe_2O_3 and γ-Fe_2O_3 (Fig. 3 in Chapter 2). Peaks of $BaCO_3$ could be observed from the XRD pattern of sintered Fe_2O_3/BZY, which implies part of BZY decomposed during sintering. The XRD pattern of spent Fe/BZY designated that Fe_2O_3 was reduced into Fe. Decomposition of BZY during the electrocatalytic reaction was suggested by the intensity decrease of the perovskite peaks and the intensity increase of $BaCO_3$ peaks after the electrocatalytic reaction. Peaks of γ-Fe could also be observed in the XRD pattern of spent Fe/BZY which are much weaker than those of α-Fe.

Morphology of the cross section indicates a dense structure of sintered Fe_2O_3/BZY (Fig. 4 in Chapter 2). After the electrocatalytic reaction, spent Fe/BZY became porous, and different morphologies such as blocks, layers, and particulates, are observed (Fig. 5 in Chapter 2). Most interestingly, several hexagons with diameters of less than 2 μm distributed on the surfaces of the blocks (Fig. 5 in Chapter 2). Those hexagons are inferred to be γ-Fe, which has fcc phase and is expected thermodynamically to exist at high temperatures and low pressures.[70] Both γ-Fe and α-Fe have bcc phase and coexist at about 600 °C.[71] Effect of applied voltage might have led to the phase transformation from α-Fe to γ-Fe in the part of Fe/BZY at 500 °C and ambient pressure.

4.2.2 Evaluation of catalytic activity and reaction rates under applied voltages

From the comparison of the catalytic and electrochemical reactions in Fig. 41, the NH_3 production rate gradually increased not only at OCV but also under applied voltages as the time on stream was elapsed. Investigation of high-pressure electrochemical promotion of NH_3 synthesis using an industrial Fe-based catalyst reported a similar slow catalytic response, and the authors ascribed the slow response to a long residence time of about 150 min.[83] While in this work, the single-chamber reactor is a simple tube with a length of 40 cm and an inner diameter of 17 mm. Therefore, the residence time, which is estimated to be about 0.55 min, cannot be the reason for the slow response in the NH_3 production rate. As N_2 gas flow was introduced at the same time of outlet gas trapping following to the reduction process of Fe_2O_3/BZY in H_2 gas flow, it is supposed that the catalyst surface was fully covered with H adatoms initially. Then the adsorbed H atoms were gradually released in the mixed gas flow, and thus the number of unoccupied active sites for N_2 activation increased and led to the promotion of the production rate.

The NH_3 production rate at OCV became stabilized at 1.61×10^{-9} mol/(s cm^2) (equivalent of 2.10×10^{-9} mol/(g-cat s)) after more than 100 min of reaction time elapsed. A constant potential (-0.6 V) applied from 0 to 450 minutes enhanced the reaction rate compared with the thermal catalytic test in the same condition, and finally the production rate reached a steady value of 2.71×10^{-9} mol/(cm^2 s). Constant polarization at -0.6 V caused a constant current I = -1.0 mA with a $-I/F$ = 1.0×10^{-8} mol/s supply of protons to Fe/BZY catalyst. The enhancement factor defined as $\Lambda = (r - r\text{-cat}) \times 3/(-I/F)$ is 25.1% where r-cat is the steady catalytic

production rate at OCV, and *F* is Faraday constant. The applied voltage of -0.6 V was then switched to OCV at 450 min. After that, the reaction rate decreased gradually and finally dropped to 1.41 mol/(s cm^2) (equivalent of 1.85×10^{-9} mol/(g-cat s)), which is close to the steady production rate by thermal catalytic reaction. In addition, the reaction rate decrease to the steady rate at OCV was not steep but gradual after the switch to OCV level. It is a typical transient behaviour which has been commonly reported in studies about the non-faradic electrochemical modification of catalytic activity (NEMCA) effect.[84] This kind of behaviour shows the production rate promotion is not an telectrocatalytic phenomenon, but a catalytic one. Evidence that the reaction rate increased with reaction time is not due to the reduction of the Fe_2O_3 in the cathode catalyst is given below.

(1) From the XRD patterns of produced Fe/BZY catalyst in the characterization results Fig. 3, the intensity of the metallic Fe peaks is much stronger than that of the other oxide peaks, which implied most of the Fe presented as metallic Fe.

(2) From the current correspond to applied voltages in Fig. 44, the current remained throughout the application of the constant voltage, which means that the electrode material has not changed.

(3) From the comparison of the catalytic reaction rate and the reaction rate at -0.6 V in Fig. 41, after switched to OCV from the steady state at -0.6 V, the reaction rate dropped to the steady catalytic reaction rate. The catalytic reaction rate did not change after the reaction at the applied voltage, suggesting that the amount of metallic Fe did not change.

(4) As a supplement to (3), an experiment in the condition of applied -0.6 V for 60 min, then switched to OCV, after that, applied -0.6 V again was carried out.

From the result shown in Fig. 45, the production rate increased along with the reaction time at applied -0.6 V firstly, and then gradually decreased after switching to OCV, and the production rate increased when -0.6 V was applied again.

Potential effect on NH_3 production rate was studied with various bias potentials. The results depicted in Fig. 42 show that the reaction rates were accelerated with negative potentials and reached to steady reaction rates of 1.50×10^{-9} mol/(s cm^2), 2.71×10^{-9} mol/(s cm^2), 3.07×10^{-9} mol/(s cm^2), 1.87×10^{-9} mol/(s cm^2), and 6.15×10^{-10} mol/(s cm^2) at -0.4 V, -0.6 V, -0.7 V, -0.9 V, and -1.2 V, respectively. The maximum steady rate of 3.07×10^{-9} mol/(s cm^2) was achieved at -0.7 V. At higher potentials, the reaction rate decreased significantly and even led to a negative calculated Λ value at -1.2 V, as summarized in Fig. 43, which means catalytic activity decreased at -1.2 V from OCV.

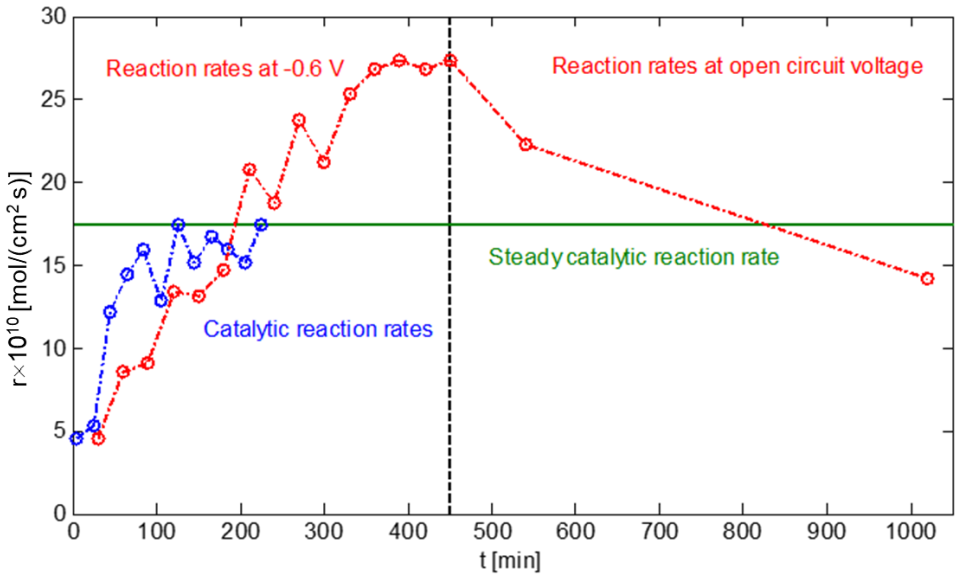

Figure 41 Comparison of catalytic reaction (blue line) and electrocatalytic reaction (red line) rates. In the red line, -0.6 V was applied from 0 to 450 minutes. From 450 to 1020 minutes, reaction was carried at open circuit voltage.

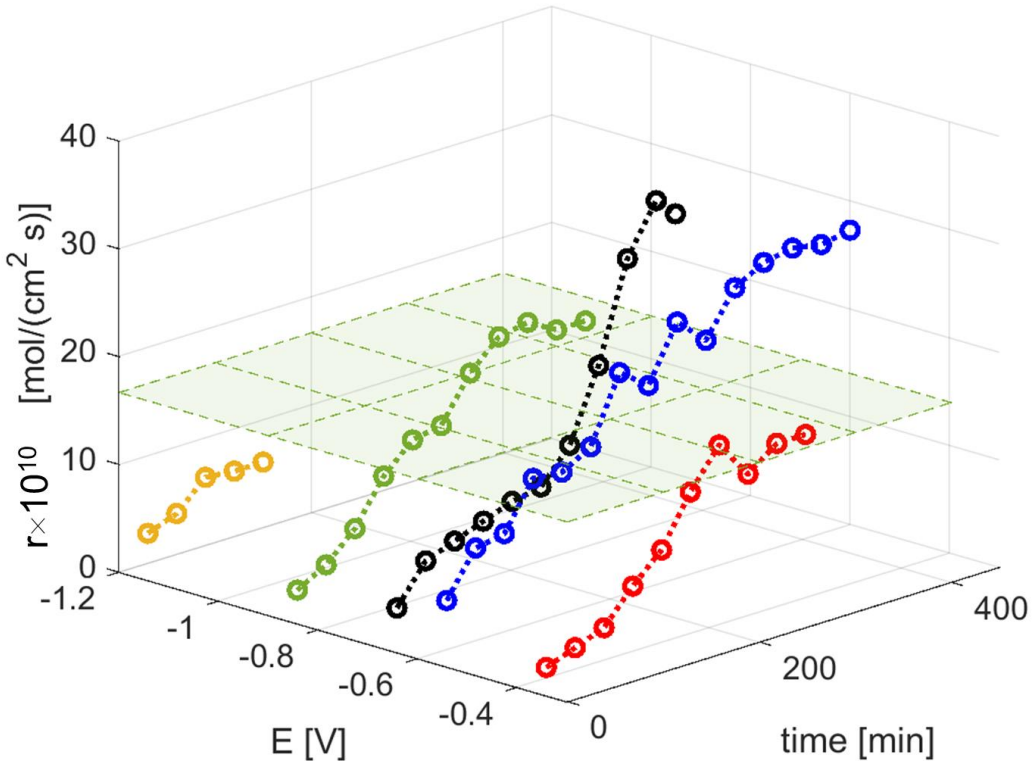

Figure 42 Reaction rates with applied voltages of -0.4 V (red), -0.6 V (blue), -0.7 V (black), -0.9 V (green) and -1.2 V (orange). Light green mesh stands for steady catalytic reaction rate.

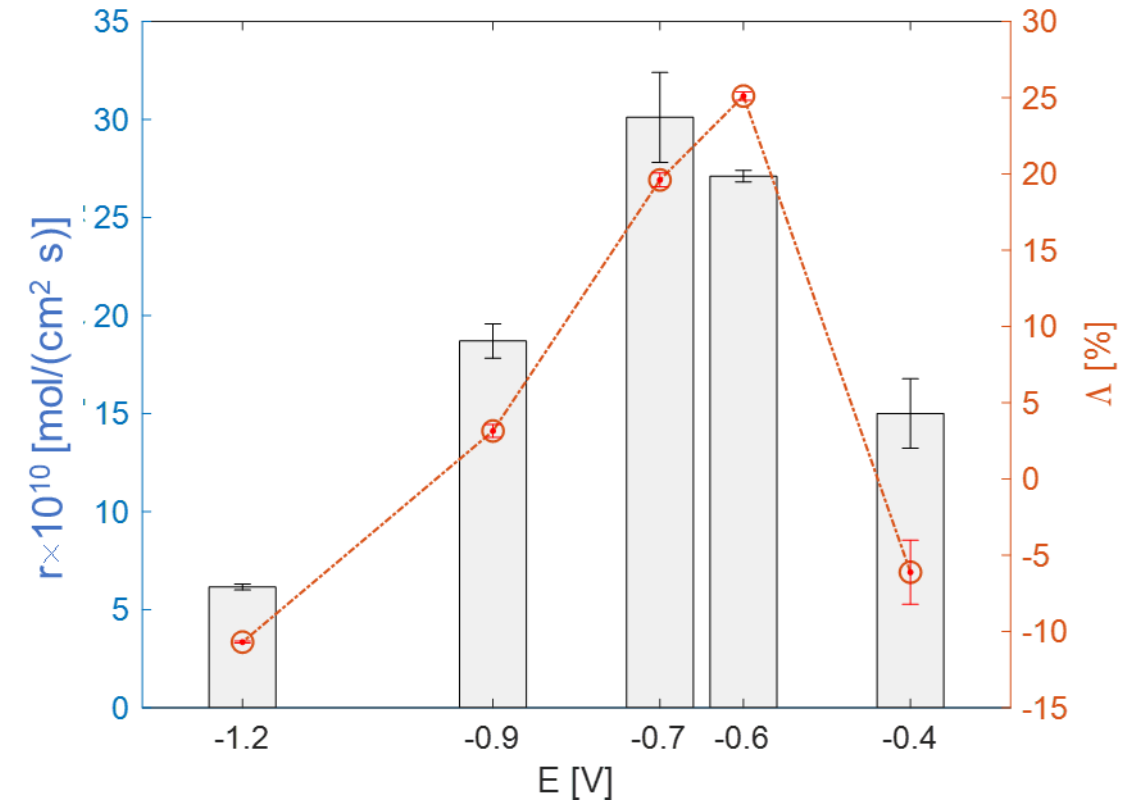

Figure 43 Steady reaction rates (blue bar) and Faradaic efficiencies (green) at the applied voltages of -0.4 V, -0.6 V, -0.7 V, -0.9 V and -1.2 V. The error bars are standard deviations.

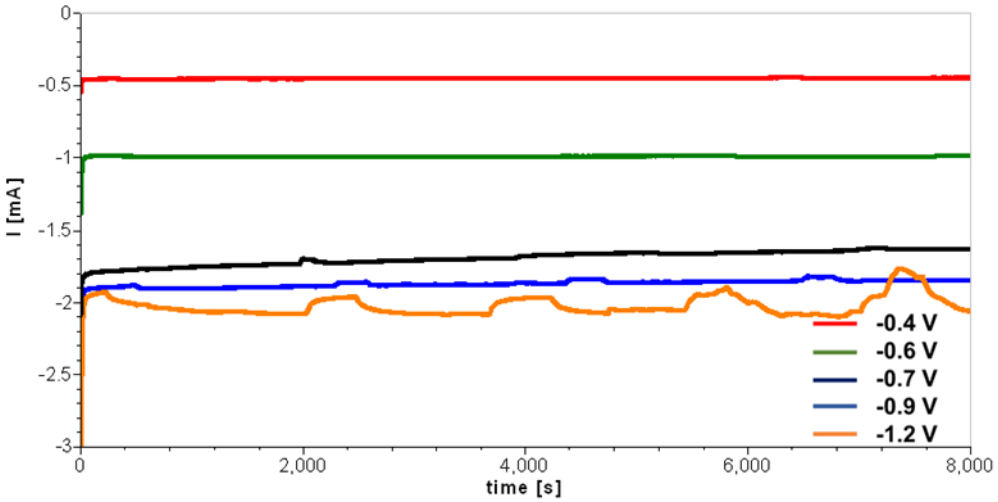

Figure 44 Currents correspond to applied voltages.

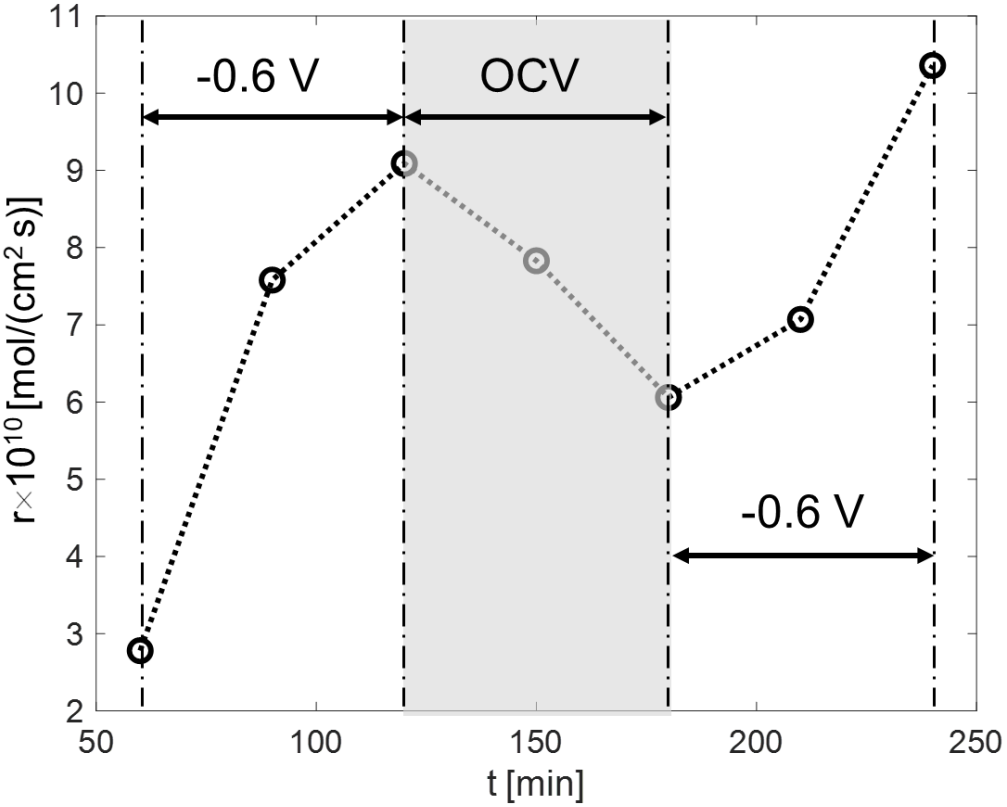

Figure 45 NH_3 production rate against time in the condition of applied -0.6 V for 60 min, then switched to OCV, after that, -0.6 V was applied again.

4.3 Thermochemical calculation

Fig. 8 shows the NH_3 equilibrium production rate at 500 °C. The equilibrium constant K calculated for NH_3 production from N_2 and H_2 is 7.17×10^{-5} (coefficients for $\boldsymbol{c_p}^\circ$ calculation and standard enthalpy for formation and standard entropy are listed in Appendix 1). With the H_2 and N_2 gas flow rate of 25 mL/min (6.57×10^{-6} mol/s equivalent) at the inlet, the calculated NH_3 equilibrium production rate (r_{eq}) is 1.38×10^{-8} mol/s. Protons pumped from anode to cathode side can cause an increase in H_2 concentration. H_2 flow rate at applied voltages (f_{eq} at applied voltages) was calculated from the sum of the inlet flow rate of 25 mL/min and H_2 produced from the protons with an assumption of current efficiency = 1. H_2 production rate from the protons was calculated by:

$$f = \frac{I}{1.602 \times 10^{-19} \times N_A \times n}$$

Where the fixed numerical charge value of elementary electron is 1.602×10^{-19} C, and N_A is the Avogadro constant and is 6.022×10^{23} mol^{-1}. The symbol n is equal to 2, which means that 2 moles of electrons are consumed for every 1 mole of H_2 produced. I is the current at each constant voltage. As a result, r_{eq} at the applied voltages is slightly higher than r_{eq} at OCV, and the experimentally measured NH_3 production rate is lower than theoretically calculated NH_3 production rate for the equilibrium.

Figure 46 shows the NH_3 equilibrium production rate at 500 °C with different inlet N_2 gas fractions. The total gas flow rate is 50 mL/min (1.31×10^{-5} mol/s equivalent). As a result, the highest NH_3 production rate is achieved with a gas ratio of N_2:H_2 = 1:3, and N_2 conversion increase with decreasing N_2 fraction. Fig. 10 shows the mathematical solution derived from the reaction equilibrium calculation given as:

$$\frac{2^2 \times y^2 \times \left(\frac{1}{x} - 2y\right)^2}{(1-y) \times \left(\frac{1}{x} - 1 - 3y\right)^3} = K$$

The symbols x and y stand for $N_2/(N_2 + H_2)$ and the N_2 conversion ratio, respectively. K means the equilibrium constant at 500 °C which is 7.17×10^{-5}. It can be seen in Fig. 47 that the N_2 conversion increases as the fraction of N_2 decreases.

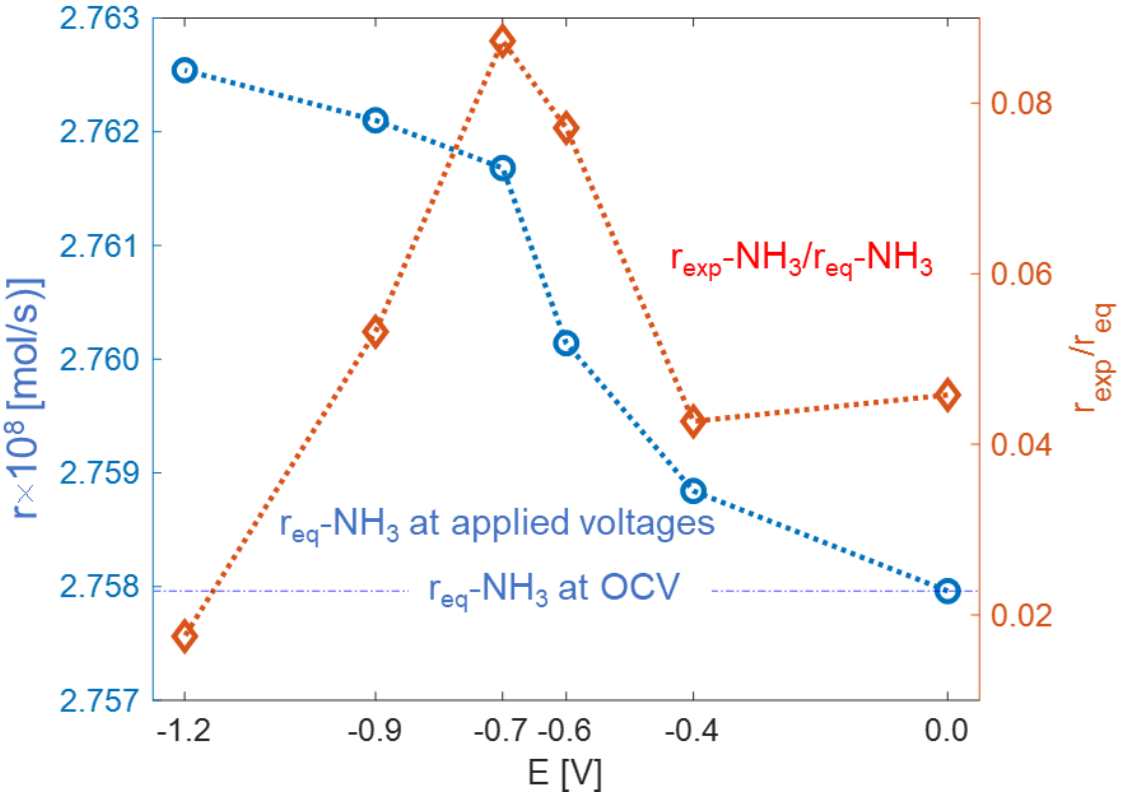

Figure 46 Equilibrium NH_3 production rate (r_{eq} at OCV) calculated with equilibrium constant of 7.17×10^{-5}. The blue dotted line (r_{eq} at applied voltages) stands for equilibrium NH_3 production rate at applied voltages. The red dotted line corresponds to the right y axis means proportion of experimental NH_3 production rate (r_{exp}) to theoretical equilibrium NH_3 production rate (r_{eq}).

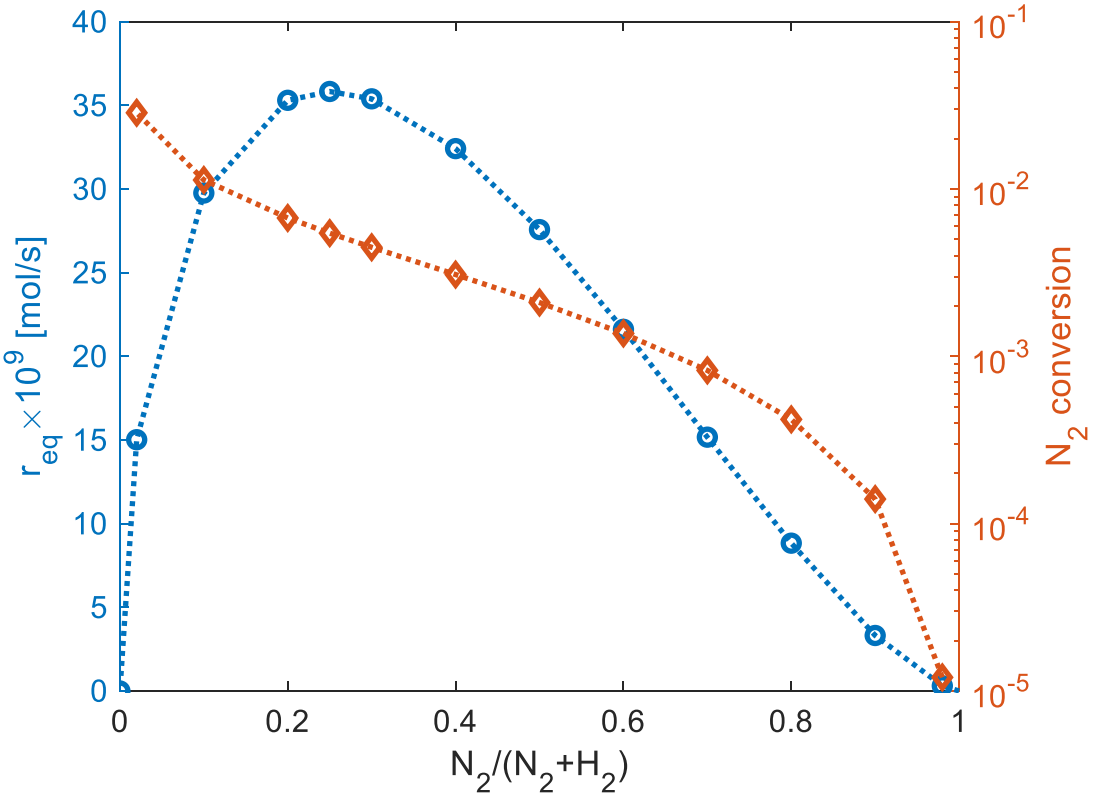

Figure 47 Equilibrium NH_3 production rate (r_{eq}) calculated with equilibrium constant of 7.17×10^{-5} and plotted against N_2 gas flow fraction. The total inlet reactant H_2 and N_2 gas flow rate is 50 ml/min. N_2 conversion is plotted in a semi-log plot.

4.4 Impedance analysis

Alternative current impedance spectra of Fe/BZY-Pt|BZY|Pt cell was measured in 50 ml/min mixed N_2 and H_2 with different flow ratios of N_2 and H_2 (30:20, 25:25, 20:30, 12.5:37.5 and 0:50). A typical equivalent circuit illustrated in Fig. 48 successfully fitted the experimental results. In this equivalent circuit, Rs is constant ohmic resistance and related to resistance of measuring equipment and wires. R_1 is relative to reactions on electrodes, and in this case, the electrode reaction is HER. R_2 stands for slow processes such as gas diffusion. CPE is a constant phase element that was discovered in order to reflect the actual behavior of capacities.[85] Surface roughness, inhomogeneous reaction rates on a surface, varying thickness or composition and non-uniform current distribution could cause a CPE. In equivalent circuit fitting result of Fe/BZY-Pt|BZY|Pt in Fig. 49, the minimum R_1 achieved with a gas ratio of 1:3 (12.5ml/min:37.5ml/min). In pure H_2 atmosphere, R_1 is larger than in mixed gases. It is because NRR speeds up the consumption of H adatoms and leads to lower R_1 in mixed gases. The impedance fitting results in Table 17 were calculated by Appendix.

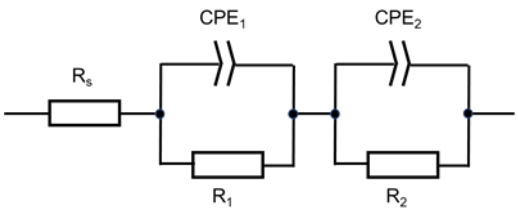

Figure 48 Illustration of the equivalent circuit for Fe/BZY-Pt|BZY|Pt cell.

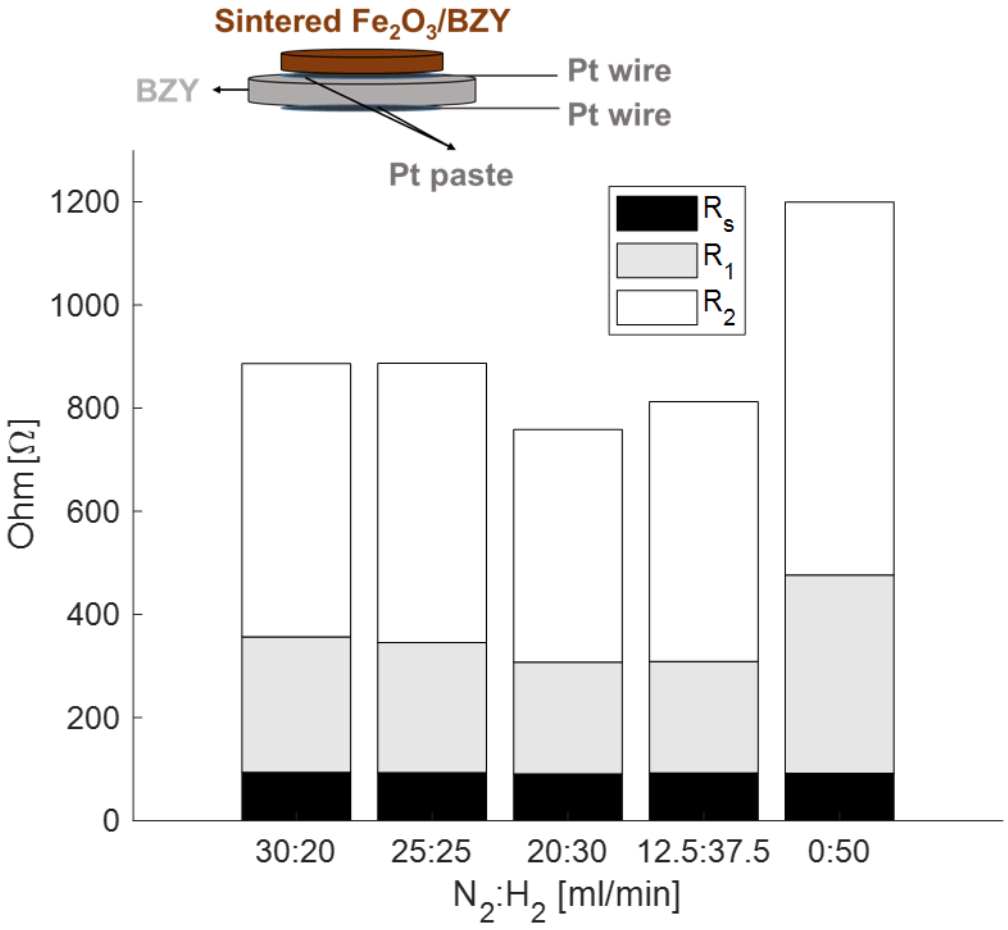

Figure 49 Fitting results based on the equivalent circuit illustrated above under different gas ratios.

Table 17 Impedance fitting results of Fe/BZY-Pt|BZY|Pt in mixed N_2 and H_2.

Gas ratio N_2:H_2	R_s [Ω]	R_1 [Ω]	CPE_1-T [$F \cdot s^{CPE1-P-1}$] $\times 10^{-4}$	CPE_1-P	R_2 [Ω]	CPE_2-T [$F \cdot s^{CPE2-P-1}$] $\times 10^{-6}$	CPE_2-P	f_1 [Hz]	f_2 [Hz] $\times 10^4$
30:20	93.4	263	6.07	0.385	530	4.47	0.478	18.8	4.99
25:25	93.1	252	5.95	0.389	542	4.28	0.478	20.7	5.16
20:30	90.6	217	6.84	0.357	451	4.76	0.476	33.4	6.34
12.5:37.5	92.5	216	6.11	0.388	504	4.25	0.479	29.4	5.94
0:50	91.7	385	3.84	0.349	723	2.85	0.487	38.1	5.28

4.5 Model of slow ammonia production rate response and potential dependency

Since no N_2H_4 was detected and the reactions were carried out under mixed gas flow at a high temperature relatively. Electrochemical NRR was supposed to be via the dissociative pathway. Reaction steps were given as:

$$N_2 + 2* \xrightarrow{k_1} 2N* \quad \#eq.1$$

$$N* + 3H_s \xrightarrow{k_2} * + NH_3 + 3V_H \quad \#eq.2$$

$$H_2 + 2V_H \xrightarrow{k_3} 2H_s \quad \#eq.3$$

$$(\text{Tafel})\,2H_s \xrightarrow{k_{-3}} H_2 + 2V_H \quad \#eq.4$$

$$(\text{Volmer})\,V_H + H^+ + e^- \xrightarrow{k_4} H_s \quad \#eq.5$$

$$(\text{Heyrovsky})\,H_s + H^+ + e^- \xrightarrow{k_5} H_2 + V_H \quad \#eq.6$$

In these reaction steps, * means N active sites, V_H is H active sites, N* and H_s are adsorbed N and H atoms, respectively. Reaction rate constants are represented as k_i (i = 1, 2, 3, 4, 5, -3) in each equation. Hydrogen evolution reaction (HER) proceeds via the Volmer-Tafel (Eqns. 4, 5) and/or Volmer-Heyrovsky (Eqns. 5, 6) steps.[86] A previous study on HER of metal electrode by density functional theory (DFT) showed the Volmer reaction is the fastest while the Tafel reaction is the rate-determining step. The rate of the Tafel reaction is indirectly influenced by the H coverage on the surface.[87] In the case of the most studied HER and oxygen evolution reaction (OER) on Pt electrodes, a study of hydrogen oxidation reaction (HOR) on Pt showed that the Volmer-Tafel pathway is dominant at low overpotentials while at high overpotentials, Volmer-Heyrovsky pathway is dominant.[88] The NH_3 production rates against reaction time at various bias

potentials were fitted based on the reaction equations above. Besides, the following assumptions were added to the fitting model.

(1) As the NH_3 generation reaction was started subsequently to the catalyst reduction pre-treatment, the initial coverage of N active site (*) is 0 while H active site (V_H) is 1.

(2) k_i (i = 2, 3, 4, 5, -3) are fitted as common parameters

(3) With applied voltages, since the amount of proton (H^+) supply is much higher than H_s used in NH_3 formation, H_s will only be generated from the combination of H^+ and e^-, which means the *eq.3* will not occur with bias potentials applied.

(4) The catalytic NH_3 synthesis step *eq. 2* is much faster than direct interaction of N*, H^+ and e^-, therefore the NH_3 production by $N* + 3H^+ + 3e^- \rightarrow * + NH_3$ is ignored.

(5) For the catalytic reaction, only eqns.1, 2, 3, 4 were used in the simulation.

Since it has a continuous and excess gas supply of reactant H_2 and N_2, the concentrations of H_2 and N_2 in *eq.1* and *eq.3* are taken as dimensionless constants and defined as 1. In order to incorporate the effect of the concentration of H_S on the production rate, the reaction rate equation of *eq.1* is given as:

$$2\frac{dN*}{dt} = k_1[*]^2/[H_s] \quad \#eq.7$$

For $N_2 + 2* \xrightarrow{k_1} 2N* \ \#eq.1$, the reaction rate equation of $2\frac{dN*}{dt} = k_1[*]^2$ and $2\frac{dN*}{dt} = k_1[*]^2/[H_s]^2$ are also tried for simulation. However, losses calculated by $\sum_{experimental}(\sum_{time}[NH_3\ error]^2/\sum_{time}[NH_3\ experimental]^2)$ with $2\frac{dN*}{dt} = k_1[*]^2$ and $2\frac{dN*}{dt} = k_1[*]^2/[H_s]^2$ are quite large. Although the flow rates of N_2 and H_2 are

known, the concentrations of N_2 and H_2 on the surface of the catalyst are unknown. Since the flows of N_2 and H_2 are far in excess relative to reaction intermediates and products, the concentrations of N_2 and H_2 are both set to be a constant dimensionless number 1. Experimental and simulated NH_3 production rates against time were plotted in Fig. 50, 51. According to the simulation results, slow production response against time in catalytic, -0.4 V, -0.6 V and -0.7 V fitted well with the above model (Fig. 50). Obtained parameters and variations in the amount of each chemical species against time were showed in Table 18, 19 and Fig. 52, 53. From Table 18, the main NH_3 production reaction (*eq. 2*) and the Tafel step (*eq. 4*) are almost independent of the applied voltages. The reaction rate constant (k_2) for the main NH_3 production reaction (*eq. 2*) is 11.56 mol^{-3} s^{-1} under applied voltages and 2.74 mol^{-3} s^{-1} at OCV. The reaction rate constant (k_{-3}) for the Tafel step (*eq. 4*) is 1.21 mol^{-1} s^{-1} under applied voltages and 1.28 mol^{-1} s^{-1} at OCV. The N_2 dissociation rate constant (k_1) varies with the applied voltages. The value of k_1 at -0.4 V is about 4 times larger than that at OCV (7.84×10^{-5} mol^{-1} s^{-1}), and at -0.6 V and -0.7 V, it drops to about 1/40 and more than 1/100 of the OCV value. It may be possible because the polarization leads to a phase transition in Fe and consequently to a difference in k_1. The slow NH_3 production rate response may not only be due to the slow adsorption of N adatoms on the catalyst surface covered with H adatoms which is mentioned in Figure 41, 42, but also due to the slow formation of nitrides on Fe surface during NH_3 synthesis process,[89] and the thus formed nitrides accelerate the NH_3 production rate. In addition, Tafel step (*eq. 4*) is much faster than Heyrovsky step (*eq. 6*). The reaction rate constant of the N_2 dissociation (k_1) increased from OCV to -0.4 V and then decreased with the applied voltage. By applying voltages, both

N* and H_s significantly decreased compared with the OCV condition. The fact that H_s was reduced by a factor of 10,000, whereas N* was reduced by only 100, is thought to be the main factor why the maximum NH_3 production rate under applied voltage is higher than that in the OCV state. It means when the amount of N* is considerably greater than that of H_s, it is favourable for NH_3 production. Figure 54 shows (a) N^*/H_S and (b) $[*]^2/H_S$ versus reaction time. It is clear from Fig. 15(a) that there is much more N* than H_S when the voltage is applied. Under the applied voltages, the order of the maximum NH_3 yielding rate is -0.7 V > -0.6 V > -0.4 V, which corresponds to the decreasing order of N^*/H_S as the applied voltage changed from -0.7 V to -0.4 V. This shows that a higher ratio of N* to H_S is desirable for NH_3 formation, but a too high N^*/H_S is detrimental to NH_3 formation as it results in few or no adsorbed H atoms adjacent to N*. The $[*]^2/H_S$ in Fig. 54 relates to the N_2 dissociation reaction rate equation (eq. 1), and the order of $[*]^2/H_S$ with the applied voltage is the same as that of NH_3 yielding rate from -0.7 V to -0.4 V. Simulations at the applied voltages of -0.9 V and -1.2 V presented large discrepancies between the experimental and calculated values by the above model (simulation plots and parameters are shown in Fig. 51, 53 and Table 19). There are several possible explanations for the large discrepancy especially at high applied voltages. At high applied voltages, much of the current can be converted into heat. The Joule heat leads to rise in the cell temperature, which is higher than the experimental setting of 500 °C, and can promote the NH_3 decomposition. Another possible explanation is that the excessive polarization gives rise to unstabilization of the Fe-N phase, which subsequently leads to a decrease in the rate of NH_3 production. Iron nitrides have a narrow range of compositions, in the Fe-N system,

Fe_4N coexists with α-Fe up to 592 °C, from 592 to 650 °C with γ-Fe and below 680 °C with ε-Fe, and Fe_2N only coexists with ε-Fe up to about 500 °C.[71] The N_2 dissociation rate constant may change with time during the phase transition of Fe, while the rate constant of N_2 dissociation in the above model was set at a constant value, which could result in the fitting disparities.

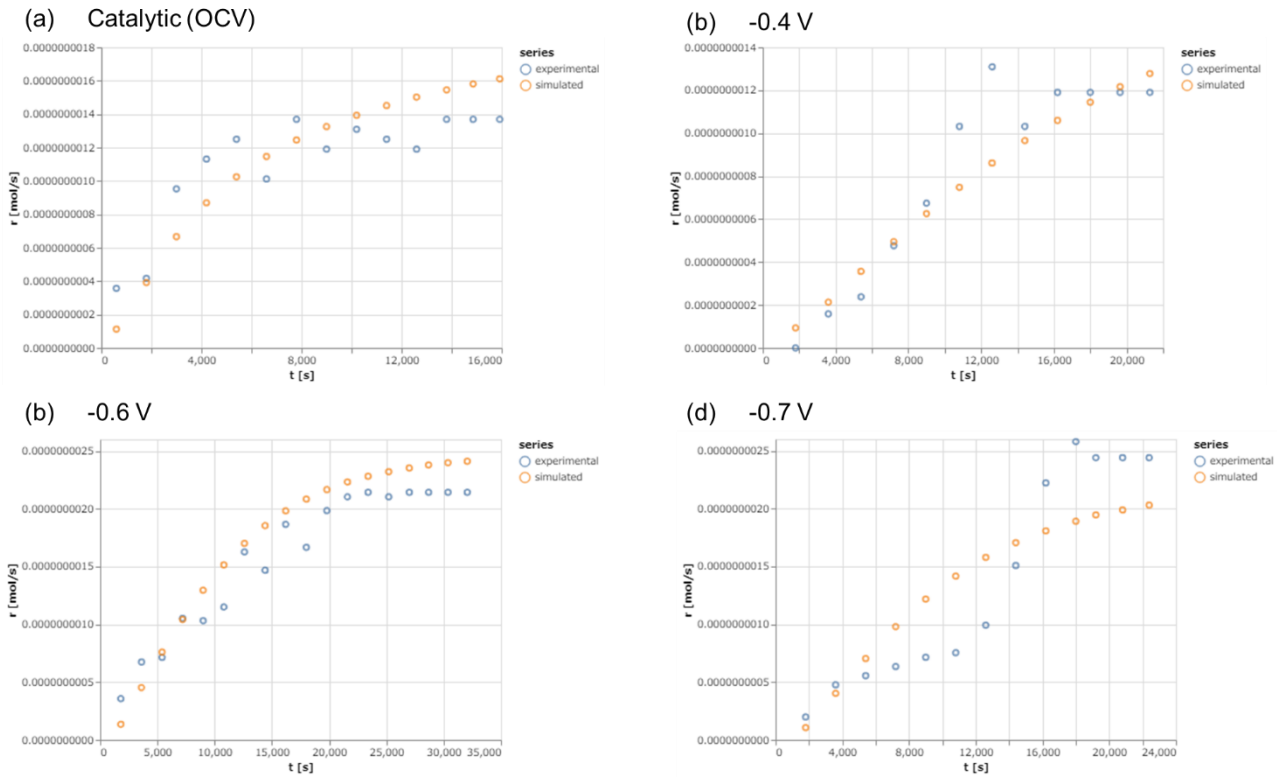

Figure 50 Fitting results (orange) and experimental (blue) plot at (a) catalytic, (b) -0.4 V, (c) -0.6 V, (d) -0.7 V based on the model suggested above.

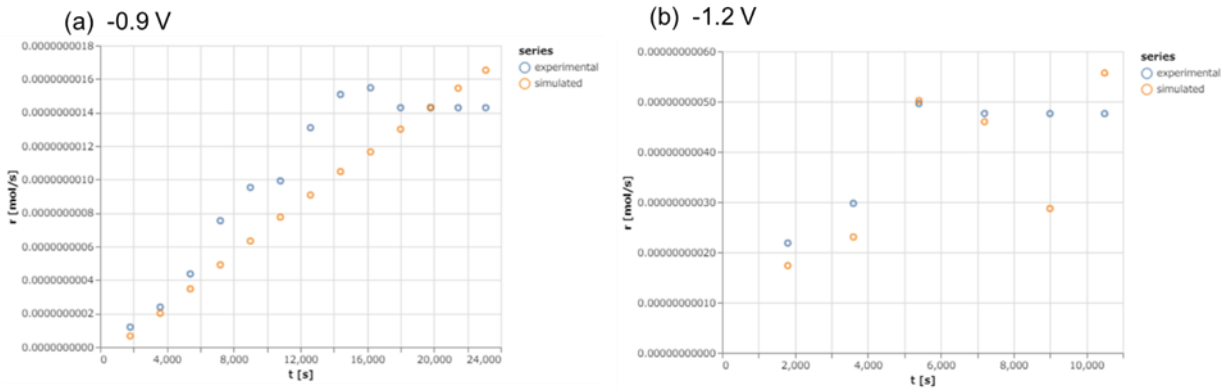

Figure 51 Experimental and simulation plots of NH_3 production rate against time at -0.9 V and -1.2 V. There are large discrepancies between simulation and experimental data at -0.9 V and -1.2 V.

Table 18 Parameters obtained by simulation at catalytic, -0.4 V, -0.6 V and -0.7 V.

	OCV	-0.4 V	-0.6 V	-0.7 V
$k_1 \times 10^{-7}$ [$mol^{-1}s^{-1}$]	784	3170	20.6	4.71
k_2 [$mol^{-3}s^{-1}$]	2.74	11.56	11.56	11.56
$k_3 \times 10^{5}$ [$mol^{-1}s^{-1}$]	9.20	-	-	-
k_{-3} [$mol^{-1}s^{-1}$]	1.28	1.21	1.21	1.21
$k_4 \times 10^{5}$ [$s\ mol^{-2}$]	-	9.71	9.71	9.71
$k_5 \times 10^{-8}$ [$s\ mol^{-2}$]	-	6.54	6.54	6.54
* total amount$\times 10^{-3}$ [mol]	301	3.20	3.20	3.20
V_H total amount [mol]	0.255	557	557	557
N* steady state$\times 10^{-3}$ [mol]	225	3.19	2.91	1.91
H_s steady state$\times 10^{-5}$ [mol]	25500	4.40	8.92	11.5
N* coverage steady state	74.7%	99.7%	90.9%	59.7%
H_s coverage steady state	100%	7.90×10^{-8}	1.60×10^{-7}	2.06×10^{-7}

Table 19 Parameters obtained by simulation at -0.9 V and 1.2 V with large fitting losses.

	-0.9 V	**-1.2 V**
k_1 **[mol^{-1}s^{-1}]**	6.13×10^{-8}	1.04×10^{-1}
k_2 **[mol^{-3}s^{-1}]**	9.46×10^{-1}	9.46×10^{-1}
k_3 **×10^5 [mol^{-1}s^{-1}]**	-	-
k_{-3} **[mol^{-1}s^{-1}]**	1.21	1.21
k_4 **×10^5 [s mol^{-2}]**	9.71	9.71
k_5**×10^{-8} [s mol^{-2}]**	6.54	6.54
*** total amount [mol]**	3.88×10^{-2}	3.88×10^{-2}
V_H total amount [mol]	1.71	1.71
N* steady state [mol]	3.83×10^{-2}	3.87×10^{-2}
H_s steady state [mol]	3.92×10^{-6}	1.85×10^{-6}

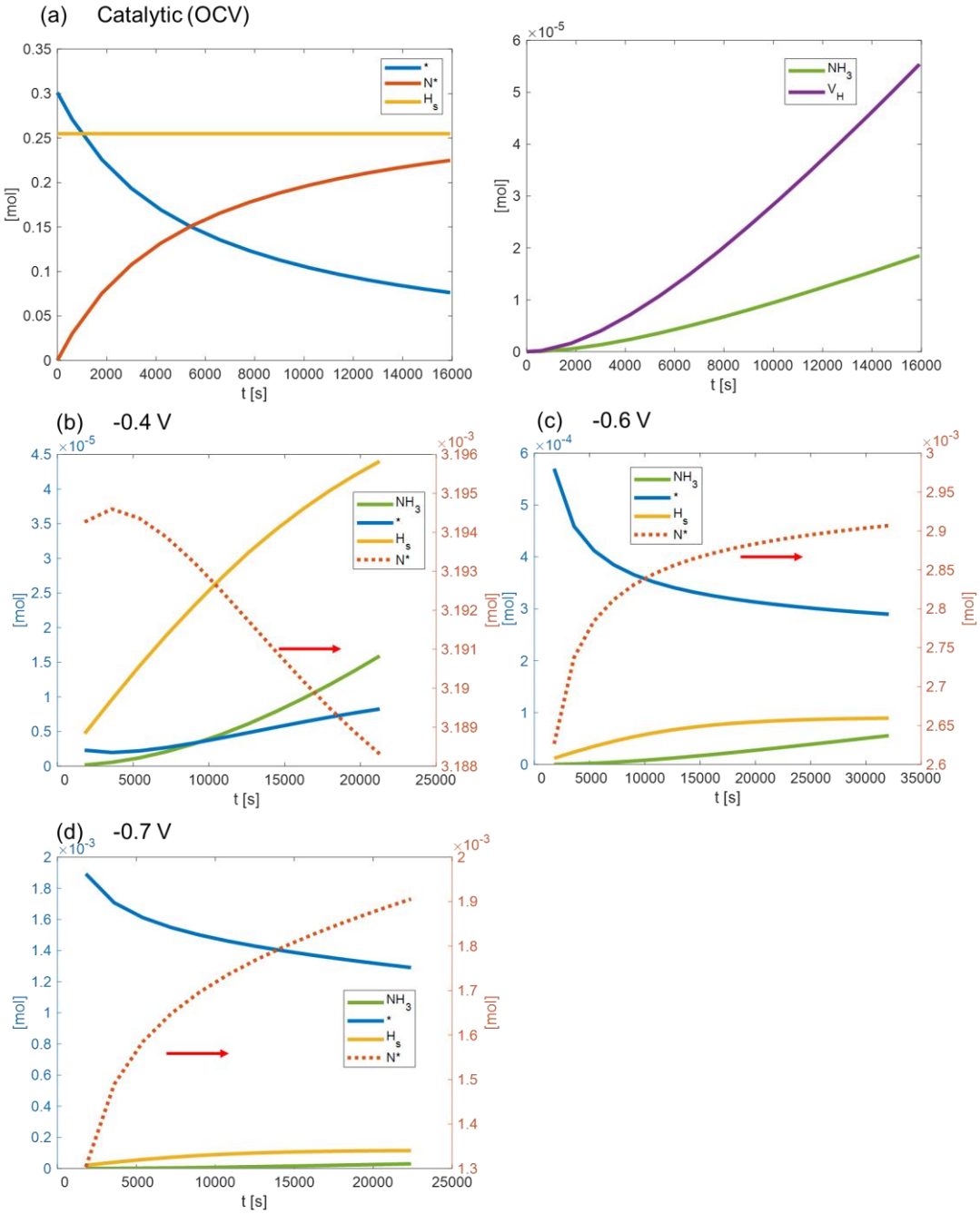

Figure 52 Plots of the amount of the species against reaction time at (a) catalytic, (b) -0.4 V, (c) -0.6 V, (d) -0.7 V. In (b), (c) and (d), NH_3 (green line), H_s (yellow line) and * (blue line) corresponds to left vertical axis. N* (dotted red line) corresponds to right vertical axis.

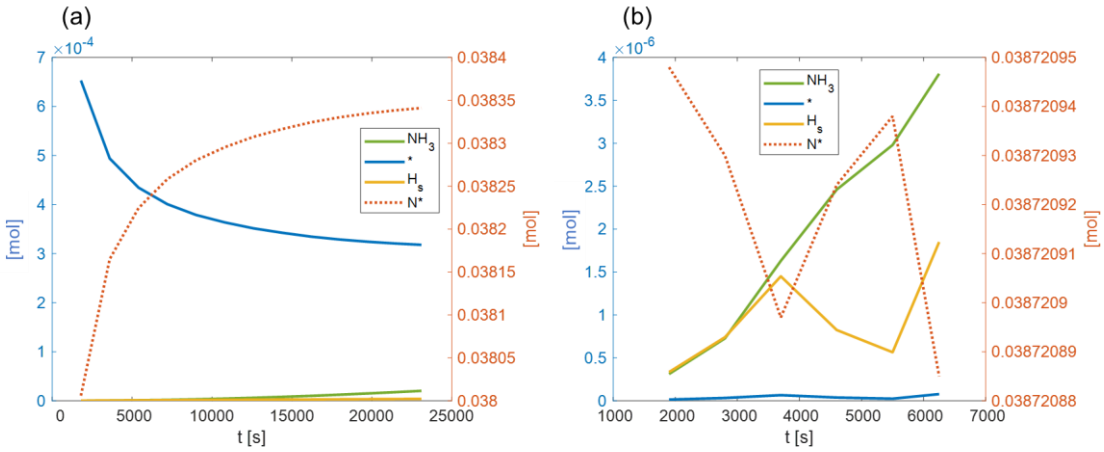

Figure 53 Plots of the amount of the species against reaction time at (a) -0.9 V, and (b) -1.2 V.

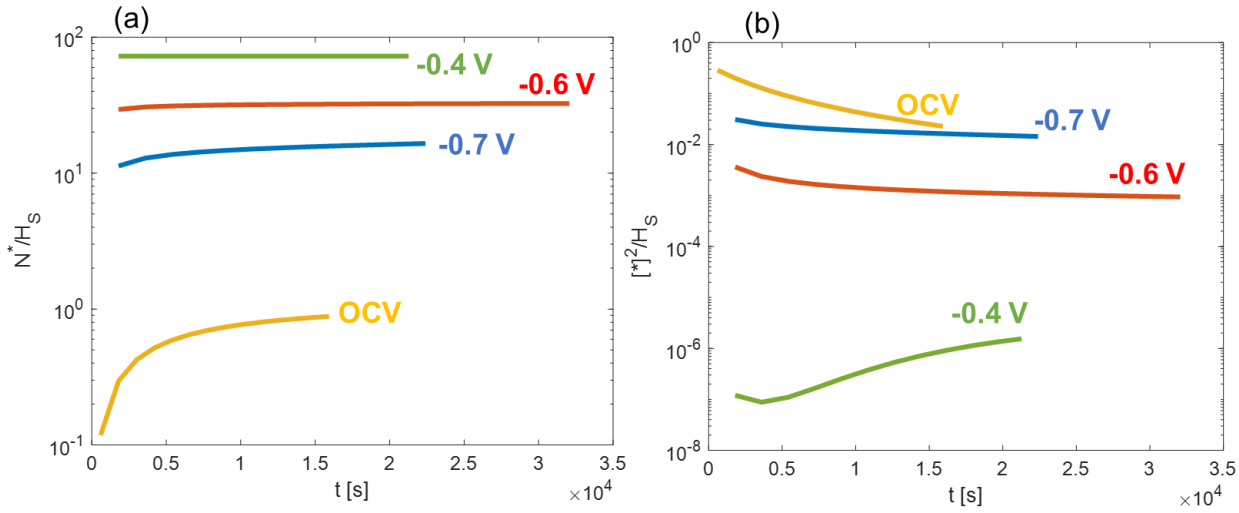

Figure 54 (a) Plot of ratio of adsorbed N (N*) to adsorbed H (Hs) against time. (b) Plot of [* (N active site)]^2/Hs at catalytic (yellow), -0.4 V (green), -0.6 V (red), -0.7 V (blue).

4.6 Summary and future improvements

In this work, an Fe-based catalyst, Fe/BZY, is used to synthesize NH_3 from N_2 and H_2 catalytically and electrochemically with a BZY electrolyte at ambient pressure and 500 °C. In the catalytic activity test, steady NH_3 production rate was 2.10×10^{-9} mol/(g-cat s). Electrochemical promotion was observed at applied voltages of -0.6 V, -0.7 V, and -0.9 V. The maximum steady NH_3 production rate of 3.07×10^{-9} mol/(cm^2 s) was yielded at -0.7 V, and the maximum enhancement factor Λ of 25.1% was achieved at -0.6 V. At highly negative applied voltages, Λ became negative. The observed electrochemical promotion of NH_3 production was explained by modelling the transient response of NH_3 production rate to the polarization. The fitting results designated that by applying voltages the amount of N* (adsorbed N atoms) on the electrode catalyst surface became considerably greater than that of H_s (adsorbed H atoms), and consequently the NH_3 production rate was accelerated. The NH_3 production rate response to the voltage application was slow, which could be accompanied with the phase transition of Fe in Fe/BZY by polarization. As Fe/BZY catalyst tends to be oxidized at high temperatures in oxidative conditions, electrocatalytic synthesis of NH_3 in two-chamber reactor using steam and N_2 at ambient pressure is the main target in the future.

The main contributions of this work can be summarized as follows.

(1) The maximum steady NH_3 production rate of 3.07×10^{-9} mol/(cm^2 s) was yielded at -0.7 V, and the maximum enhancement factor Λ of 25.1% was achieved at -0.6 V.

(2) The observed electrochemical promotion of NH_3 production was explained by modelling the transient response of NH_3 production rate to the polarization. As the results, when the amount of N* (adsorbed N atoms) on the electrode catalyst surface became considerably greater than that of H_s (adsorbed H atoms), it is favorable for NH_3 production.

The phase transition from α-Fe to γ-Fe might be a dominant reason for the slow response of NH_3 production rate at OCV and applied voltages. With the phase transition, the reaction rate constant of the N_2 dissociation reaction could be a function of time. Expressing the rate constant as a time function complicates the fitting by introducing too many parameters. For future research, in order to quantitatively determine the phase transition of Fe, the change in magnetism could be measured as the electrolysis reaction proceeds. Other methods of improving the modelling include the introduction of continuous NH_3 quantitative method.

Chapter 5: Diffuse reflectance infrared Fourier transform spectroscopy (DRIFTS) for the *in situ* analysis of adsorbed N-containing spices during electrolysis

Typical electrochemical characteristics of electrolysis cells such as impedance spectroscopy, current-voltage curve (IV curve) testing, cyclic voltammetry and the mentioned potentiostatic pulse experiment above, only provide indirectly information in a sense. In other words, adsorbed species on the electrode catalysts cannot be observed directly by these methods, which leads to the difficulty of mechanism study in some ways. In situ spectroscopy methods such as X-ray spectroscopy are developing and have already been applied to electrochemical devices and provide valuable information of the chemistry species during the reactions. *In situ* Diffuse reflectance infrared Fourier transform spectroscopy (DRIFTS) for electrolysis cells attracts much attention recently. For a sampling by DRIFTS, the infrared (IR) beam enters the sample, and then can be reflected or transmitted through the sample particles. The scattered IR beam is collected by the spherical focusing mirrors and finally analyzed. Samples are typically prepared as powers filled into the micro-cup in the metal base, or prepared as solutions dropped on a substrate and then evaporated.

5.1 Introduction of Fourier-transform infrared spectroscopy (FTIR)

Infrared spectroscopy (IR spectroscopy), is a measurement of the interaction between the infrared radiation and a liquid,[90] solid[91] or gaseous[92] substance by absorption, emission and reflection. A typical IR spectroscopy can be plotted on a vertical axis of absorbance or transmittance against the wave numbers with the symbol cm^{-1} on the horizontal axis. A N atoms system has 3N-3 degrees of freedom, in the case of a linear molecule, there are 2 rotational and 3N-5 vibrational degrees of freedom. For a nonlinear molecule, there are 3 rotational and 3N-6 vibrational degrees of freedom. A simple symmetrical diatomic molecule such as N_2 has only one vibrational degree and the vibrational band is not observed by IR spectrum. There are generally two kinds of vibrations, stretching and bending, depending on the changes of bond length and angle. Figure 56 shows six patterns of common vibrations in a CH_2 system. The schematic illustration of the stretching vibrations modeled by the harmonic oscillator model is Fig. 55 The chemical bond connecting two atoms or chemical groups A and B is approximated as a spring. The equation is given as:

$$v = \frac{1}{2\pi c}\sqrt{k\frac{m_A + m_B}{m_A m_B}}$$

v: frequency of vibration (cm^{-1})

c: speeds of light (cm/s)

k: bond strength (1×10^{-5} N/cm)

m_A, m_B: mass of A, B (g)

Based on the harmonic oscillator model, the stretching vibration frequency v depends on the bond strength and the atoms mass.[93] It can be seen that the stronger the chemical bond the higher the vibration frequency. Thus, the triple or double bonds have higher

vibration frequencies than the single bond typically. It is also known that the heavier the mass the lower the vibration frequency. Specific isotope labeling (^{2}H, ^{13}C, ^{15}N, ^{18}O) of one of the atoms involved in the vibration is possible to change the vibration frequency, and this method is widely used in small molecular such as N_2O[94] and complex groups such as proteins[95] for concentration measurement and structural analysis. The frequency is also sensitive to the environment such as hydrogen bonding interactions. Generally, hydrogen bonds lower the stretching vibration frequency but increase the bending vibration frequency.[96]

The infrared spectrum is usually divided into three regions, which are near-infrared, mid-infrared and far-infrared. The near-infrared (NIR) with high energy is approximately in the range of 14000-4000 cm^{-1}, the mid-infrared (MIR) is about 4000-400 cm^{-1}, and the low-energy far-infrared (FIR) is in the range of 400-10 cm^{-1}. Fourier-transformed infrared (FTIR) spectroscopy collects the vibrations over a wide spectral range, and then the raw data is transformed into spectrum by a Fourier transform. The measured reflectance and transmittance can be converted by

$$A = \log_{10} I_0/I_1$$

I is the transmittance or reflectance, and A is the absorbance.

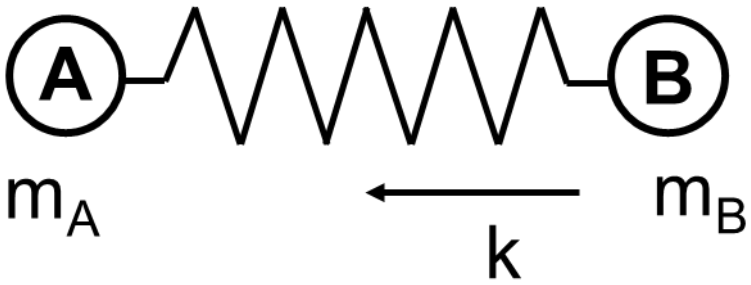

Figure 55 The stretching vibrations modeled by the harmonic oscillator model.

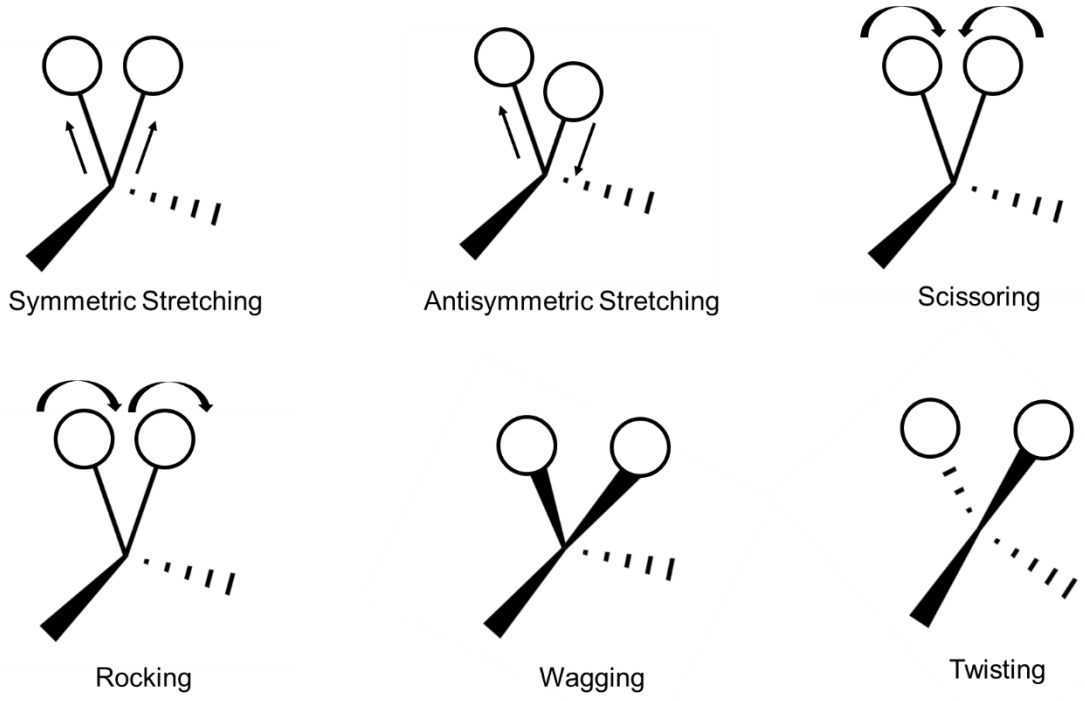

Figure 56 Six kinds of common vibration ways.

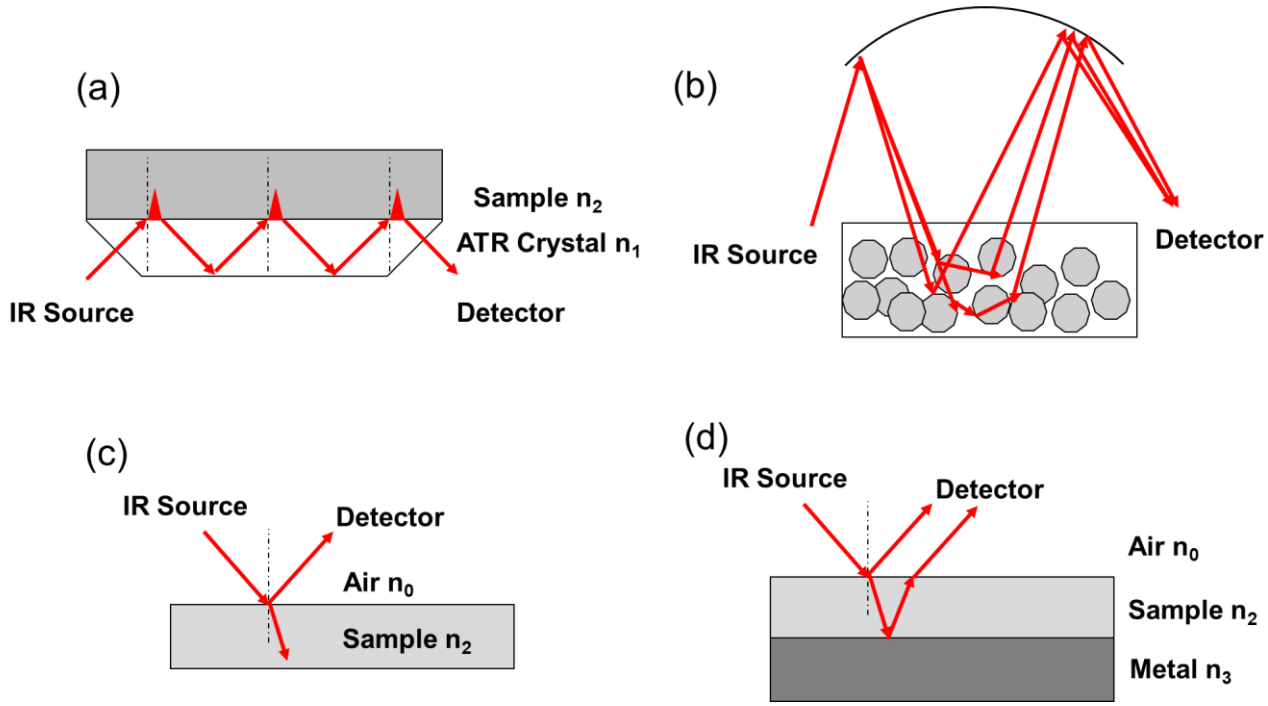

Figure 57 Reflectance methods in FTIR.[97] (a) Attenuated total reflectance (ATR). (b) Diffuse reflectance infrared Fourier transform spectroscopy (DRIFTS). (c) Specular reflection. (d) Reflection absorption method.

The following is a general introduction to the procedure for operating an FTIR. General introduction of the reflectance methods in FTIR are illustrated in Fig. 57. The first step is the sample preparation. Sample preparation differs depending on the reflectance method. In this work, DRIFTS was carried out, and samples are measured as they are, without mixing with KBr. The second step is getting a background spectrum. The background spectrum contains information on the source, interferometer, and detector, as well as on the ambient water and CO_2 present on the optical bench. Figure 58 shows a background spectrum example, the doublet peaks at 2360 cm^{-1} corresponds to asymmetric stretching of gaseous CO_2, and the peaks at 1600 cm^{-1} (O-H bending) and 3600 cm^{-1} (O-H stretching) corresponds to ambient water. The third step is the spectrum measurement

contains the absorption information from the samples as well as the background. From the ratio between the sample spectrum and the background spectrum $A = \log_{10} I_0/I_1$, the absorption information of the samples can be investigated clearly.

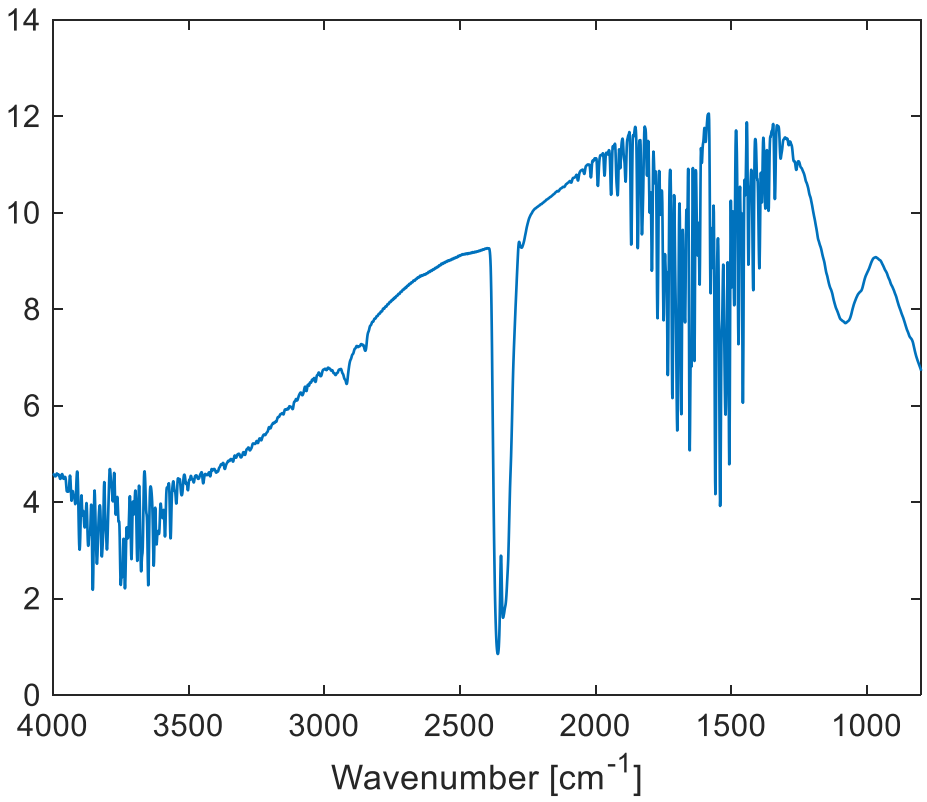

Figure 58 An example of an FTIR background.

5.2 Modified in situ DRIFTS setup

In this work, a commercial DRIFTS setup was modified and applied to electrochemical N_2 reduction as Fig. 59. In order to achieve an operation temperature higher than 200 °C which is desired for proton conductivity of the electrolyte (CDP in this chapter), an electrical resistance wire was placed in the metal base near the micro-cup. For protection of the ZnSe window from oxidation (must below 200 °C) at the high operating temperature, a water-cooling system was attached to the metal base near the dome. The specific size of the apparatus is shown in the Fig. 60. An O ring fits to the dome can ensure gas tight of small space in the dome. There are three pathways which connect the inside space of the dome and atmosphere. Two of them are used for the inlet and outlet gas flows, and the one connects with the micro-cup directly was used as the pathway for Pt lead wires. In order to avoid the shortage by the two Pt lead wires, a thin polyimide film (12.5 μm, Kapton, Wilmington, Delaware, United States, Dupont) which is stable from -269 - +400 °C. was used to cover the Pt wires.

Electrolysis cell was set on the micro-cup of the metal base. In the electrochemical synthesis process mentioned above in Chapter 3, a ⌀10 mm carbon paper was used on the cathode side in order to increase the current collection area. However, in the *in situ* DRIFTS tests, the cathode catalysts must be exposed to the IR beam, hence a carbon ring with an inside diameter of 7 mm was used instead as shown in Fig. 61. On the anode side, a ⌀10 mm Pt/C loaded on carbon paper was used for current collection. The electrolysis cell constitutes 0.1 g CDP electrolyte (mix ratio of SiP_2O_7:CsH_2PO_4 was 1:1) compressed with 0.035 g Fe/BZY-Ru (mix ratio of Fe/BZY : RuO_2 was 1:1) catalyst on the top layer. in order to fix the electrolysis cell, the current collection materials and the Pt lead wires, PTFE sheets formed into rings were used as support. Tests in the dome are actually similar

with tests in a single-chamber reactor, and the inlet gas is a mixture of N_2 and H_2, which is different from the above two-chamber reactor in electrolysis tests in this chapter. In the electrochemical synthesis process mentioned above in Chapter 4, a sintered BZY electrolyte has a diameter of about 16 mm, while due to the constrains of the small space of the dome, BZY powders were pressed into a ⌀10 mm pellet, and finally sintered to be a ⌀9 mm pellet. As shown in Fig. 62, a disk of 0.6 g Fe_2O_3/BZY was used as the cathode catalyst, and was attached to the electrolyte in the same way in Chapter 4. Since the heat tolerance temperature of the insulating used in modified DRIFTS setup is lower than 500 °C, the cell was pre-reduced in the single-chamber reactor before the *in situ* DRIFTS tests. A background absorbance spectrum was measured under the 8ml/min H_2 gas flow at 150 °C with 100 scans at OCV. All DRIFTS spectra are displayed as $\log(I_0/I)$ where I_0/I is the relative reflectance (I_0 is the background reflectance). Then the measurement procedure was shown in Fig. 63, measurements were carried out under the 8ml/min N_2 gas flow at 300 °C at OCV and under mixed N_2 and H_2 gas flow (both are 8 ml/min) at 250 °C at OCV and various applied bias.

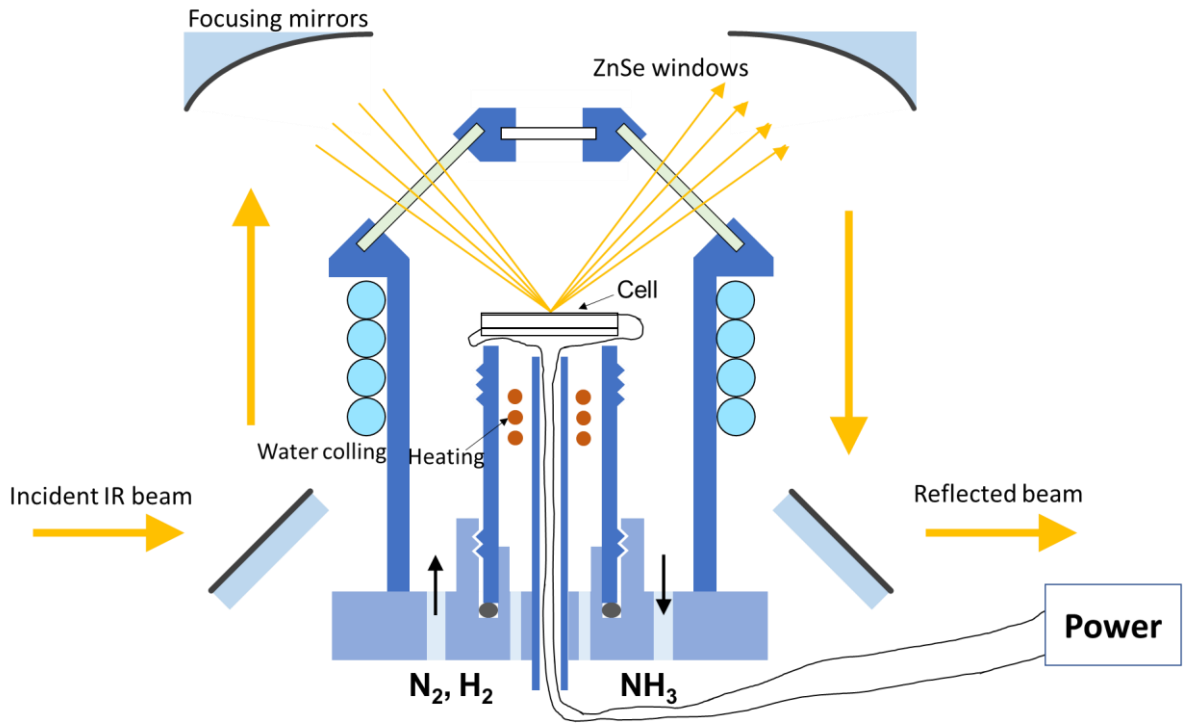

Figure 59 A schematic of modified DRIFTS setup applied to electrochemical N_2 reduction.

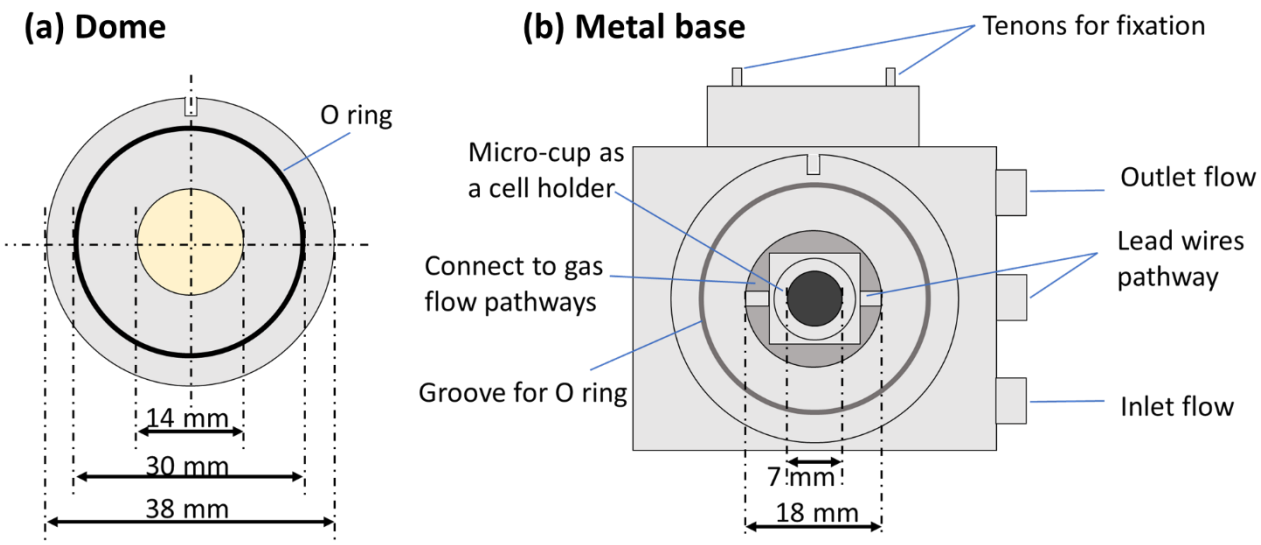

Figure 60 The bottom-up view of the dome (a) and the vertical view of the metal base (b).

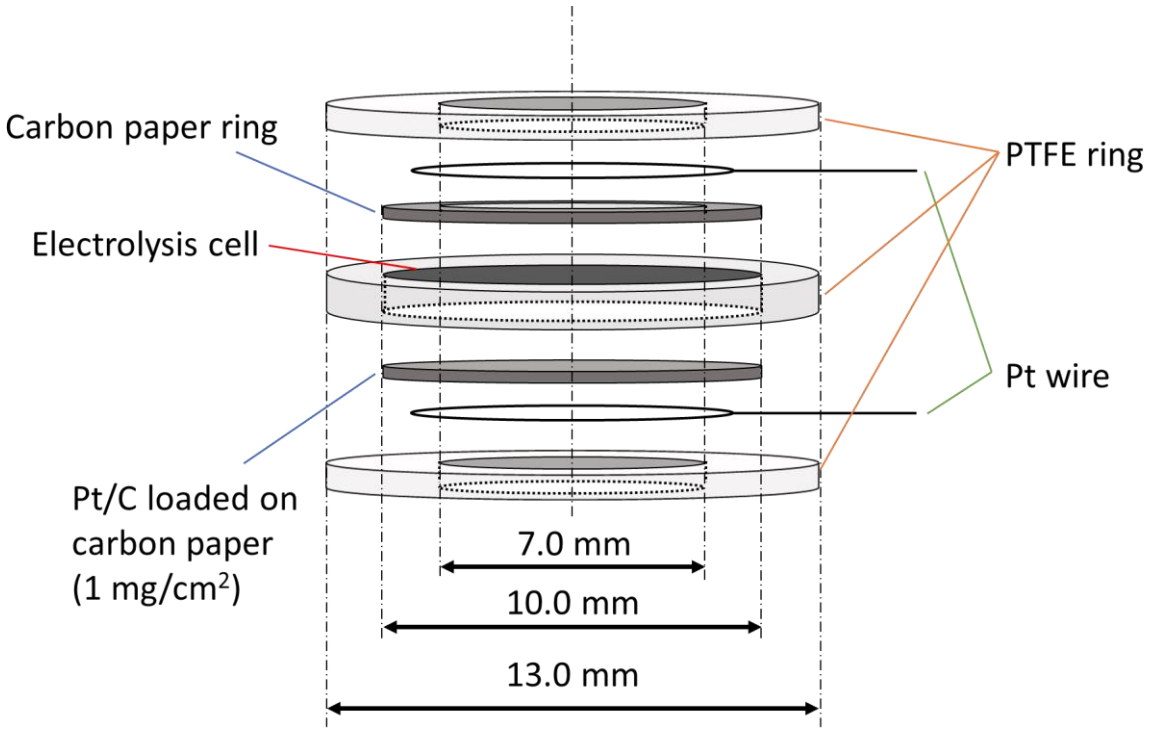

Figure 61 A schematic of electrolysis cell on the micro-cup. CDP electrolyte and Fe/BZY-Ru catalyst were applied.

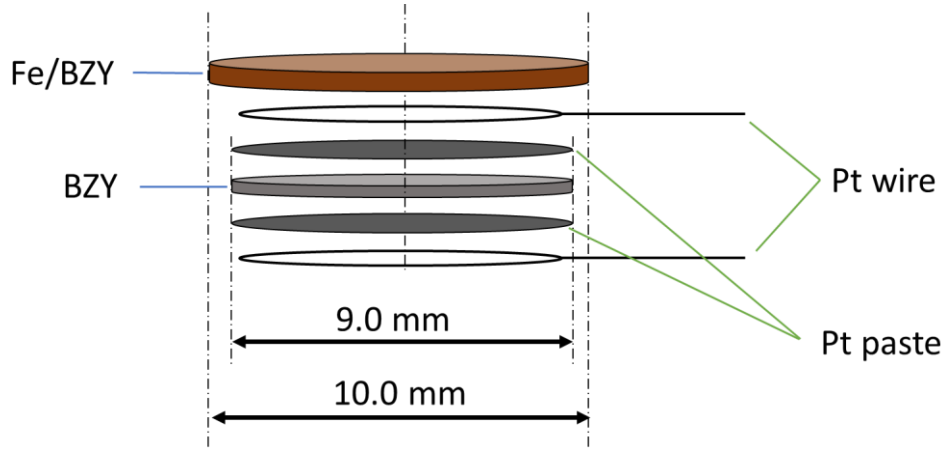

Figure 62 A schematic of electrolysis cell on the micro-cup. BZY electrolyte and Fe/BZY catalyst disk were applied.

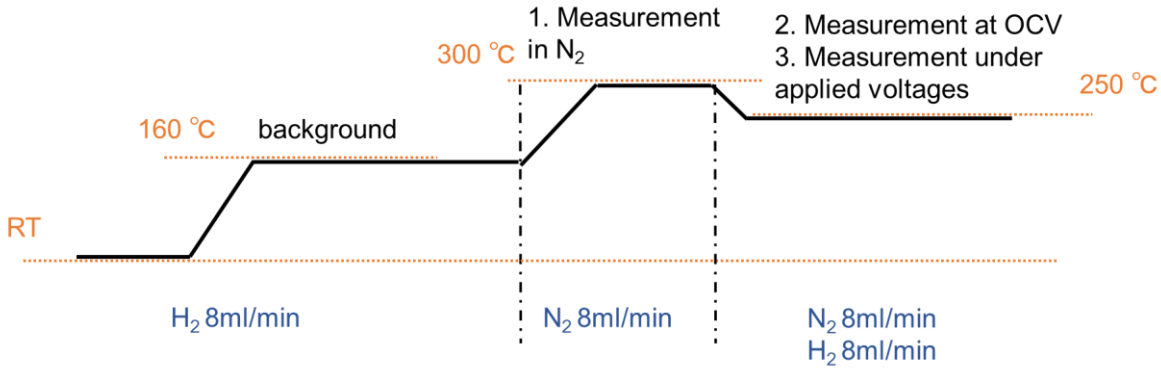

Figure 63 Measurement procedures for both CDP and BZY cell.

5.3 Results and discussion

According to the results of CDP cell in Figure 64, two kinds of sharp peaks at 1100 and 1301 cm^{-1}, one weak peak at 1461 cm^{-1}, and a broad peak at 3300 cm^{-1} were observed. Peak at 1100 cm^{-1} is attributed to N-N stretching (reported at 1106 cm^{-1}), which appeared in all experimental conditions even when only N_2 gas was supplied. This implies that the N_2 adsorption sites on the catalyst surface are highly active. Peaks at 1301 cm^{-1}, 1461 cm^{-1} and 3300 cm^{-1} are assigned to H-N-H wagging, H-N-H bending and N-H stretching of H-N-H bending (reported at 1270, 1461 and 3235 cm^{-1}).[98] These three kinds of peaks only appeared when both N_2 and H_2 are supplied and seems became stronger with applied bias. It is obvious that N_2H_x species were formed on the surface of Fe/BZY-Ru. In addition, the strong signal at 2360 cm^{-1} is associative with gas-phase CO_2 exists in IR beam path outside the dome. The complicated peaks at a wide range of 1500-1800 cm^{-1} are attributed to -OH species.[99]

According to the results of BZY cell in Figure 65, two broad peaks of N-N stretching at 1000-1300 cm^{-1} and N-H stretching at around 3300 cm^{-1} are only appeared at applied bias. Peaks at 1400-1800 cm^{-1} assigned to O-H bending and peak at 3600 cm^{-1} assigned to O-H stretching are much stronger than the results of CDP cell. It supports that with the protection of Ru by the spillover effect, Fe is suppressed from binding to oxygen species. As the voltage increased, strength of O-H bending and O-H stretching adsorption increased at first until -0.6 V and then decreased. Possibly it is because at higher applied voltage, -H species become the dominant adsorption species and would lead to lower NH_3 production rate and FE. It corresponds to the results in Chapter 4, and provides support for the reaction model assumption. As the applied voltage became larger, the N-H stretching peak shifted slightly to the right. The vibration frequency became lower, which

means the strength of N-H bond became weaker.

While differences of the reflections between OCV and with bias were observed, both CDP cell and BZY cell exhibited low extremely current densities. For CDP cell, reactant gases were taken into the system without humidification, which might lead to low proton conductivity and CDP decomposition. In addition, current collection area on the cathode side is much smaller than electrolysis process in Chapter 3. For BZY cell, since the heat tolerance temperature of the insulating used in modified DRIFTS setup is lower than 400 °C, where BZY exhibits low proton conductivity.

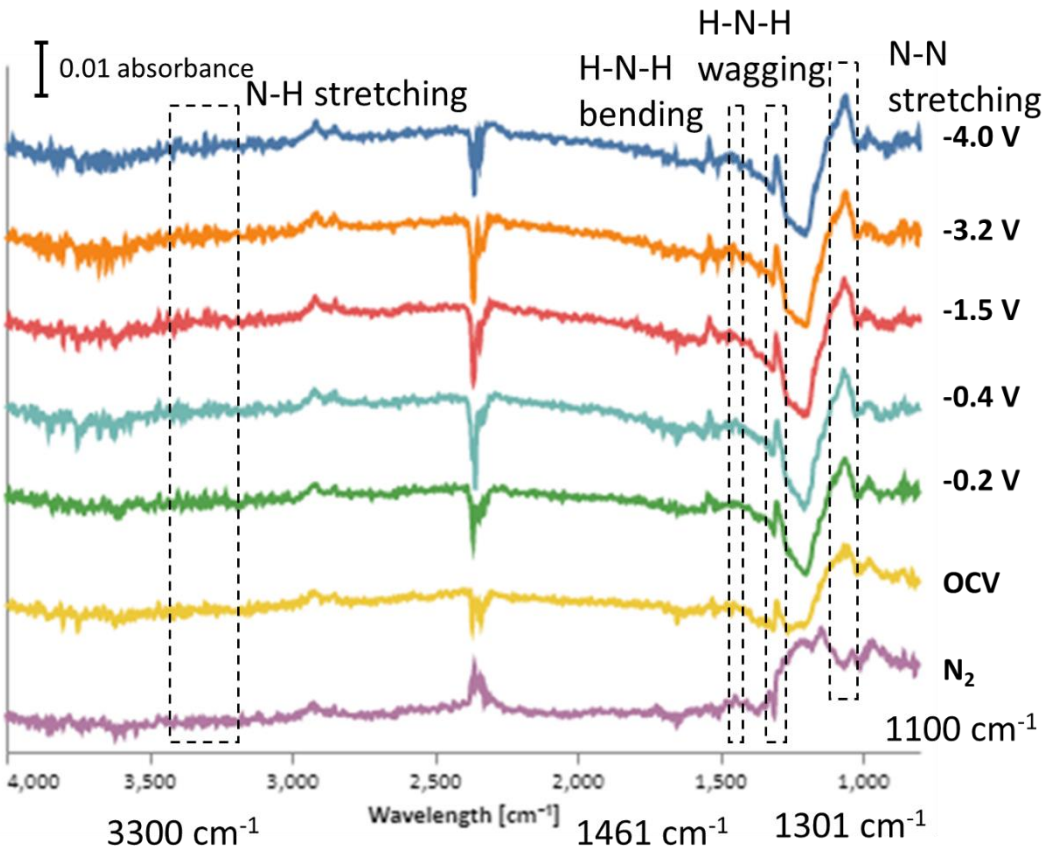

Figure 64 Spectra results of CDP cell with Fe/BZY-Ru cathode catalyst in N_2 flow of 8 ml/min and N_2-H_2 mixed flow (1 : 1) of 16 ml/min at various electrochemical potentials.

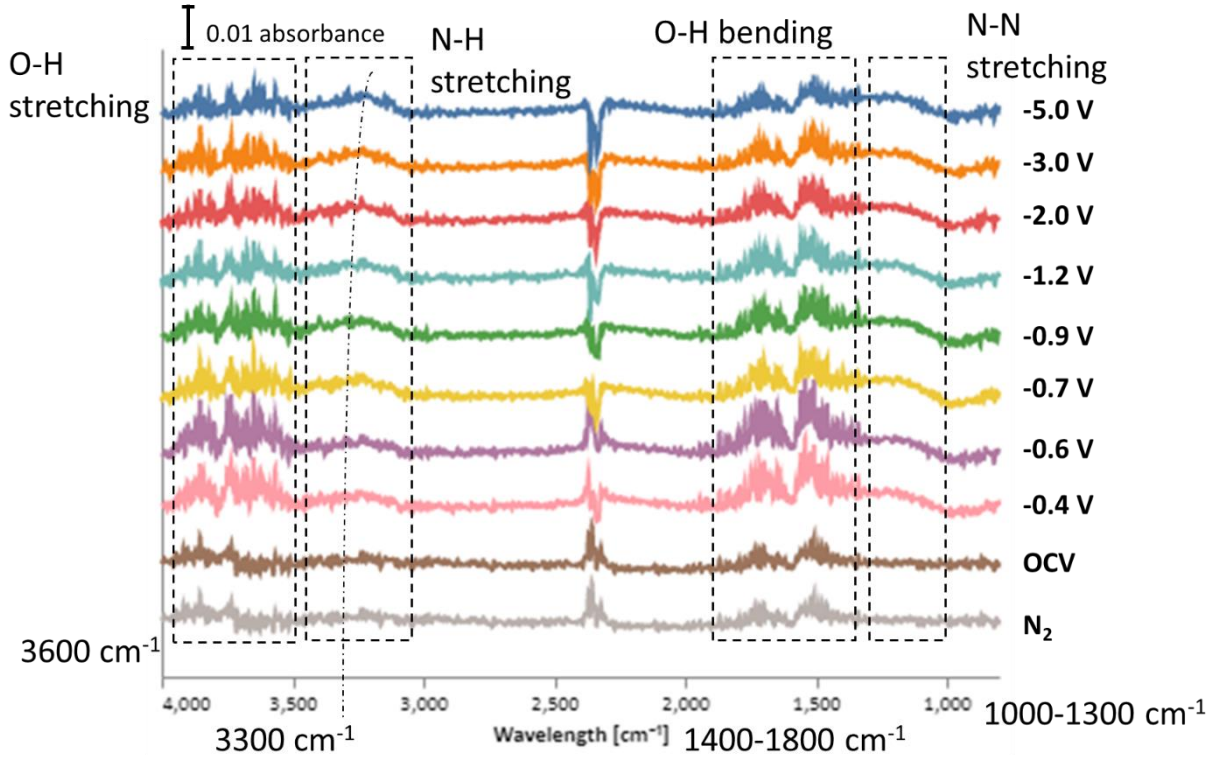

Figure 65 Spectra results of BZY cell with Fe/BZY cathode catalyst in N_2 flow of 8 ml/min and N_2-H_2 mixed flow (1 : 1) of 16 ml/min at various electrochemical potentials.

5.4 Summary and future improvement

In situ DRIFT measurements were carried out in a N_2-H_2 gas mixture with polarization, which is considered to be equivalent to a single-chamber reactor because the gas atmosphere in the DRIFT cell could not be separated. The materials of the samples were the same as the electrolysis cells in Chapters 3 and 4. The background was measured in H_2 flow, and the sample measurements were carried out in a mixed gas flow. In the obtained spectra, the peak at 1100 cm^{-1} was assigned to N-N stretching, and the peaks at 1301 cm^{-1}, 1461 cm^{-1} and 3300 cm^{-1} were assigned to -NH_2 wagging, H-N-H bending and N-H stretching. In the sample with CDP electrolyte, all the four kinds of these peaks mentioned above appeared, and there is an increase in the intensity of the peaks attributed NH_x with applied voltages. In contrast, in the sample with BZY electrolyte, the peaks of the N-containing adsorbed species were not as sharp as the sample with CDP electrolyte. The disadvantages of the set-up used in this chapter could be summarized as follows.

(1) Since the set-up is equivalent to a single-chamber reactor, humidified gas cannot be introduced into the equipment as Fe catalyst will be oxidized. Such low current in the electrolysis process could be caused by dehydration of the CDP electrolyte.

(2) The temperature setting was 300 °C, while in the case when H_2 was introduced, the temperature did not rise to 300 °C. The thermal conductivity of H_2 is high, suggesting that the heat loss resulted in a lower temperature.

The future work will modify the set-up to function as a double-chamber reactor illustrated in Figure 66. The anode chamber is inside the micro-cup, and the cathode chamber is outside the micro-cup. The anode side of the electrolysis cell will be covered the micro-cup and attached by gasket. H_2 and N_2 gas flow will be introduced separately. In this way, humidified gas could be introduced through the inlet flow way connected to the micro-cup, thereby preventing the contact of Fe catalyst with steam. H_2 inlet gas flow will be provided at a low flow rate; thus, the heat loss could decrease.

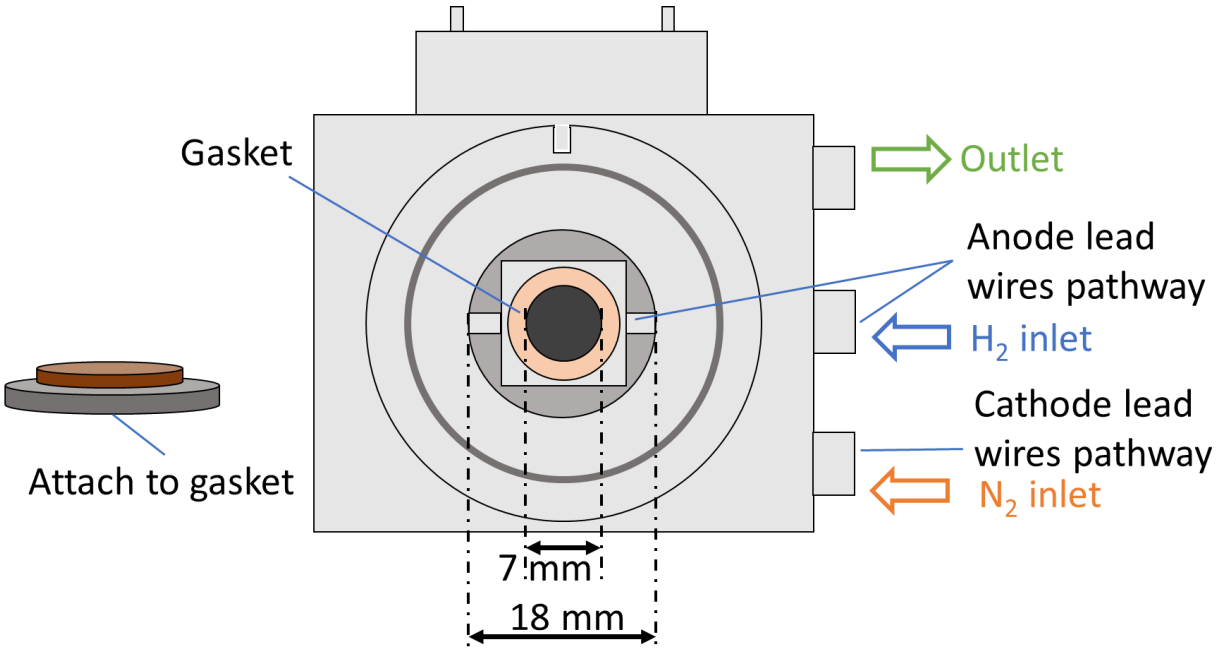

Figure 66 Design of the metal base to function as a double-chamber reactor.

Chapter 6: Conclusions

6.1 Summary

[Chapter 2] In this study, an Fe-based nitrogen reduction catalyst was developed and used in two different electrolytic reactors for the electrochemical reduction of nitrogen. The prepared catalysts have high catalytic activity, and the addition of Ru can prevent Fe from oxidation, thus enhancing the durability of the catalyst.

[Chapter 3] In the two-chamber reactor with phosphate electrolyte, the electrochemical reduction of nitrogen is considered to have proceeded via an associative mechanism. To verify the reaction mechanism, the data obtained by potentiostatic pulse experiment was analyzed with the proposed model. At the applied voltage of -0.2 V, adsorbed N_xH was harder to decompose than under other conditions, which can be the key to the formation of N_2H_4.

[Chapter 4] In the single-chamber reactor with BZY electrolyte, the electrochemical promotion effect was observed. A gradually increase in the reaction rate with the progress of the reaction time and a final stable change were fitted with the proposed model. As the result, large N^*/H_s benefited NH_3 production. However, when N^*/H_s was too large, it is not favorable to produce NH_3.

[Chapter 5] The *in situ* DRIFT measurements were carried out under conditions corresponding to the electrolytic process in order to directly observe the nitrogen-containing adsorbed species. The H-N-H bending peaks were only observed in the CDP cell with applied voltages.

Although NH_3 electrosynthesis has many challenges to overcome before it can be commercialized, the results of this study have shown that increasing the coverage of N-containing compounds on the cathode surface can improve ammonia selectivity and

increase the efficiency of nitrogen synthesis. However, with the guidance provided by this research, such as the improvement of ammonia selectivity by increasing the coverage of nitrogen-containing compounds on the cathode surface, the promotion of an efficient nitrogen electroreduction mechanism, and the increased durability of Fe-based electrocatalysts, it is necessary to work towards the solution of problems such as the improvement of the variability for the use of renewable energy.

6.2 Future perspective

6.2.1 Outlook on the future of industrial NH_3 synthesis

The outlook on the future of industrial synthesis of NH_3 is illustrated in Fig. 67. The short-term goal is to replace the hydrogen source of CH_4 in traditional Haber-Bosch process with syngas produced from biomass, or H_2 produced from water electrolysis. In the long term, it will gradually develop into a carbon-free method, such as the production of NH_3 by electrochemical synthesis directly from H_2 or water and N_2 or air.

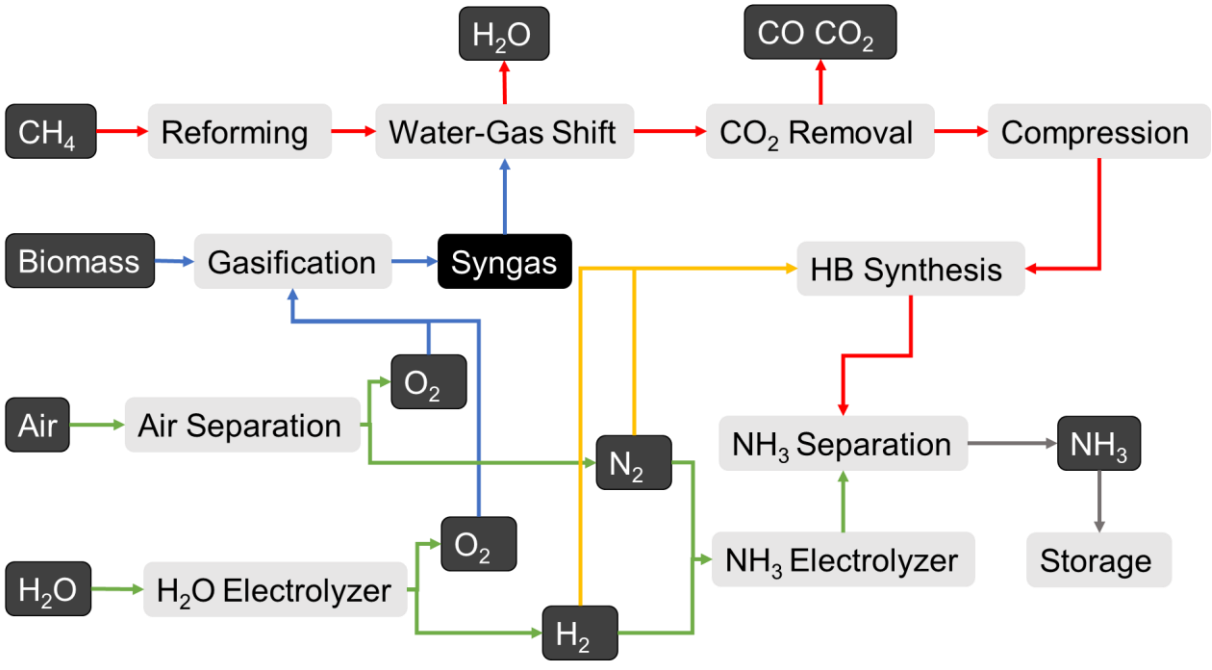

Figure 67 Schematic of present-day Haber-Bosch process and future green NH_3 synthesis process.

6.2.2 Ammonia-fed fuel cell

At present, over 80% of the 200 million tons of NH_3 produced annually worldwide is used to produce fertilizers and the rest in pharmaceuticals, explosives, and other chemical industries, but due to the high hydrogen content (17.6 wt%) and energy density (4250 kWh/m^3, liquid), it is a promising carbon-free energy carrier. H_2 has a high energy content per unit of mass (39.4 kWh/kg) and is used in fuel cells. However, the volumetric density of H_2 at ambient condition (0.089 kg/m^3) is low and the storage of liquid H_2 requires high pressure (with gas cylinders could up to 80 MPa) or low temperature (in cryogenic tanks at 21.2 K). Even under these severe conditions, the energy density of liquid H_2 per unit of volume is still much lower than the fossil fuels (such as coal and oil). While NH_3 can be easily liquefied thus is one of the most promising safe carbon-free transportation fuels. The energy contents of NH_3 and H_2 are summarized in Table 20.

Table 20 Comparison of the energy contents of NH_3 and H_2.[100] [101] [102]

	NH_3	H_2
Liquefaction temperature [K]	241.15	20.15
Energy density [kWh/kg]	6.25	39.4
Energy density liquid [kWh/m^3]	4250	1418 (80 MPa)
		2790 (21.2 K)

Direct NH_3 fuel cells have been already tested on alkaline membrane fuel cells (AMFCs) at low temperature,[103] alkaline fuel cells (AFCs) at intermediate temperature[104] and solid oxides fuel cells (SOFCs) at high temperature.[105] In the cases of AMFCs and AFCs,

which are operated by the transfer of the hydroxide ions (OH^-) through the electrolyte, the reactions are given by:

$$O_2 + 2H_2O + 4e^- \rightarrow 4OH^- \quad \text{Cathode eq. 1}$$

$$NH_3 + 6OH^- \rightarrow N_2 + 6H_2O + 6e^- \quad \text{Anode eq. 2}$$

Degradation of electrolyte performance due to the reaction between OH^- and CO_2 to CO_3^{2-} is a great challenge for AFCs. Direct NH_3 AMFCs can prevent the generation of carbonate precipitates thus increase the stability of the cells. Whereas it is hard to break the N-H bonds in NH_3 at low temperature. Proton-conducting acidic electrolyte operated at intermediate is not suitable for direct NH_3 fuel cells due to the reaction between acid and NH_3.

In the case of SOFCs, both oxygen-conducting and proton-conducting electrolytes were used for direct NH_3 fuel cells.[106] The reactions operated by oxygen conductors are given by:[107]

$$O_2 + 4e^- \rightarrow 2O^{2-} \quad \text{Cathode eq. 3}$$

$$NH_3 + 5O^{2-} \rightarrow 2NO + 3H_2O + 10e^- \quad \text{Anode eq. 4}$$

$$NH_3 + 3NO \rightarrow 5/2N_2 + 3H_2O \quad \text{Anode eq. 5}$$

The reactions operated by proton conductors are given by[108]:

$$2NH_3 \rightarrow N_2 + 3H_2 \quad \text{Cathode eq. 6}$$

$$H_2 \rightarrow 2H^+ + 2e^- \quad \text{Cathode eq. 7}$$

$$O_2 + 4e^- + 4H^+ \rightarrow 2H_2O \quad \text{Anode eq. 8}$$

For oxygen-conducting SOFC with electrolytes such as yttria-stabilized zirconate (YSZ) and samarium-doped ceria (SDC), the production of NO is one of the challenges, in addition, water produced on the cathode side cause the dilution of the fuel. Proton-conducting SOFCs use such as doped- barium cerate can cover the above two points, the

durability of anode at high temperature is a challenge.[109]

Direct N_2H_4 fuel cells are also attracting attention as a carbon-free energy source with a higher theoretical cell voltage of +1.61 V than direct NH_3 fuel cells (+1.17 V).[100]

Besides the mentioned challenges, both NH_3 and N_2H_4 are toxic, where safety concerns are remained for future application.

6.2.3 NH_3 combustion for power generation

In order to achieve decarbonization, the use of NH_3 as an alternative fuel for power generation is attracting a lot of attention. The Ministry of Economy, Trade and Industry (METI) has set a short-term target to 2030 of the introductions of 20% NH_3 mixed combustion in thermal power generation, and a long-term target to 2050 of improvement of the NH_3 mixed combustion rate up to 50%.[110] However, NH_3 combustion has several disadvantages.

(1) The minimum ignition energy of NH_3 is high. The minimum ignition energy (MIE) is the minimum amount of energy required to ignite a combustible vapor, gas, or dust. the reported MIE of NH_3 was 680 mJ, which is far greater than hydrocarbons of below 0.5 mJ.[111]

(2) The flammability limit of NH_3 is narrow. It is reported that the flammability of NH_3 is in the range of 15.5% to 27% by volume in air.[112]

(3) The burning velocity of NH_3 is low.[113] In order to improve the stability of the NH_3 combustion, other energetic fuels such as CH_4, H_2 were added.[114]

(4) High toxic NO_x emission during the NH_3 combustion. The proposed chemical reaction paths are shown in Fig. 68 Experimental studies have shown that under fuel-rich

conditions, NO_x emissions can be significantly reduced.[115]

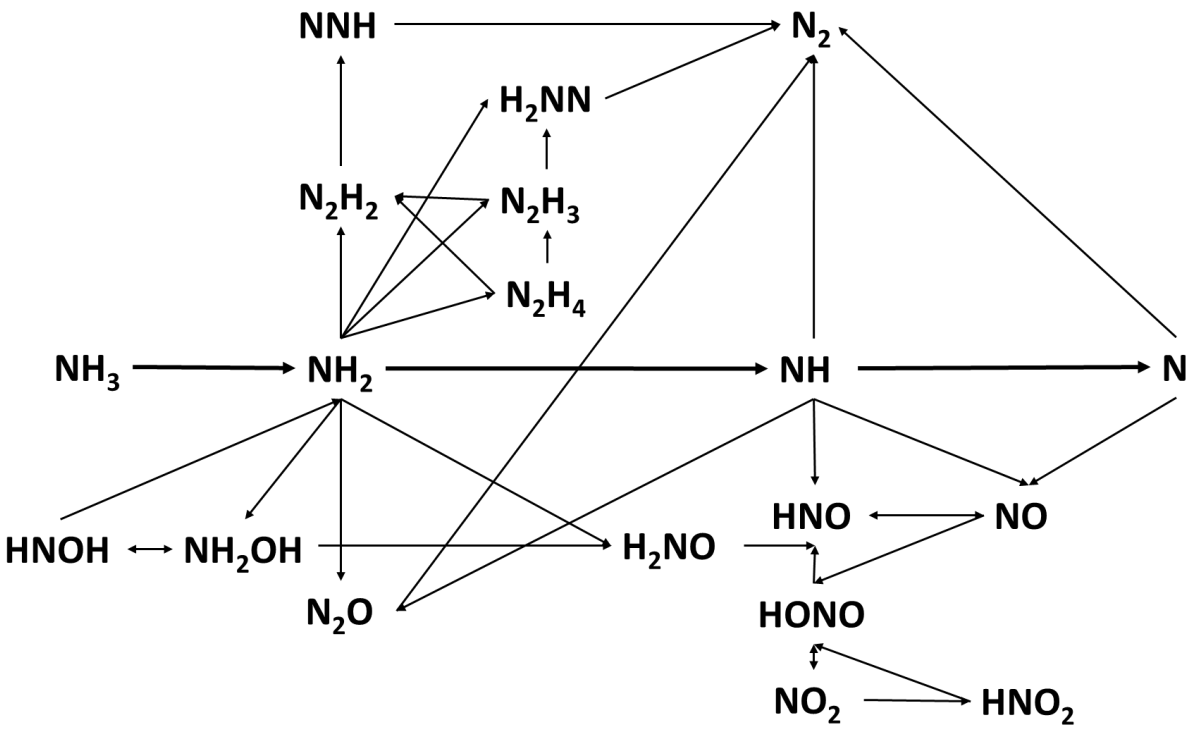

Figure 68 Proposed reaction paths for NH_3 combustion in NH_3/O_2 flames.[116] [117]

Appendix

A.1 Temperature dependence of standard enthalpy of formation ($\Delta_f H^\circ$) and standard entropy (S°)

Standard enthalpy of formation of a compound is the change in enthalpy when one mole of a substance is formed from its constituent elements with all substances in a standard state.[118] For a gas phase, gaseous NH_3 formation reaction from H_2 and N_2 in this study, it is assumed to be an ideal gas, and is the state of gas of pure substance at standard pressure p°. The standard pressure was recommended to be 10^5 Pa by IUPAC in 1982.[119] The standard enthalpy change can be calculated from the difference between the standard enthalpy of formation of products and reactants based on the Hess's Law, which is given by:

$$\Delta_r H^\circ = \sum \Delta_f H^\circ (products) - \sum \Delta_f H^\circ (reactants)$$

Since the standard formation enthalpy is a function of temperature and data at 298.15 K are all given, standard formation enthalpy at other temperature can be expressed as:

$$\Delta_f H^\circ(T) = \Delta_f H^\circ(298.15\ K) + \int_{298.15\ K}^{T} Cp^\circ dT$$

Thus, the standard enthalpy change can be given as:

$$\Delta_r H^\circ(T) = \Delta_r H^\circ(298.15\ K) + \sum \int_{298.15\ K}^{T} Cp^\circ dT\,(products) - \sum \int_{298.15\ K}^{T} Cp^\circ dT(reactants)$$

And the standard entropy can be given as:

$$S^\circ(T) = S^\circ(298.15\ K) + \int_{298.15\ K}^{T} \frac{Cp^\circ}{T} dT$$

Relations between the standard enthalpy change and the equilibrium constant (K) can be expressed by the van't Hoff equation:

$$\left(\frac{\partial lnK}{\partial T}\right)_p = \frac{\Delta_r H^\circ}{RT^2}$$

The relationship among the standard Gibbs energy ($\Delta G^\circ(T)$), the standard enthalpy, the standard entropy and equilibrium constant is given as:

$$\Delta G^\circ(T) = \Delta H^\circ(T) - T\Delta S^\circ(T) = -RTlnK(T)$$

The specific heat capacity at constant pressure ($c_p° \ J/(mol\ K)$) formed as a polynomial over temperature given by Shomate equation is written as:[120]

$$c_p° = A + Bt + Ct^2 + Dt^3 + E/t^2$$

t = temperature(K)/1000

In the gaseous NH_3 formation reaction

$$N_2(g) + 3H_2(g) \leftrightarrow 2NH_3(g)$$

$$\Delta_r H^\circ(T) = \Delta_r H^\circ(298.15\ K) + 2\int_{298.15\ K}^{T} c_p°\mathrm{NH_3} dT - \int_{298.15\ K}^{T} c_p°\mathrm{N_2} dT - 3\int_{298.15\ K}^{T} c_p°\mathrm{H_2} dT$$

$$K = \frac{\left(\frac{p\mathrm{NH_3}}{p^\circ}\right)^2}{\left(\frac{p\mathrm{N_2}}{p^\circ}\right)\left(\frac{p\mathrm{H_2}}{p^\circ}\right)^3}$$

The gas phase thermochemistry data of H_2, N_2 and NH_3 are from NIST (National Institute of Standards and Technology, U.S. Department of Commerce) Chemistry WebBook.

Table-A 1 Coefficients in Shomate equation for $c_p°$ calculation.

Species (g)	A	B	C	D	E
NH_3	19.99563	49.77119	-15.37599	1.921168	0.189174
H_2	33.066178	-11.363417	11.432816	-2.772874	-0.158558
N_2(100-500K)	28.98641	1.853978	-9.647459	16.63537	0.000117

N_2(500-2000K)	19.50583	19.88705	-8.598535	1.369784	0.527601

Table-A 2 Standard enthalpy of formation and standard entropy at 298.15 K

Species (g)	$\Delta_f H^\circ\ [kJ/mol]$	$S^\circ\ [J/(mol\ K)]$
NH_3	-45.90	192.77
H_2	0	130.68
N_2	0	191.61

The formation of NH_3 is an exothermic reaction ($\Delta_r H^\circ(T) < 0$) under the calculated temperature range (from 298.15 K to 800 K) in Figure-A 1. The standard Gibbs energy against temperature is plotted in Figure-A 2. The equilibrium constant decreases dramatically with the increase of temperature in Figure-A 3. At 298.15 K, the equilibrium constant is 5.43×10^5, while at 493.15 K (220 °C) it drops to 2.39×10^{-1}, and at 773.15 K (500 °C), the equilibrium constant is only 7.17×10^{-5}.

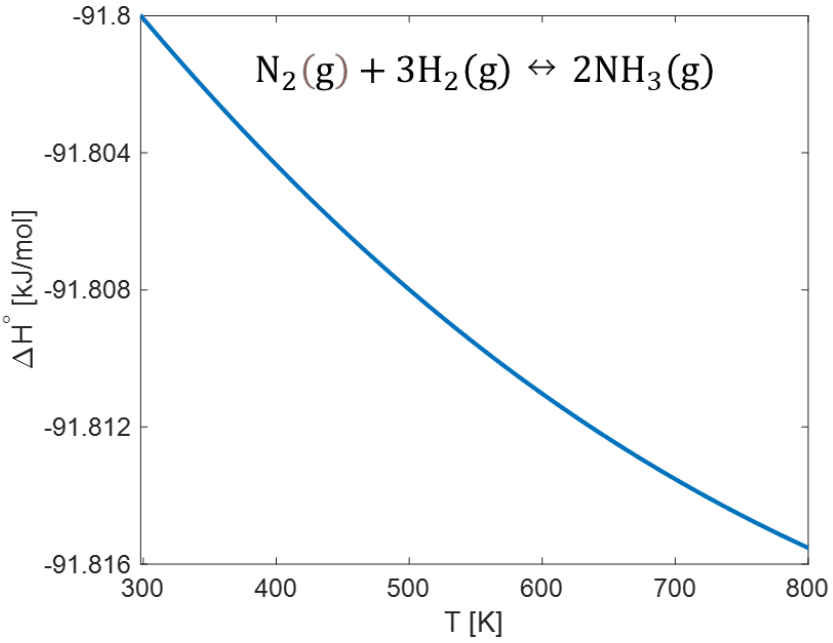

Figure-A 1 The standard enthalpy changes for NH_3 formation reaction.

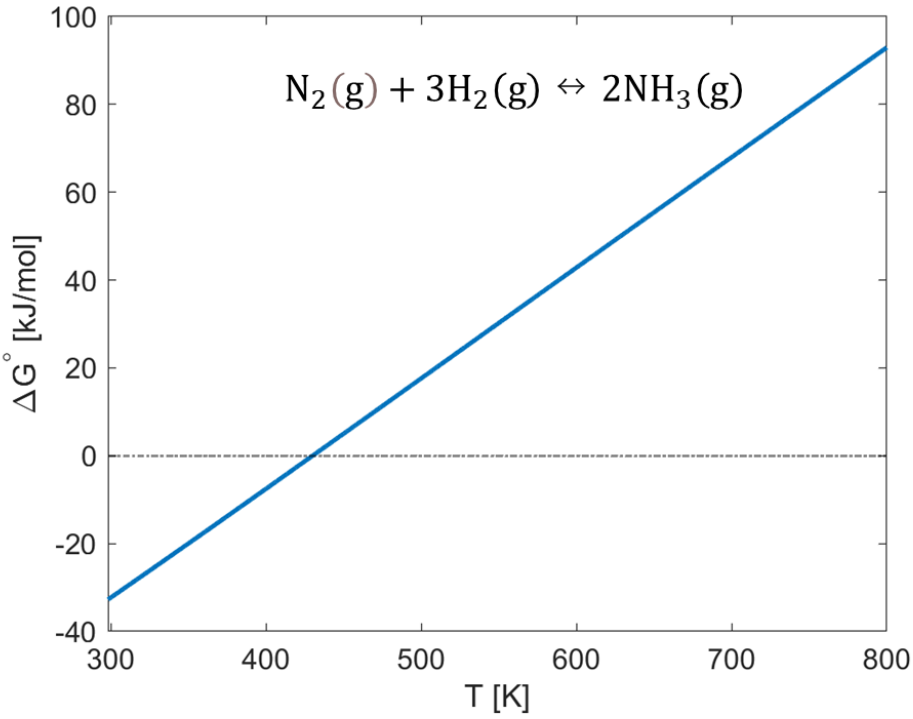

Figure-A 2 The standard Gibbs energy for NH_3 formation reaction.

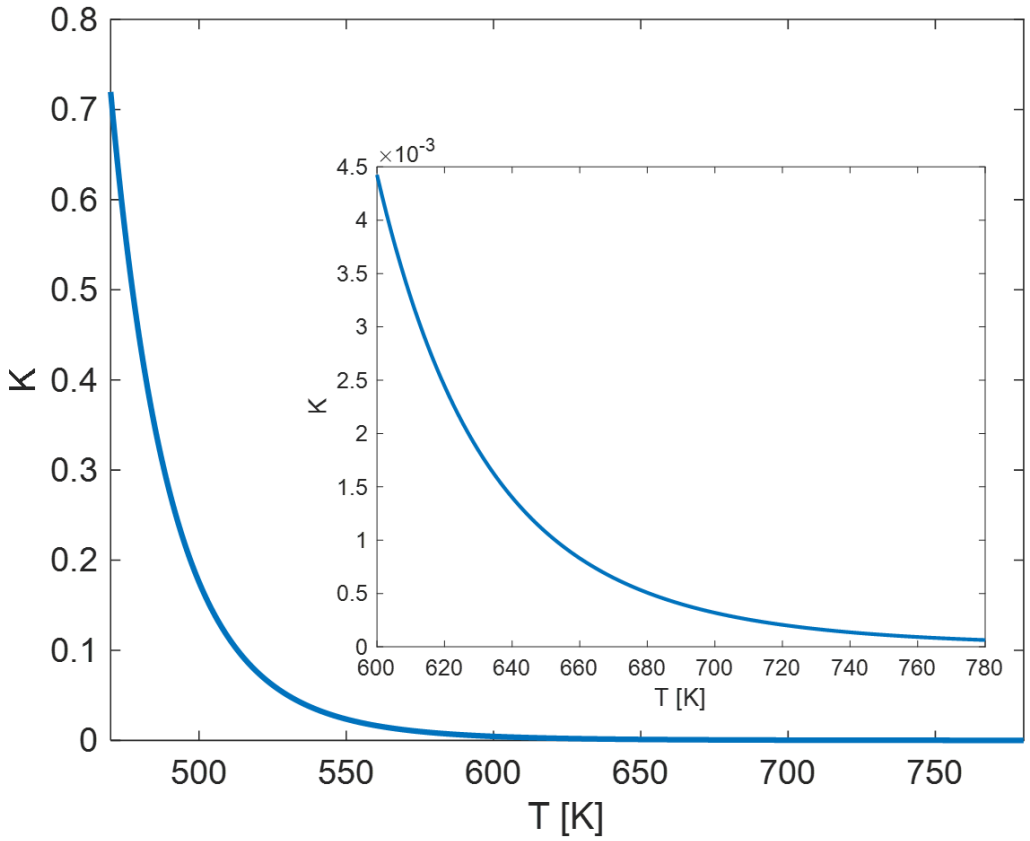

Figure-A 3 Calculated equilibrium constant at different temperatures.

With the obtained K, and equation relating the N_2 conversion rate to the N_2 fraction is given by following calculations.

$$\mathrm{N_2(g) + 3H_2(g) \rightleftharpoons 2NH_3(g)}$$

Before reaction:

$$T(inlet) = \mathrm{N_2}(inlet) + \mathrm{H_2}(inlet)$$

$$\mathrm{N_2}(inlet) = T(inlet) \times x(\mathrm{N_2}\ fraction)$$

$$\mathrm{H_2}(inlet) = T(inlet) \times (1 - x)$$

In equilibrium:

$$\mathrm{NH_3}(eq) = \mathrm{N_2}(inlet) \times y(conversion) \times 2 = T(inlet) \times x \times y \times 2$$

$$\mathrm{N_2}(eq) = \mathrm{N_2}(inlet) \times (1 - y) = T(inlet) \times x \times (1 - y)$$

$$\mathrm{H_2}(eq) = \mathrm{H_2}(inlet) - \frac{3}{2} \times \mathrm{NH_3}(eq) = T(inlet) \times (1 - x) - 3 \times T(inlet) \times x \times y$$

$$T(eq) = \mathrm{N_2}(eq) + \mathrm{H_2}(eq) + \mathrm{NH_3}(eq)$$

$$\frac{\left(\frac{p\mathrm{NH_3}}{p^\circ}\right)^2}{\left(\frac{p\mathrm{N_2}}{p^\circ}\right)\left(\frac{p\mathrm{H_2}}{p^\circ}\right)^3} = \frac{(\mathrm{NH_3}(eq)/T(eq))^2}{(\mathrm{N_2}(eq)/T(eq))(\mathrm{H_2}(eq)/T(eq))^3} \frac{2^2 \times y^2 \times \left(\frac{1}{x} - 2y\right)^2}{(1 - y) \times \left(\frac{1}{x} - 1 - 3y\right)^3} = K$$

Figure-A 4 shows the N_2 conversion plotted against $N_2/(N_2+H_2)$ under different temperatures. From Figure-A 5, when the N_2 fraction is very low, the conversion rate increases quickly. When the N_2 fraction is very high, the conversion rate decreases smoothly.

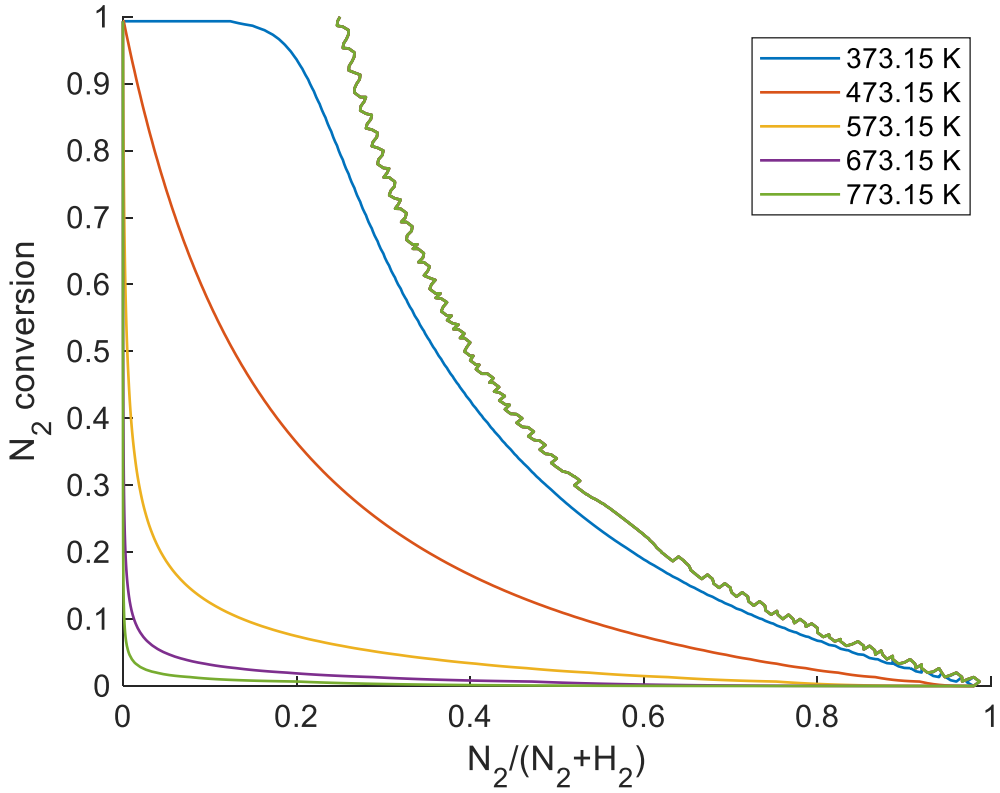

Figure-A 4 N_2 conversion plotted against $N_2/(N_2+H_2)$ under different temperatures.

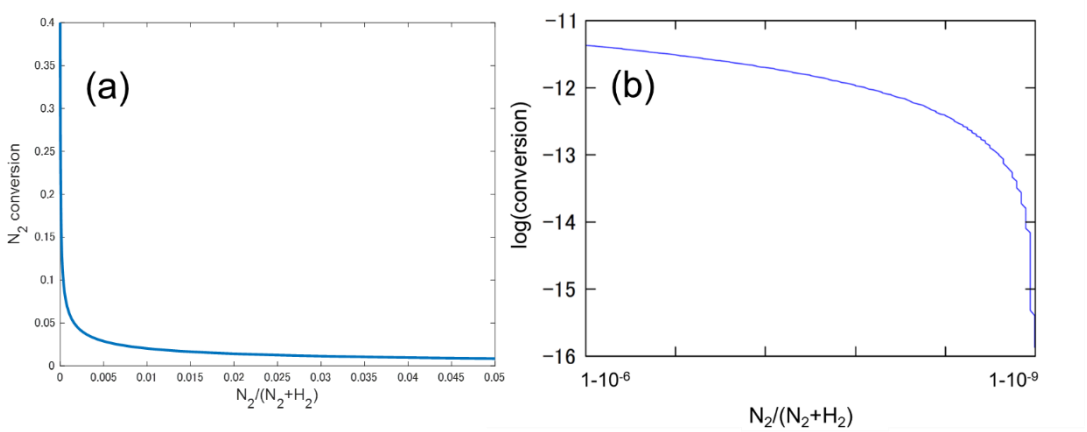

Figure-A 5 Magnified view of the N_2 conversion ratio vs. N_2 fraction at 500 °C and ambient pressure. (a) Low N_2 fraction. (b) High N_2 fraction. The y axis of (b) is logarithmic axis.

A.2 Colorimetric method for NH_3 and N_2H_4 quantification in this work

DR900 colorimeter (HACH) is used for NH_3 and N_2H_4 quantification. For salicylate method (method 8155[121]), a set of reagents containing two types of powder pillows, a salicylate powder pillow (HACH 1337) and an ammonia cyanurate powder pillow (HACH 1336). For p-dimethylaminobenzadehyde method (method8141[122]), a HydraVer2 Hydrazine Reagent is used. The procedures for NH_3 and N_2H_4 quantification by colorimetric method are shown in Figure-A 6, 7. The measuring range of NH_3-N by salicylate method is 0.01 to 0.50 mg/L. the concentration of NH_3-N measured in this work is in the range of 0.01 to 0.56 mg/L. The measuring range of N_2H_4 by p-dimethylaminobenzadehyde method is 10 to 500 μg/L. the concentration of NH_3-N measured in this work is in the range of 8 to 26 μg /L. Since phosphate was used as electrolyte for NH_3 electrochemical synthesis at 220 °C, phosphate can be a possible interfering substance in NH_3 quantification. From Table-A 3, because the interfering level of PO_4^{3-}-P is sufficiently high, the interferences of PO_4^{3-}P can be ignored. Since the concentration of NH_3-N measured in this work is in the range of 0.01 to 0.56 mg/L, it is far below the level of NH_3 interference level in N_2H_4 quantification in Table-A 4.

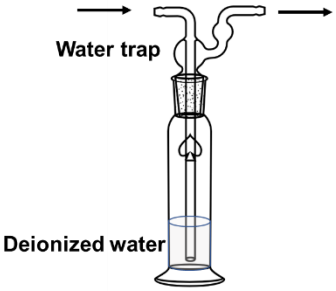

1. Sample collection.

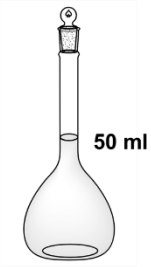

2. Precise dilutions of sample.

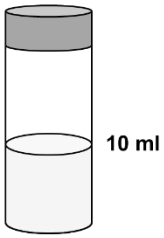

3. Prepared for blank. Fill the blank solution into the sample cell.

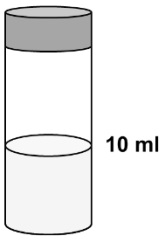

4. Fill the sample into the sample cell.

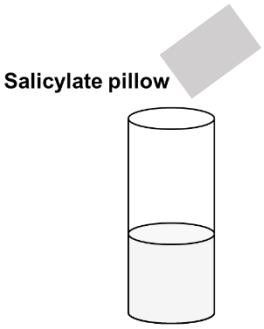

5. Add the salicylate powder pillow into the sample cell (for both blank and sample).

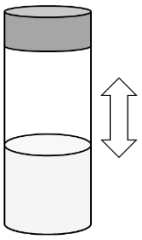

6. Shake to dissolve the reagent

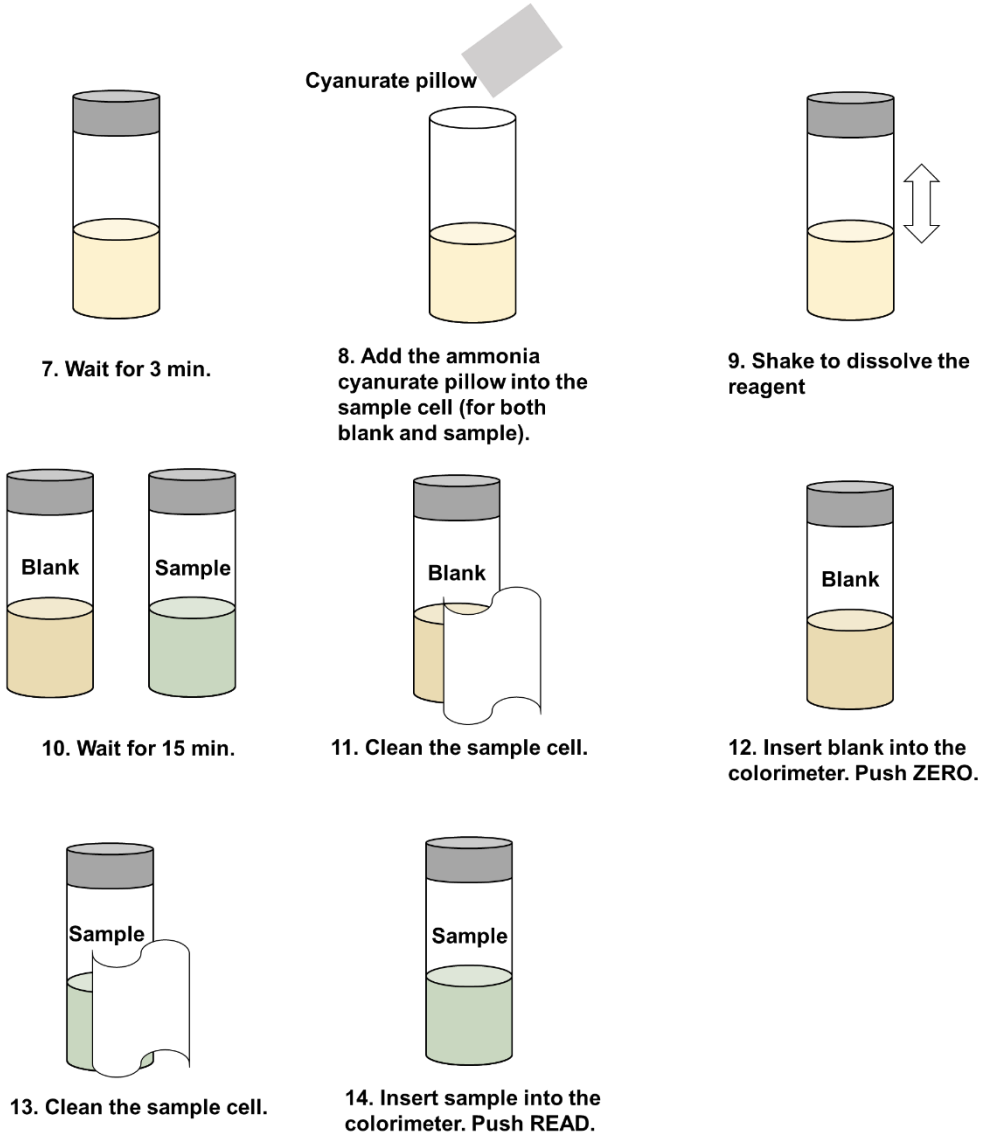

Figure-A 6 Procedure for NH_3 quantification by colorimetric method.

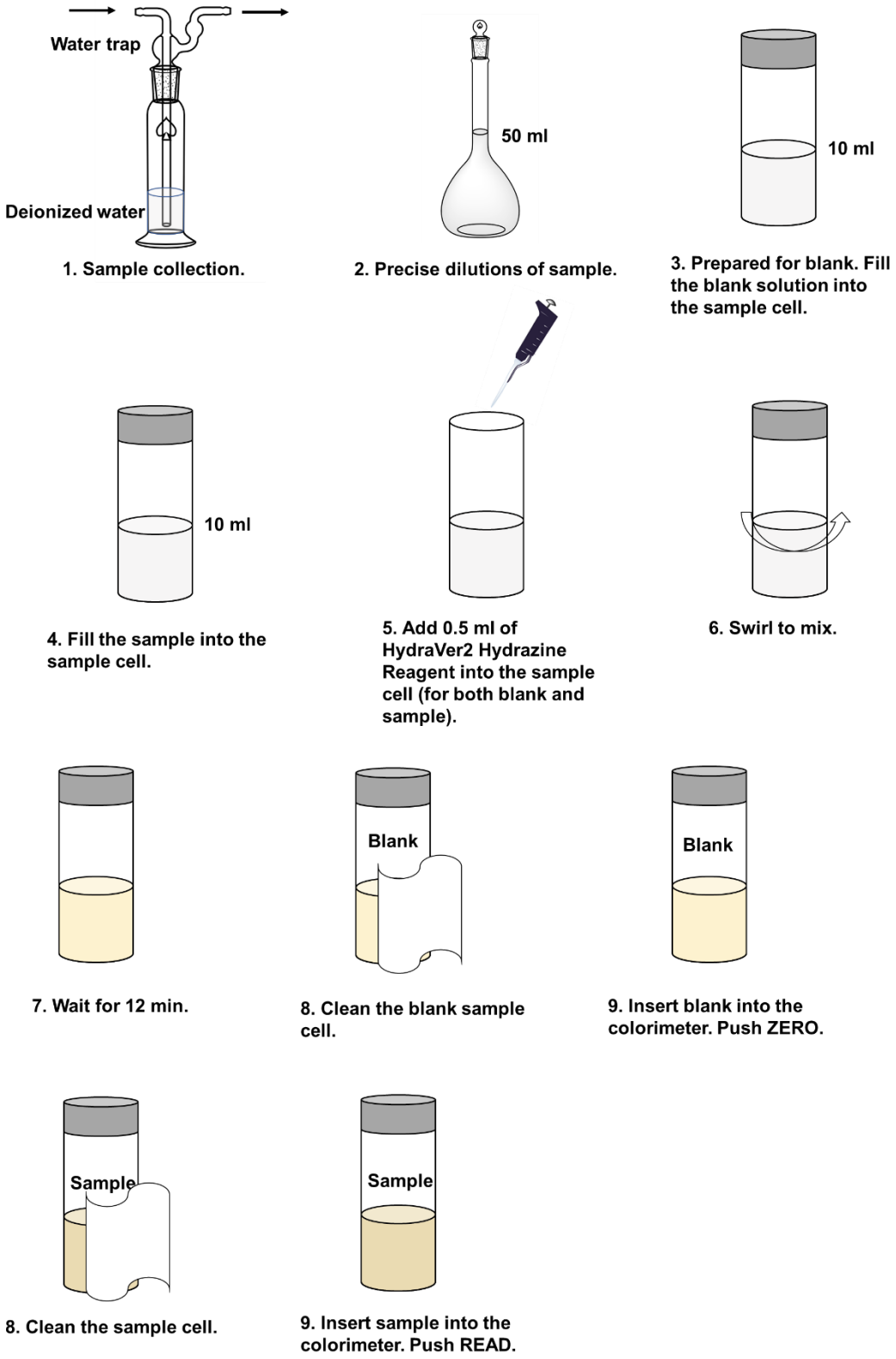

Figure-A 7 Procedure for N_2H_4 quantification by colorimetric method.

Table-A 3 Possible interferences in NH_3 quantification by colorimetric in this work.

Interfering substance	Interference level
Phosphate	100 mg/L as PO_4^{3-}-P

Table-A 4 Possible interferences in N_2H_4 quantification by colorimetric in this work.

Interfering substance	Interference level
NH_3	No interference up to 10 mg/L.

For a 30 min trap diluted with a 50 ml volumetric flask, the reaction rate with a unit of mol/(s cm^2) is calculated by:

$$r(\mathrm{NH_3}) = READ \times \frac{50}{1000} \times \frac{1}{1000} \times \frac{1}{14} \times \frac{1}{30 \times 60} \times \frac{1}{0.5^2\pi}$$

$$r(\mathrm{N_2H_4}) = READ \times \frac{50}{1000} \times \frac{1}{1000000} \times \frac{1}{32} \times \frac{1}{30 \times 60} \times \frac{1}{0.5^2\pi}$$

The Faraday efficiency (FE) under a constant current I with a unit of A is calculated by:

$$FE(\mathrm{NH_3}) = READ \times \frac{50}{1000} \times \frac{1}{1000} \times \frac{1}{14} \times 3 \times \frac{1}{30 \times 60} \times F \times \frac{1}{I}$$

$$FE(\mathrm{N_2H_4}) = READ \times \frac{50}{1000} \times \frac{1}{1000000} \times \frac{1}{32} \times 4 \times \frac{1}{30 \times 60} \times F \times \frac{1}{I}$$

A.3 Impedance fitting calculation

A simple equivalent circuit for the case of charge transfer at the electrode-solution interface is shown in Fig-A 8. In this equivalent circuit, the charge transfer resistance R_1 is parallel with the electric double layer capacitance C_1, and the RC-circuit and the solution resistance R_s are in series.[123] Impedance caused by C_1 is given as:

$$Z_c = \frac{1}{j(2\pi f)C_1}$$

The symbol f is the frequency, and j is an imaginary number. The total impedance Z can be separated into the real part Z' and the imaginary part Z". The equations are given as:

$$Z = Z' - jZ"$$

$$Z' = R_s + \frac{R_1}{1 + \left((2\pi f)C_1\right)^2 R_1^2}$$

$$Z" = \frac{(2\pi f)C_1 R_1^2}{1 + \left((2\pi f)C_1\right)^2 R_1^2}$$

An impedance plot with real part Z' on the horizonal axis and the imaginary part Z" on the vertical axis is a Nyquist plot. The shape of the Nyquist plot drawn on the basis of Figure-A 8 is a semicircle. The frequency at the apex of the semicircle is given by:

$$\omega_{max1} = 2\pi f_1 = \frac{1}{C_1 R_1}$$

The symbol ω_{max1} means the angular frequency at the apex of the Nyquist plot. However, in actual measurement, the impedance always shows a collapsed shape in the direction of the real number axis. Therefore, a constant phase element (CPE_1) is used instead of C_1 as shown in Figure-A 9 for curve fitting.

Impedance caused by CPE_1 is given as[124]:

$$Z_c = \frac{1}{j(2\pi f)^P T}$$

The simple T is a constant with a unit of Fs^{p-1}, and P is a dimensionless exponent, representing the degree of collapse of the semicircle. When P is 1, the Nyquist plot is a normal semicircle.

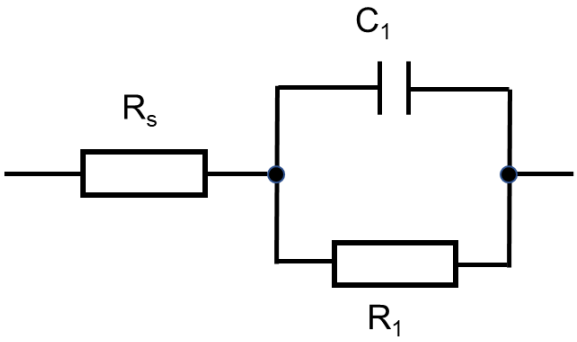

Figure-A 8 A simple equivalent circuit for the case of charge transfer at the electrode-solution interface. R_s is the resistance of the solution, C_1 is the electric double layer capacitance, and R_1 is the charge transfer resistance.

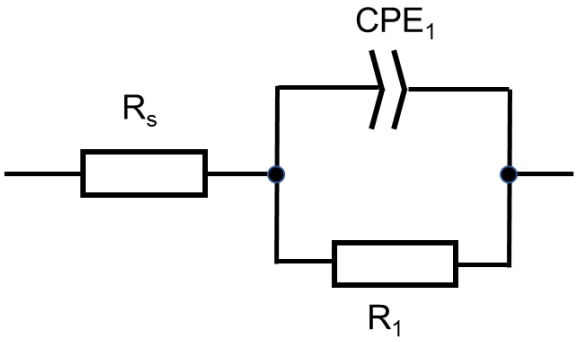

Figure-A 9 Equivalent circuit using CPE_1 instead of C_1.

A.4 Standard deviation calculation

The error bars in Figure 19 and Figure 43 in Chapter 3 and 4 are standard deviations.

$$\bar{x} = \frac{1}{n}\sum_{i}^{n} x_i$$

$$s = \sqrt{\frac{1}{n-1}\sum_{i}^{n}(x_i - \bar{x})^2}$$

Where $\bar{x}$ is the mean value of the sample data x_i (i=1, 2, …, n), n is the size of the sample. Here the standard deviation is calculated by the corrected sample standard deviation s. In this work, the sample size in Figure 19 and Figure 43 is 4.

A.5 Proton conductivity calculation

As the definition, R, the resistance, is directly proportional to the distance l and the specific resistance ρ, and inversely proportional to the area A. The conductance σ is the reciprocal of ρ. In the case of proton conductivity measurement, the resistance R can be derived from the impedance spectra.

$$R = \frac{l}{A}\rho$$

$$\sigma = \frac{1}{\rho}$$

The dependance of σ on temperature T can be expressed by the Arrhenius equation. E_a is the activation energy, and k_B is the Boltzmann constant which is defined exactly 1.380649 × 10^{-23} J/K. As a result, the larger the activation energy, the faster the σ changes with temperature. A is the frequency factor which is a constant.

$$\sigma T = Aexp(\frac{-E_a}{k_B T})$$

A.6 Effective medium approximation (EMA)

The approximation is a self-consistent scheme, especially for the cases where volume fractions of the pure phases are both large in the two-phase medium.[125] According to Furusawa et al.[126],in a binary-phase system consists the matrix (the electrical conductor), the insulating particles (BZY) and the highly electrical conducting boundary layer. The matrix with resistivity ρ_0 is supposed to be randomly replaced with the insulator with resistivity ρ_1 and the volume ratio p ($0 \leq p \leq 1$). An interfacial with resistivity ρ_2 and thickness d will be formed between the phases. The probabilities P_i (i = 0, 1, 2) of each material with resistivity ρ_0, ρ_1 and ρ_2 are given as:

$$P_0 = (1-p)^m$$

$$P_1 = p$$

$$P_2 = (1-p)[1-(1-p)^{m-1}]$$

$$m = (d/a)^3$$

Where a is *a* characteristic length. Assume the resistivity of a resistor cube composed of the insulator and the surrounded interface to be ρ_r. ρ_r is given as:

$$\frac{1}{\rho_r} = \frac{1-(1+q)^{-2/3}}{\rho_2} + \frac{(1+q)^{-1/3}}{\rho_1 + \rho_2[(1+q)^{1/3}-1]}$$

$$q = P_2/P_1$$

Using the effective medium approximation, the effective resistivity ρ^* can be given as:

$$\frac{(1/\rho_0)-(1/\rho^*)}{(1/\rho_0)+(2/\rho^*)}P_0 + \frac{(1/\rho_r)-(1/\rho^*)}{(1/\rho_r)+(2/\rho^*)}(P_1+P_2) = 0$$

Nomenclature

Symbols

$\boldsymbol{A}$	frequency factor
$\boldsymbol{A}$	absorbance
$\boldsymbol{c}$	concentration
$\boldsymbol{c}$	speeds of light
$\boldsymbol{c_p}^\circ$	specific heat capacity at constant pressure
$\boldsymbol{D}$	diffusion coefficient
$\boldsymbol{E}$	voltage
$\boldsymbol{E_a}$	activation energy
$\boldsymbol{f}$	frequency
$\boldsymbol{F}$	Faraday constant
$\boldsymbol{G}$	Gibbs free energy
$\boldsymbol{H}$	enthalpy
$\boldsymbol{I}$	current
$\boldsymbol{I}$	transmittance or reflectance
$\boldsymbol{k}$	reaction rate constant
$\boldsymbol{k}$	bond strength
$\boldsymbol{k_B}$	Boltzmann constant
$\boldsymbol{K}$	equilibrium constant
$\boldsymbol{l}$	thickness
$\boldsymbol{L}$	inductor
$\boldsymbol{m}$	mass
$\boldsymbol{N_A}$	Avogadro constant

$\boldsymbol{p}$	partial pressure
$\boldsymbol{r}$	production rate
$\boldsymbol{R}$	molar gas constant
$\boldsymbol{R}$	resistance
$\boldsymbol{s}$	standard deviation
$\boldsymbol{S}$	entropy
$\boldsymbol{T}$	temperature
$\boldsymbol{v}$	frequency of vibration
$\boldsymbol{x}$	distance
$\boldsymbol{\theta}$	angle
$\boldsymbol{\theta}$	coverage
$\boldsymbol{\Lambda}$	enhancement factor
$\boldsymbol{\rho}$	specific resistance
$\boldsymbol{\sigma}$	conductivity
⌀	diameter

Abbreviations

AC	Alternate current
AFCs	alkaline fuel cells
AMFCs	alkaline membrane fuel cells
BZY	Yttrium-doped barium zirconate
CDP	CsH_2PO_4
CE	counter electrode
CPE	constant phase element
DFT	density functional theory
DRIFTS	diffuse reflectance infrared Fourier transform spectroscopy
EDS	Energy dispersive X-ray spectroscopy
EMA	effective medium approximation
FE	Faradaic efficiency
FIR	far-infrared
FTIR	Fourier-transformed infrared
HER	hydrogen evolution reaction
IR	Infrared
IV	current-voltage
MIE	minimum ignition energy
MIR	mid-infrared
MvK	Mars-van Krevelen
NEMCA	Non-Faradaic electrochemical modification of catalytic activity
NIR	near-infrared
NRR	nitrogen reduction reaction

OCV	open circuit voltage
PTFE	polytetrafluoroethylene
RC	resistor-capacitor
RDS	rate determining step
RE	reference electrode
RT	room temperature
SDC	samarium-doped ceria
SEM	scanning electron microscope
SHE	standard hydrogen electrode
SMR	steam-methane reforming
SOFCs	solid oxides fuel cells
STP	standard temperature and pressure
TMNs	transition metal nitrides
TPR	temperature programmed reduction
WE	working electrode
WGS	water-gas shift
XRD	X-ray diffraction
YSZ	yttria-stabilized zirconate

List of Publications

Publications related to this dissertation

Yuan, Yao, Shohei Tada, and Ryuji Kikuchi.

"Ammonia synthesis using Fe/BZY–RuO_2 catalysts and a caesium dihydrogen phosphate-based electrolyte at intermediate temperatures."

Materials Advances 2.2 (2021): 793-803.

Chapter 2, 3

Yuan, Yao, Shohei Tada, and Ryuji Kikuchi.

"Electrochemically promoted ammonia synthesis on an Fe/$BaZr_{0.8}Y_{0.2}O_{3-\delta}$ catalyst at ambient pressure." (under review)

Chapter 2, 4

Yuan, Yao, and Ryuji Kikuchi.

"Ionic and Electronic Conductivities of Yttrium-doped Barium Zirconate-Hematite Composite Electrolytes." (under review)

Chapters 2, 4

Diffuse reflectance infrared Fourier transform spectroscopy (DRIFTS) for the *in situ* analysis of adsorbed N-containing spices during electrolysis (in preparation)

Chapter 5

Acknowledgments

I am using this opportunity to express my gratitude to everyone who supported me throughout the doctoral course.

I acknowledge the support from the Graduate School of Engineering, The University of Tokyo Doctoral Student Special Incentives Program (SEUT).

I would like to express my sincere gratitude to my supervisor *Associate Professor Ryuji Kikuchi* for the continuous supervising and support of my master's course and doctoral course. I am grateful for him for his positive comments and encouragement of many of my preliminary ideas. With his help, I was able to try out many new ideas and learnt how to organize my ideas clearly and present them to others in a concise and plain way.

I appreciate the members of my dissertation committee; *Professor Jun Kubota* (Fukuoka University), *Professor Akira Nakayama* (The University of Tokyo), *Professor Masaru Ogura* (The University of Tokyo), and *Professor Kazuhiro Takanabe* (The University of Tokyo) (alphabetical order). Their constructive criticism helped me sophisticate this dissertation.

I am grateful to *Assistant Professor Shohei Tada* (Ibaraki University) for his help in research work, especially in the FTIR measurements. I am grateful to *Dr. Naoya Fujiwara* and *Dr. Geletu Qing* for their helpful comments in research work. I am grateful to laboratory secretaries *Ms. Yukie Ichikawa* and *Ms. Noriko Kuwabara* for administration. I am grateful to all other laboratory members for their kind help in research work and life in Japan.

I am deeply thankful to *Professor Baoshi Du* (Zhengzhou University) for initiating me in chemistry during my high school years. It was under his influence that I became interested in chemistry. Although I will not be conducting research in chemistry in the future, his

rigorous approach to teaching and research has had a long-lasting impact on my life.

I am deeply grateful to my parents for their love and support. Thank them for their respect of my decisions in my future life.

Finally, I would like to express my deepest thanks to my husband *Ryuichi Ohori*. I would like to thank him for discussing problems in my research, and providing me valuable advices on mathematical modelling. Thank him for his understanding and enduring love.

Yao Yuan

Reference

1 https://www.nobelprize.org/prizes/chemistry/1918/haber/lecture/

2 https://www.nobelprize.org/prizes/chemistry/1931/bosch/biographical/

3 I. Rafiqul, C. Weber, B. Lehmann and A. Voss, *Energy*, **2005**, 30, 2487-2504.

4 C. Smith, A. K. Hill and L. Torrente-Murciano, *Energy & Environmental Science*, **2020**, 13, 331-344.

5 https://www.basf.com/ca/en/who-we-are/history/1902-1924.html

6 J. N. Galloway, F. J. Dentener, D. G. Capone, E. W. Boyer, R. W. Howarth, S. P. Seitzinger, G. P. Asner, C. C. Cleveland, P. A. Green, E. A. Holland, D. M. Karl, A. F. Michaels, J. H. Porter, A. R. Townsend and C. J. Vöosmarty, *Biogeochemistry*, **2004**, 70, 153-226.

7 E. Skúlason, T. Bligaard, S. Gudmundsdóttir, F. Studt, J. Rossmeisl, F. Abild-Pedersen, T. Vegge, H. Jónsson and J. K. Nørskov, *Physical Chemistry Chemical Physics*, **2012**, 14, 1235-1245.

8 J. G. Howalt, T. Bligaard, J. Rossmeisl and T. Vegge, *Physical Chemistry Chemical Physics*, **2013**, 15, 7785-7795.

9 J.-L. Shi, S.-Q. Xiang, W. Zhang and L.-B. Zhao, *Physical Chemistry Chemical Physics*, **2020**, 22, 25973-25981.

10 T. Wu, W. Fan, Y. Zhang and F. Zhang, *Materials Today Physics*, **2021**, 16, 100310.

11 S. Zhao, X. Lu, L. Wang, J. Gale and R. Amal, *Advanced Materials*, **2019**, 31, 1805367.

12 Y. Yang, L. Zhang, Z. Hu, Y. Zheng, C. Tang, P. Chen, R. Wang, K. Qiu, J. Mao, T. Ling and S.-Z. Qiao, *Angewandte Chemie International Edition*, **2020**, 59, 4525-4531.

13 Y. Liu, Y. Su, X. Quan, X. Fan, S. Chen, H. Yu, H. Zhao, Y. Zhang and J. Zhao, *ACS Catalysis*, **2018**, 8, 1186-1191.

14 L. Zhang, L.-X. Ding, G.-F. Chen, X. Yang and H. Wang, *Angewandte Chemie International Edition*, **2019**, 58, 2612-2616.

15 X. Li, X. Sun, L. Zhang, S. Sun and W. Wang, *Journal of Materials Chemistry A*, **2018**, 6, 3005-3011.

16 Z. Zhao, Y. Long, S. Luo, Y. Luo, M. Chen and J. Ma, *Journal of Energy Chemistry*, **2021**, 60, 546-555.

17 Y. Abghoui and E. Skúlason, *Catalysis Today*, **2017**, 286, 69-77.

18 D. Yan, H. Li, C. Chen, Y. Zou and S. Wang, *Small Methods*, **2019**, 3, 1800331.

19 Y. Xu, X. Xu, N. Cao, X. Wang, X. Liu, M. Fronzi and L. Bi, *International Journal of Hydrogen Energy*, **2021**, 46, 10293-10302.

20 L. Zhu, R. Ran, M. Tadé, W. Wang and Z. Shao, *Asia-Pacific Journal of Chemical Engineering*, **2016**, 11, 338-369.

21 J. Yu, C. Li, B. Li, X. Zhu, R. Zhang, L. Ji, D. Tang, A. M. Asiri, X. Sun, Q. Li, S. Liu and Y. Luo, *Chemical Communications*, **2019**, 55, 6401-6404.

22 C. Li, D. Ma, S. Mou, Y. Luo, B. Ma, S. Lu, G. Cui, Q. Li, Q. Liu and X. Sun, *Journal of Energy Chemistry*, **2020**, 50, 402-408.

23 Y. Xu, X. Xu, N. Cao, X. Wang, X. Liu, M. Fronzi and L. Bi, *International Journal of Hydrogen Energy*, **2021**, 46, 10293-10302.

24 M. E. Vol'Pin and V. B. Shur, *Nature*, **1966**, 209, 1236-1236.

25 D. V. Yandulov and R. R. Schrock, *Science*, **2003**, 301, 76.

26 J. D. Gilbertson, N. K. Szymczak and D. R. Tyler, *Journal of the American Chemical Society*, **2005**, 127, 10184-10185.

27 J. Y. Becker, S. Avraham and B. Posin, *Journal of electroanalytical chemistry and interfacial electrochemistry*, **1987**, 230, 143-153

28 P. Saha, S. Amanullah and A. Dey, *Journal of the American Chemical Society*, **2020**, 142, 17312-17317.

29 H. Deng and R. Hoffmann, *Angewandte Chemie International Edition in English*, **1993**, 32, 1062-1065.

30 O. Einsle, F. A. Tezcan, S. L. A. Andrade, B. Schmid, M. Yoshida, J. B. Howard and D. C. Rees, *Science*, **2002**, 297, 1696.

31 J. Kirn and D. C. Rees, *Nature*, **1992**, 360, 553-560.

32 R. D. Milton, R. Cai, S. Abdellaoui, D. Leech, A. L. De Lacey, M. Pita and S. D. Minteer, *Angewandte Chemie International Edition*, **2017**, 56, 2680-2683.

33 D. P. Hickey, K. Lim, R. Cai, A. R. Patterson, M. Yuan, S. Sahin, S. Abdellaoui and S. D. Minteer, *Chemical Science*, **2018**, 9, 5172-5177.

34 R. Cai and S. D. Minteer, *ACS Energy Letters*, **2018**, 3, 2736-2742.

35 X. Cui, C. Tang and Q. Zhang, *Advanced Energy Materials*, **2018**, 8, 1800369.

36 R. Lan and S. Tao, *RSC Advances*, **2013**, 3, 18016-18021.

37 T. Murakami, T. Nishikiori, T. Nohira and Y. Ito, *Journal of the American Chemical Society*, **2003**, 125, 334-335.

38 N. Serizawa, H. Miyashiro, K. Takei, T. Ikezumi, T. Nishikiori and Y. Ito, *Journal of The Electrochemical Society*, **2012**, 159, E87.

39 S. Licht, B. Cui, B. Wang, F.-F. Li, J. Lau and S. Liu, *Science*, **2014**, 345, 637-640.

40 Y. Bicer and I. Dincer, *International Journal* of *Energy Research*, **2017**, 41, 1987-2000.

41 Y. Bicer and I. Dincer, *Journal of the* Electrochemical Society, **2017**, 164, H5036-H5042

42 S. Kishira, G. Qing, S. Suzu, R. Kikuchi, A. Takagaki and S. T. Oyama, *International Journal* of *Hydrogen Energy*, **2017**, 42, 26843-26854.

43 M. Ouzounidou, A. Skodra, C. Kokkofitis and M. Stoukides, *Solid State Ionics*, **2007**, 178, 153-159.

44 Y. Guo, B. Liu, Q. Yang, C. Chen, W. Wang and G. Ma, *Electrochemistry Communications*, **2009**, 11, 153-156.

45 F. Kosaka, T. Nakamura and J. Otomo, *Journal of The Electrochemical Society*, **2017**, 164, F1323-F1330.

46 M. Zhang, J. Xu and G. Ma, *Journal of Materials Science*, **2011**, 46, 4690-4694.

47 D. S. Yun, J. H. Joo, J. H. Yu, H. C. Yoon, J.-N. Kim and C.-Y. Yoo, *Journal of Power Sources*, **2015**, 284, 245-251.

48 Z. Chen, J. Zhao, C. R. Cabrera and Z. Chen, *Small Methods*, **2019**, 3, 1800368.

49 Z. Geng, Y. Liu, X. Kong, P. Li, K. Li, Z. Liu, J. Du, M. Shu, R. Si and J. Zeng, *Advanced Materials*, **2018**, 30, 1803498.

50 F. Zhou, L. M. Azofra, M. Ali, M. Kar, A. N. Simonov, C. McDonnell-Worth, C. Sun, X. Zhang and D. R. MacFarlane, *Energy & Environmental Science*, **2017**, 10, 2516-2520.

51 K. Kim, C.-Y. Yoo, J.-N. Kim, H. C. Yoon and J.-I. Han, *Journal of The Electrochemical Society*, **2016**, 163, F1523.

52 K. Imamura, M. Matsuyama and J. Kubota, *ChemistrySelect*, **2017**, 2, 11100-11103.

53 J. H. Montoya, C. Tsai, A. Vojvodic and J. K. Nørskov, *ChemSusChem*, **2015**, 8, 2180-2186.

54 P. Mars, D.W. van Krevelen, *Chemical Engineering Science*, **1954**, 3, 41.

55 J. R. H. Ross, in Contemporary Catalysis, ed. J. R. H. Ross, Elsevier, Amsterdam, **2019**, pp. 161-186.

56 P. L. Searle, *Analyst*, **1984**, 109, 549-568.

57 J. Tetlow and A. Wilson, *Analyst*, **1964**, 89, 453-465.

58 M. D. Krom, *Analyst*, **1980**, 105, 305-316.

59 Z. Genfa and P. K. Dasgupta, *Analytical Chemistry*, **1989**, 61, 408-412.

60 R. Kérouel and A. Aminot, *Marine Chemistry*, **1997**, 57, 265-275.

61 A. J. Kendall, S. I. Johnson, R. M. Bullock and M. T. Mock, *Journal of the American Chemical Society*, **2018**, 140, 2528-2536.

62 Y. Zhao, R. Shi, X. Bian, C. Zhou, Y. Zhao, S. Zhang, F. Wu, G. I. N. Waterhouse, L.-Z. Wu, C.-H. Tung and T. Zhang, *Advanced Science*, **2019**, 6, 1802109.

63 J. D. Mulik and E. Sawicki, *Environmental Science & Technology*, **1979**, 13, 804-809.

64 J. Shaw and B. Staddon, *Journal of Experimental Biology*, **1958**, 35, 85-95.

65 B. H. R. Suryanto, H.-L. Du, D. Wang, J. Chen, A. N. Simonov and D. R. MacFarlane, *Nature Catalysis*, **2019**, 2, 290-296.

66 S. Z. Andersen, V. Čolić, S. Yang, J. A. Schwalbe, A. C. Nielander, J. M. McEnaney, K. Enemark-Rasmussen, J. G. Baker, A. R. Singh, B. A. Rohr, M. J. Statt, S. J. Blair, S. Mezzavilla, J. Kibsgaard, P. C. K. Vesborg, M. Cargnello, S. F. Bent, T. F. Jaramillo, I. E. L. Stephens, J. K. Nørskov and I. Chorkendorff, *Nature*, **2019**, 570, 504-508.

67 S. L. Foster, S. I. P. Bakovic, R. D. Duda, S. Maheshwari, R. D. Milton, S. D. Minteer, M. J. Janik, J. N. Renner and L. F. Greenlee, *Nature Catalysis*, **2018**, 1, 490-500.

68 D. Pergolesi, E. Fabbri, A. D'Epifanio, E. Di Bartolomeo, A. Tebano, S. Sanna, S. Licoccia, G. Balestrino and E. Traversa, *Nature Materials*, **2010**, 9, 846-852.

69 Y. Yuan, R. Kikuchi, A. Takagaki and S. T. Oyama, *ECS Transactions*, **2017**, 78, 451-459.

70 S. Klotz, Y. Le Godec, T. Strässle and U. Stuhr, *Applied Physics Letters*, **2008**, 93, 091904.

71 H. A. Wriedt, N. A. Gokcen and R. H. Nafziger, *Bulletin of Alloy Phase Diagrams*, **1987**, 8, 355-377.

72 H. S. Zeng, K. Inazu and K.-i. Aika, *Journal of Catalysis*, **2002**, 211, 33-41.

73 H. Mayama and K. Tsujii, *The Journal of Chemical Physics*, **2006**, 125, 124706.

74 G. Qing, K. Sukegawa, R. Kikuchi, A. Takagaki and S. T. Oyama, *Journal of Applied Electrochemistry*, **2017**, 47, 803-814.

75 R. McKibben, R. M. Sharp, D. A. Harrington, B. G. Pound and G. A. Wright, *Acta Metallurgica*, **1987**, 35, 253-262.

76 B. G. Pound, G. A. Wright and R. M. Sharp, *Acta Metallurgica*, **1987**, 35, 263-270

77. D. Pergolesi, E. Fabbri, A. D'Epifanio, E. Di Bartolomeo, A. Tebano, S. Sanna, S. Licoccia, G. Balestrino and E. Traversa, *Nature Materials*, **2010**, 9, 846-852.

78. Y. Yamazaki, R. Hernandez-Sanchez and S. M. Haile, *Chemistry of Materials*, **2009**, 21, 2755-2762.

79. P. Babilo and S. M. Haile, *Journal of the American Ceramic Society*, **2005**, 88, 2362-2368.

80 E. Fabbri, D. Pergolesi, S. Licoccia and E. Traversa, *Solid State Ionics*, **2010**, 181, 1043-1051.

81 P. Babilo, T. Uda and S. M. Haile, Journal of materials research, 2007, 22, 1322-1330.

82 L. F. Greenlee, J. N. Renner and S. L. Foster, *ACS Catalysis*, **2018**, 8, 7820-7827.

83 C. G. Yiokari, G. E. Pitselis, D. G. Polydoros, A. D. Katsaounis and C. G. Vayenas, *The Journal of Physical Chemistry A*, **2000**, 104, 10600-10602.

84 I. V. Yentekakis and S. Bebelis, *Journal of Catalysis*, **1992**, 137, 278-283.

85 C. Peng, J. Melnik, J.-L. Luo, A. R. Sanger and K. T. Chuang, *Solid State Ionics*, **2010**, 181, 1372-1377.

86 X. Tian, P. Zhao and W. Sheng, *Advanced Materials*, **2019**, 31, 1808066.

87 E. Skúlason, V. Tripkovic, M. E. Björketun, S. Gudmundsdóttir, G. Karlberg, J. Rossmeisl, T. Bligaard, H. Jónsson and J. K. Nørskov, *The Journal of Physical Chemistry C*, **2010**, 114, 18182-18197.

88 J. X. Wang, T. E. Springer and R. R. Adzic, *Journal of the Electrochemical Society*,

2006, 153, A1732.

89 T. Kandemir, M. E. Schuster, A. Senyshyn, M. Behrens and R. Schlögl, *Angewandte Chemie International Edition*, **2013**, 52, 12723-12726

90 L. Carolei and I. G. R. Gutz, *Talanta*, **2005**, 66, 118-124.

91 T. Barzetti, E. Selli, D. Moscotti and L. Forni, *Journal of the Chemical Society, Faraday Transactions*, **1996**, 92, 1401-1407.

92 H. Niki, P. Maker, C. Savage, L. Breitenbach and M. Hurley, *Journal of Physical Chemistry*, **1987**, 91, 941-946.

93 C. Berthomieu and R. Hienerwadel, *Photosynthesis Research*, **2009**, 101, 157-170.

94 M. B. Esler, D. W. T. Griffith, F. Turatti, S. R. Wilson, T. Rahn and H. Zhang, *Chemosphere - Global Change Science*, **2000**, 2, 445-454.

95 J. Manor, E. Arbely, A. Beerlink, M. Akkawi and I. T. Arkin, *The Journal of Physical Chemistry Letters*, **2014**, 5, 2573-2579.

96 A. Barth, *Biochimica et Biophysica Acta (BBA) - Bioenergetics*, **2007**, 1767, 1073-1101.

97 Jasco, Principles of infrared spectroscopy (6) Various measurement methods in FTIR spectroscopy-reflection methods-

98 P. Song, H. Wang, L. Kang, B. Ran, H. Song and R. Wang, *Chemical Communications*, **2019**, 55, 687-690.

99 D. J. Cumming, C. Tumilson, S. F. R. Taylor, S. Chansai, A. V. Call, J. Jacquemin, C. Hardacre and R. H. Elder, *Faraday Discussions*, **2015**, 182, 97-111.

100 N. V. Rees and R. G. Compton, *Energy & Environmental Science*, **2011**, 4, 1255-1260.

101 R. Lan, J. T. S. Irvine and S. Tao, *International Journal of Hydrogen Energy*, **2012**, 37, 1482-1494.

102 A. Züttel, A. Remhof, A. Borgschulte and O. Friedrichs, *Philosophical Transactions of the Royal Society A: Mathematical, Physical and Engineering Sciences*, **2010**, 368, 3329-3342.

103 S. Suzuki, H. Muroyama, T. Matsui and K. Eguchi, *Journal of Power Sources*,

2012, 208, 257-262.

104 J. C. Ganley, *Journal of Power Sources*, **2008**, 178, 44-47.

105 T. Okanishi, K. Okura, A. Srifa, H. Muroyama, T. Matsui, M. Kishimoto, M. Saito, H. Iwai, H. Yoshida, T. Koide, S. Suzuki, Y. Takahashi, T. Horiuchi, H. Yamasaki, S. Matsumoto, S. Yumoto, H. Kubo, J. Kawahara, A. Okabe, Y. Kikkawa, T. Isomura and K. Eguchi, *Fuel Cells*, **2017**, 17, 383-390.

106 M. Ni, M. K. H. Leung and D. Y. C. Leung, *International Journal of Energy Research*, **2009**, 33, 943-959.

107 G. Meng, C. Jiang, J. Ma, Q. Ma and X. Liu, *Journal of Power Sources*, **2007**, 173, 189-193.

108 K. Xie, Q. Ma, B. Lin, Y. Jiang, J. Gao, X. Liu and G. Meng, *Journal of Power Sources*, **2007**, 170, 38-41.

109 R. Lan and S. Tao, *Frontiers in Energy Research*, **2014**, 2.

110 経済産業省　燃料アンモニア導入官民協議会 中間取りまとめ **2021**

111 F. J. Verkamp, M. C. Hardin and J. R. Williams, *Symposium (International) on Combustion*, **1967**, 11, 985-992.

112 J. Li, H. Huang, N. Kobayashi, Z. He and Y. Nagai, *International Journal of Energy Research*, **2014**, 38, 1214-1223.

113 R. Li, A. A. Konnov, G. He, F. Qin and D. Zhang, *Fuel*, 2019, 257, 116059.

114 S. Li, S. Zhang, H. Zhou and Z. Ren, *Fuel*, **2019**, 237, 50-59.

115 Z. Li and S. Li, *International Journal of Hydrogen Energy*, **2021**, 46, 4526-4537.

116 Ø. Skreiberg, P. Kilpinen and P. Glarborg, *Combustion and Flame*, **2004**, 136, 501-518.

117 K. P. Shrestha, L. Seidel, T. Zeuch and F. Mauss, *Energy & Fuels*, **2018**, 32, 10202-10217.

118 IUPAC. *Compendium of Chemical Terminology, 2nd ed. (the "Gold Book")*. Compiled by A. D. McNaught and A. Wilkinson. Blackwell Scientific Publications, Oxford (**1997**). Online version (**2019-**) created by S. J. Chalk. ISBN 0-9678550-9-8. https://doi.org/10.1351/goldbook.

119 M. B. Ewing, T. H. Lilley, G. M. Olofsson, M. T. Ratzsch and G. Somsen, *Pure and Applied Chemistry*, **1994**, 66, 533-552.

120 JANAF Thermochemical Tables

121 Nitrogen, Ammonia-Salicylate Method 8155-HACH

122 Hydrazine, p-Dimethylaminobenzaldehyde Method 8141-HACH-

123 板垣 昌幸, *Electrochemistry*, **2010**, 78, 783-785.

124 四反田 功, 酒井 悠, 渡辺 邦, 板垣 昌幸, *表面技術*, **2009**, 60, 288-288.

125 D. J. Bergman, *Physics Reports*, **1978**, 43, 377-407.

126 S. Furusawa, S. Miyaoka and Y. Ishibashi, *Journal of the Physical Society of Japan*, **1991**, 60, 1666-1671.